ROLE(S) OF PANNEXIN1A/B IN THE PHYSIOLOGY OF THE ZEBRAFISH VISUAL SYSTEM

SARAH HOUSHANGI-TABRIZI

A THESIS SUBMITTED TO THE FACULTY OF GRADUATE STUDIES IN
PARTIAL FULFILLMENT OF THE REQUIREMENTS FOR THE DEGREE OF
MASTER OF ARTS

GRADUATE PROGRAM IN PSYCHOLOGY

YORK UNIVERSITY

TORONTO, ONTARIO

JULY 2024

Abstract

Panx1 proteins are glycosylated integral membrane channels with unique conduction properties, functioning as an ATP channel and non-selective ion channel in different physiological pathways. In zebrafish, the mammalian Panx1 ohnologues, Panx1a and Panx1b, have distinct tissue expression patterns. We previously demonstrated that in the retina, Panx1a is localized in the horizontal cell layer and the ON/OFF ganglion cell layer, while Panx1b protein is present in the horizontal cell layer, ganglion cell layer, and in the end-feet of the Muller glia astrocytes. Here we investigated the optic flow response in the Panx1a$^{-/-}$ and Panx1b$^{-/-}$ 6dpf larvae utilizing molecular, systems, and behavioral assays. The RNA-seq analysis revealed broad regulation of genes involved in axon guidance, retinal axon guidance, astrocytes, axons, dendrites, and synapse, confirmed by RT-qPCR in the 3dpf and 6dpf Panx1a$^{-/-}$ and Panx1b$^{-/-}$. We demonstrate that Panx1a$^{-/-}$ and Panx1b$^{-/-}$ display an inability to make a leftward and rightward directional motion in low light contrast conditions when exposed to the left and right moving gratings. We also show how the strategic localization of Panx1a and Panx1b in the habenula region modulates visually guided behavior. Lastly, Panx1a$^{-/-}$ and Panx1b$^{-/-}$ demonstrate the inability to generate functional saccades and display ocular motor deficiencies linked to potential neurological disorders. These findings suggest that Panx1 modulates the axonal growth in axon guidance pathfinding and together are interconnected to the habenula region, leading to synaptic plasticity of the retinal neural circuitry, and regulating visually guided locomotion in the zebrafish larvae.

Acknowledgment

I wish to extend my deepest gratitude to all those who have supported me throughout my journey to complete this master’s thesis. Their support, guidance, and encouragement have been invaluable in this endeavor.

First and foremost, I would like to express my sincere appreciation to my supervisor, Dr. Georg R. Zoidl, for his unwavering support, insightful guidance, and constructive feedback throughout my research project. Your expertise and patience have helped me grow as a researcher and significantly shaped the outcome of my thesis. I am forever grateful for the opportunity to work under your mentorship.

I am also deeply thankful to my advisor, Dr. Liya Ma, for her willingness to serve on my committee, and for her critical feedback and thought-provoking insights, which have greatly enhanced my project.

A special acknowledgment goes to Christiane Zoidl for her technical expertise, constant guidance, and support in utilizing and improving various protocols. Your ability to inspire out-of-the-box thinking has been invaluable, and I am profoundly grateful for everything you have taught me.

I would also like to thank my lab team: Fatema, Darren, Georg, and Riya. Your valuable advice and support have made a significant impact on my learning experience, and I have learned so much from each of you.

My heartfelt thanks go to Janet and Veronica for their assistance and support in the vivarium. Their help ensured a smooth transition throughout my project when it came to zebrafish husbandry.

I am extremely grateful to my friends who have stood by me through thick and thin. Your unwavering support has been a constant source of strength, and I am forever grateful for your companionship.

Last but not least, I would like to express my deepest thanks to my family for their unconditional support and guidance. Your constant presence and encouragement have been the bedrock of my journey, and I am incredibly fortunate and grateful to have you by my side.

Thank you all for your invaluable support and contributions.

Table of Content

List of Abbreviations

µM	Micromolar
µm	micrometer
95%CI	95% Confidence Interval
ABN	Abducens nuclei
AF5	Arborization Field 5
ANOVA	Analysis of variance
BDNF	Brain-derived neurotrophic factor
BLAST	Basic Local Alignment Search
Bp	Base pair
cDNA	Complementary deoxyribonucleic acid
Cryo-EM	Cryo-Electron Microscopy
C-terminus	Carboxyl-terminus
Deg/sec	degree per second
DNA	Deoxyribonucleic acid
dpf	Days Post Fertilization
DS	Directional selective
EmT	Eminentia Thalami
EtBr	Ethidium bromide
FR	Fasciculi Retroflexus
Hb	Habenula
IPN	Interpeduncular Nuclei
min	Minute
mL	Millilitre
mm	Millimeter
NaCl	Sodium chloride
nMLF	Medial Longitudinal Fasciculus
OT	Optic tectum
O/N	Overnight
P-adjust	Adjusted p-value

Panx1	Pannexin1
PCR	Polymerase Chain Reaction
PD	Parkinson’s disease
PFA	Paraformaldehyde
PT	Pretectum
REST	Relative expression software tool
RS	Reticulospinal
RNA	Ribonucleic acid
RNA-seq	RNA sequencing
RT	Room Temperature
RT-qPCR	Reverse Transcription- quantitative PCR
sec	Seconds
SEM	Standard error of the mean
TALEN	Transcription activator-like effector nucleases
TL	Tupfel long fin
ZFIN	Zebrafish International Network

Tables

Figures

Supplementary Figures

1. Introduction

1.1. Pannexin1: From discovery to structure and localization

Pannexins are glycosylated integral membrane protein channels that exhibit unique conduction properties as ATP and non-selective ion channels that take part in different physiological pathways and cell-to-cell communication (Boassa et al., 2008). Pannexin1 (Panx1) comes from a family of three Pannexin glycoproteins, including Panx2 and Panx3. Panx1 (**Fig. 1**) is the most studied family member that plays a role in regulating cell-signaling cascades downstream of the purinergic, adrenergic, transient receptor potential vanilloid, and NMDA receptors (Boassa et al., 2008; Dahl, 2015; Mim et al., 2021; Sosinsky et al., 2011). Here, the Panx1 channel is extensively studied due to its functional implications in retinal physiology.

The pannexin proteins were discovered by Panchin and colleagues (2000) through a BLAST search using the GenBank human genome as a second family of gap junction proteins, based on similar sequence homology to connexin and innexin gap junctions. Panchin and colleagues (2000) were investigating sequence homology to innexin when the researcher accidentally discovered what he named Pannexin. Connexin and innexin are gap junction proteins involved in cell-to-cell communication with structural similarities to one another. Innexins are found in invertebrates and connexins are present in vertebrates (Baranova et al., 2004). Although the two proteins form gap junctions with similar functionality, they do not display sequence homology with one another (Baranova et al., 2004; Bruzzone et al., 2003).

The Pannexins were initially predicted to be homologous to innexins by sharing a conserved cysteine residue and similar transmembrane regions (Baranova et al., 2004). Pannexins, despite having structural similarity to innexins, do not display sequence homology to connexins but have topological commonalities. In addition, Pannexins unlike connexin, which forms gap junctions for cellular communications, primarily form a large-pore single membrane channel involved in paracrine signaling, ATP release, as well as serve as a calcium channel (Baranova et al., 2004; Bruzzone et al., 2003). Pannexin is now considered a separate gene family of the vertebrate genomes due to predominantly acting as a heptameric channel between the extracellular and intracellular environment (Baranova *et al.,* 2004). The new family of proteins were named as Pannexin, in which 'pan' is a Latin word for 'all' and 'nexus' is analogous to the cell-to-cell gap junction communication (Panchin et al., 2000).

The Panx1 gene forms a heptameric channel through the oligomerization of subunits with the following internal structures: two extracellular loops, four alpha-helical transmembrane (TM) domains, a cytoplasmic C- termini and N-, as well as a single intracellular loop assembling into the seven protomers (Baranova et al., 2004; Boassa et al., 2007). The cryo-electron microscopy (cry-EM) structure (**Fig.1**) of the xPANX1 ATP release channel (Deng et al., 2020) was resolved using X*enopus tropicalis* and the *Homo sapiens* PANX1 proteins.

The Panx1 has a ubiquitous expression pattern in the central nervous system (CNS), retina, skeletal muscles, skin, heart, ovaries and testes, spleen, small intestine and prostate, and is moderately found in the placenta (Baranova et al., 2004; Barbe et al., 2003). In addition, the Panx1 is present in astrocytes and neuronal cells where the blockage and modifications of the Panx1 channels alter the ATP-release pathway and lead to physiological changes in these cell types (Barbe et al., 2003; Suadicani et al., 2012).

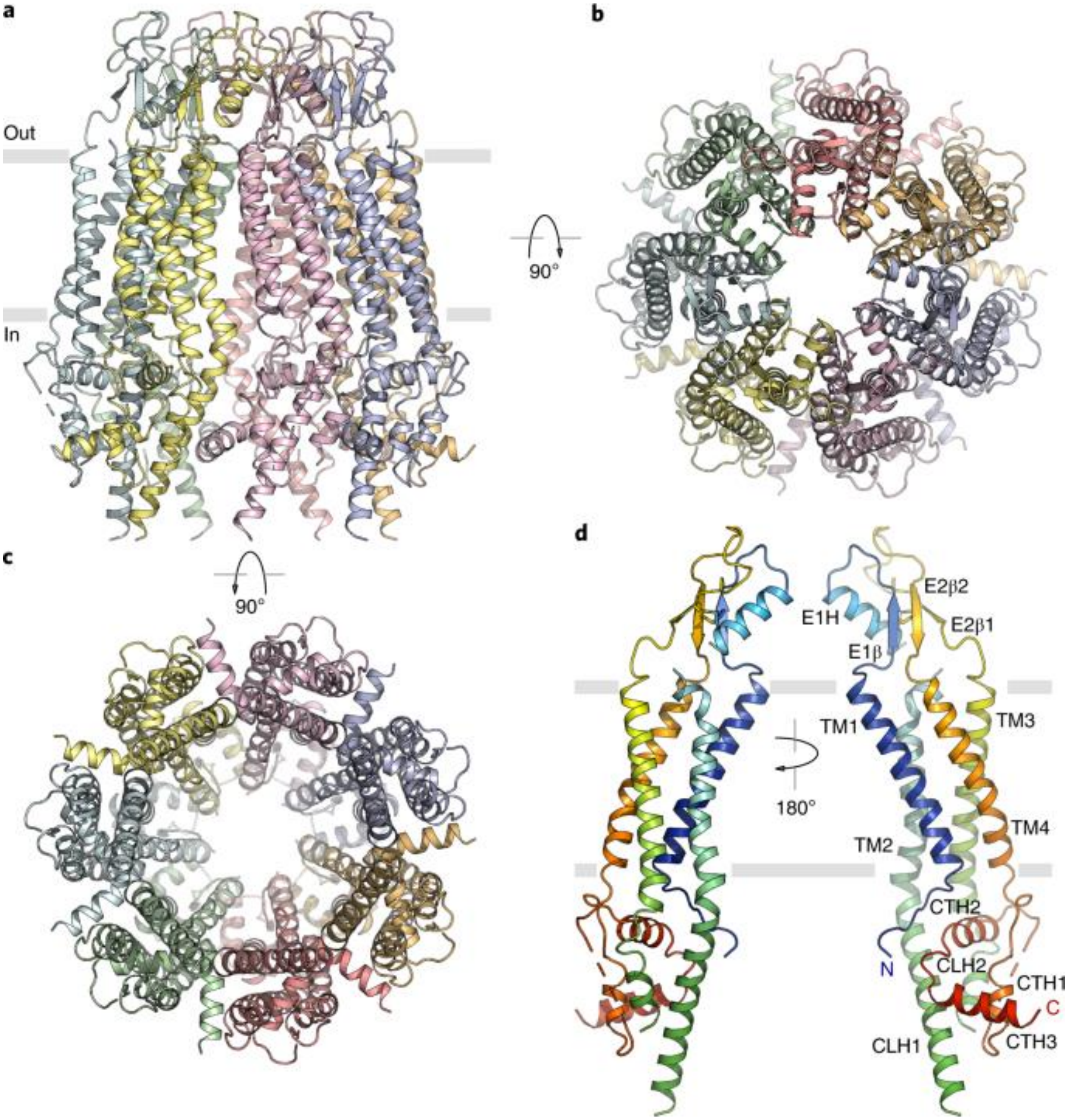

Figure 1. The cryo-EM structure of xPANX1 (*Xenopus tropicalis*) is visualized from different dimensions parallel to the membrane. a) extracellular view b) intracellular view c) capturing the individual submit and d) a single subunit with the N and C *terminus (*Image acquired from Deng et al., 2020).

1.1.1 Functional and Physiological Relevance of Panx1

The Panx1 channels are involved in various pathophysiological and physiological pathways. These proteins are activated by various stimuli including mechanical stress, calcium and potassium, glutamate, oxygen deprivation, and voltage (Michalski et al., 2018; Whyte-Fagundes & Zoidl, 2018). In addition, the Panx1 can interact with G-protein coupled receptors (P2Y) and ionotropic purinergic receptors (P2X7) and become activated (Locovei et al., 2006; Pelegrin et al., 2008). The NMDA receptors are involved in the activation of the Panx1 channels at the post-synaptic density through kinase activation (Li et al., 2018).

The Panx1 channels are involved in neuronal development, synaptic plasticity, and dendritic spine formation where the loss of these channels leads to changes in hippocampal activity and memory deficits in mice models (Gajardo et al., 2018; Prochnow et al., 2012). In the rodent model, the absence of Panx1 was also associated with changes in retinal contrast sensitivity and a reduction in the specimen’s ability to recognize objects (Prochnow et al., 2012; Zhao et al., 2015). The release of ATP through the Panx1 channels is both inhibitory and excitatory in regulating cell-signaling cascades downstream of the purinergic, adrenergic, transient receptor potential vanilloid, and NMDA receptors via ATP release (Boassa et al., 2008; Dahl, 2015; Mim et al., 2021; Sosinsky et al., 2011). The first human female patient with a homozygous Panx1 was identified to have problems with spatial navigation in low light conditions, primary ovarian failures, and intellectual disability (Shao et al., 2016). The expression of the Panx1 protein in the retina has been of much interest to researchers investigating the functional implications of the Panx1 protein in rodent and zebrafish models in the goal of better understanding vision pathologies such as ischemia and ocular hypertension (Ray et al., 2005; Kranz et al., 2012).

1.2. The functional role and tissue expression pattern of Pannexin1 in the zebrafish retina

In zebrafish, there are two ohnologues of Pannexin 1 (Panx1) present, Panx1a and Panx1b, which are expressed in different tissue patterns (Ray et al., 2005). The ohnologs are a result of whole-gene duplication over 200 million years ago during the teleost evolution (Ray et al., 2005). Panx1a is localized in the horizontal cell layer, and the ON/OFF ganglion cell layer **(Fig. 2, left image)** and Panx1b **(Fig.2, right image)** protein is expressed in the horizontal cell layer, ganglion cell layer, and is also found in the end-feet of the Muller glia astrocytes (Safarian et al., 2020; Safarian et al., 2021). Interfering with the normal channel functioning has been demonstrated to lead to physiological pathologies such as ocular hypertension and ischemia in the rodent and zebrafish visual system (Ray et al., 2005).

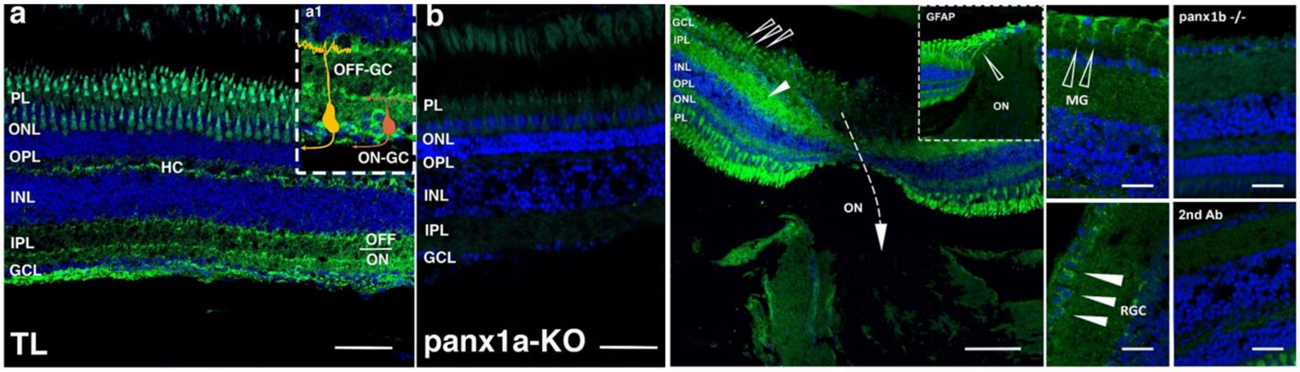

Figure 2. The expression and localization of Panx1a (in the green color image on the left) and Panx1b (in the green color image on the right) antibodies throughout the retina. Panx1a is localized in the horizontal cell layer and the ON/OFF ganglion cell layer. The Panx1b is expressed in the horizontal cell layer, ganglion cell layer, and is also found in the end-feet of the Muller glia astrocytes. (Panx1b image acquired from Sarafian et al., 2021). Image on the left, Scale bar = 25µm and image on the right, Scale bars = 100 µm; 25 µm; 20 µm.

The loss of Panx1a in zebrafish larvae led to changes in visuomotor behavior and was associated with light decrement detection and abnormal responses to visual stimulus through the retinal OFF-pathway via dopaminergic and adenosine signaling pathways (Safarian et al., 2020). In adult zebrafish, the Panx1a is also involved in a negative feedback pathway from the horizontal cell layers to the cones in the photoreceptor layer which aids in generating the centre/ surround organization of the receptive fields of bipolar cells (Cenedese et al., 2017). The absence of the Panx1b channels in 6dpf zebrafish larvae disrupts the retinal response leading the larvae to experience difficulties in navigating leftward motion in low light conditions (Safarian et al., 2021). The Panx1b is also involved in modulating the circadian clock system, mediating the sleep-wake cycle of the zebrafish visual system in forming non-visual processes (Safarian et al., 2021).

1.3. The zebrafish retinal network as a study model

The zebrafish retina is easily accessible during all stages of development and the visual system of the zebrafish is formed rapidly, as early as five days post-fertilization (dpf) (Park et al., 2016). In addition, the zebrafish model is efficient when it comes to transgenic manipulation. Due to its transparent nature, it enables researchers to do in vivo imaging experiments to study the function and structure (Kölsch et al., 2020). Interestingly, the zebrafish retina also shares color vision with humans, and the expression of Panx1 makes it ideal for vision research, as well as understanding the normal functioning of visual systems and vision pathologies (Zoidl et al., 2008). Despite the zebrafish model diverging from ancestors leading to mammals over 400 million years ago, the development of the retinal architecture remains conserved (Kölsch et al., 2020).

The visual system of the zebrafish (*Danio rerio*) is composed of a complex neural circuitry in which photoreceptor cells convert photons to electrical impulses, leading to the formation of an image onto the retina (Li et al., 2012). The zebrafish retina, like the retina of mammals, including humans, is composed of laminated tissue patterns that is comprised of six types of neural cells. The neural cells are comprised of two photoreceptor cell types: rods and cones, involved in detecting low light intensities and daytime vision respectively. There are three interneurons (horizontal cells (HC), bipolar cells, and amacrine cells) involved in signal propagation. Lastly, the ganglion cells are involved in regulation of axon guidance pathways from the retina to the visual centre (Gramage et al., 2014).

Neural direction-selectivity is one of the main properties of the visual system, responding to visual stimuli in an asymmetrical manner in different directions (Kölsch et al., 2021). Retinal ganglion cells (RGC) detect and implement stimuli of direction and propagate the visual information to higher visual processes in the brain. There are different RGC (**Fig. 3**) that are subdivided according to morphology, physiology, and anatomical features responsible for detecting edges, luminescence, and motion direction to guide perceptual and behavioral function in zebrafish (Park et al., 2016). The localization of the different RGC subtypes is based on a combination of dendritic stratification patterns where the axons extend to arborization fields (neuropils found in the brain nuclei, localized in the pretectum, thalamus, and hypothalamus region), as well as the tectum. The transcription profiling of these subtypes has detected >30 RGC gene markers, displaying different physiological and morphological features conveying the visual information to the specific tectal layers (**Fig. 3**) based on axonal projections and the dendritic stratification (Kölsch et al., 2020). The stratification pattern of the ON and OFF light responses allows the different RGC types, which are sensitive to different visual features, to receive the input of the visual stimuli from distinct interneurons (Kölsch et al., 2020). These structures have different perceptual and behavioral roles in the visual system such as optical flow detection, visual escape, circadian rhythms photo-entertainment, and phototaxis (Orgar, 2016).

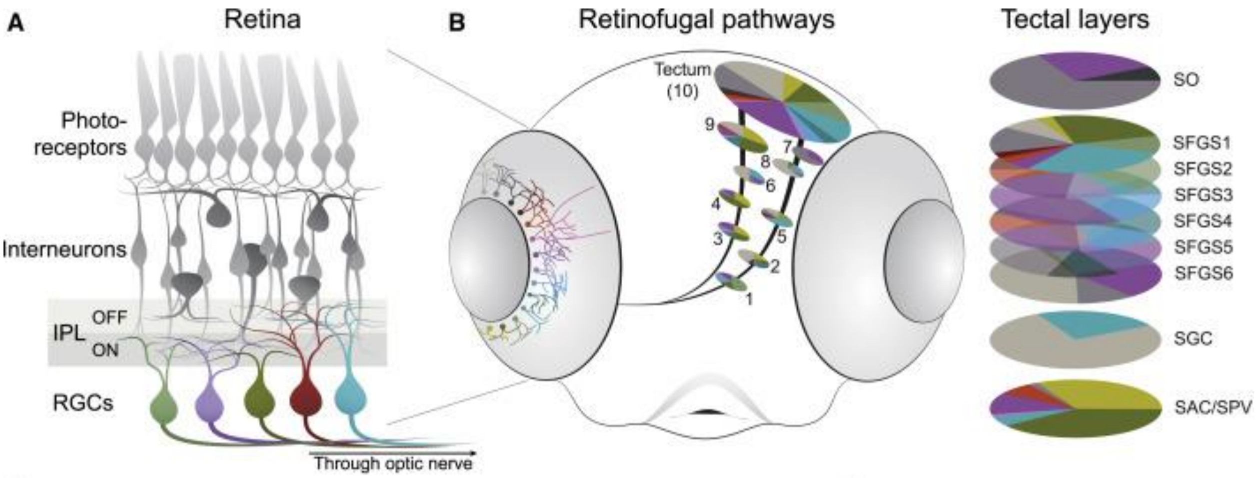

Figure 3. Anatomical characteristics of the zebrafish retina and the layout of the RGCs sending the visual information via the optic nerve to higher visual processes in the brain. The visual system is composed of a stratification pattern in the IPL that is split into light ON and OFF responses. The tectum is the visual centre of the brain, which is in the midbrain, composed of nine to ten laminae where the RGC extend. The position of the arborization field which includes the stratym opticum (SO), stratum fibrosum et griseum superficiale (SFGS), stratum grisem centrale (SCG), and the stratum album centrale/ stratum periventriculare (Image acquired from Kölsch et al., 2020).

1.4. The mechanism of zebrafish larvae's optic flow

Optic flow is the animal's innate self-motion by creating a drifting movement through the visual scene that covers the entire visual field of the organism (Matsuda & Kubo, 2021). The animal can make appropriate decisions regarding adjusting body position, gaze stabilization, and posture with respect to the environment. The pretectum is known to be the relay station in the brain that processes the input of the direction-selective retinal neuron, it also processes complex temporal and spatial visual features that integrate the optic flow response which pertains to behavior (Matsuda & Kubo, 2021). In addition, the cerebellum is involved in representing the motor signals associated with optic flow. In the zebrafish, the neural circuits of processing optic flow are measured in the form of optokinetic response (OKR) and optomotor response (OMR).

The OMR and OKR are both innate swimming responses that the fish exhibits (Matsuda & Kubo, 2021).

1.4.1 Neural network involved in locomotor activity in the zebrafish

In OKR and OMR, the visual information acquired by the visual field through optic flow is detected by the retina and the information is transmitted to visual processing regions of the brain, primarily to the pretectum (Orger et al., 2008). In OKR, the pretectum propagates the signal directly or indirectly to the ocular motor system. This consists of the motor neurons responsible for regulating the extraocular muscles (Orger et al., 2008). In the case of OMR, the medial longitudinal fasciculus (nMLF) of the midbrain and the reticulospinal (RS) system of the hindbrain are the main regions involved that receive the visual signal from the pretectum for regulating swimming through the descending axons that reach the spinal cord (Orger et al., 2008; Thiele et al., 2014). **Figure 4** captures the organization of the optic flow circuitry in the brain of the zebrafish larvae when performing OMR and OKR.

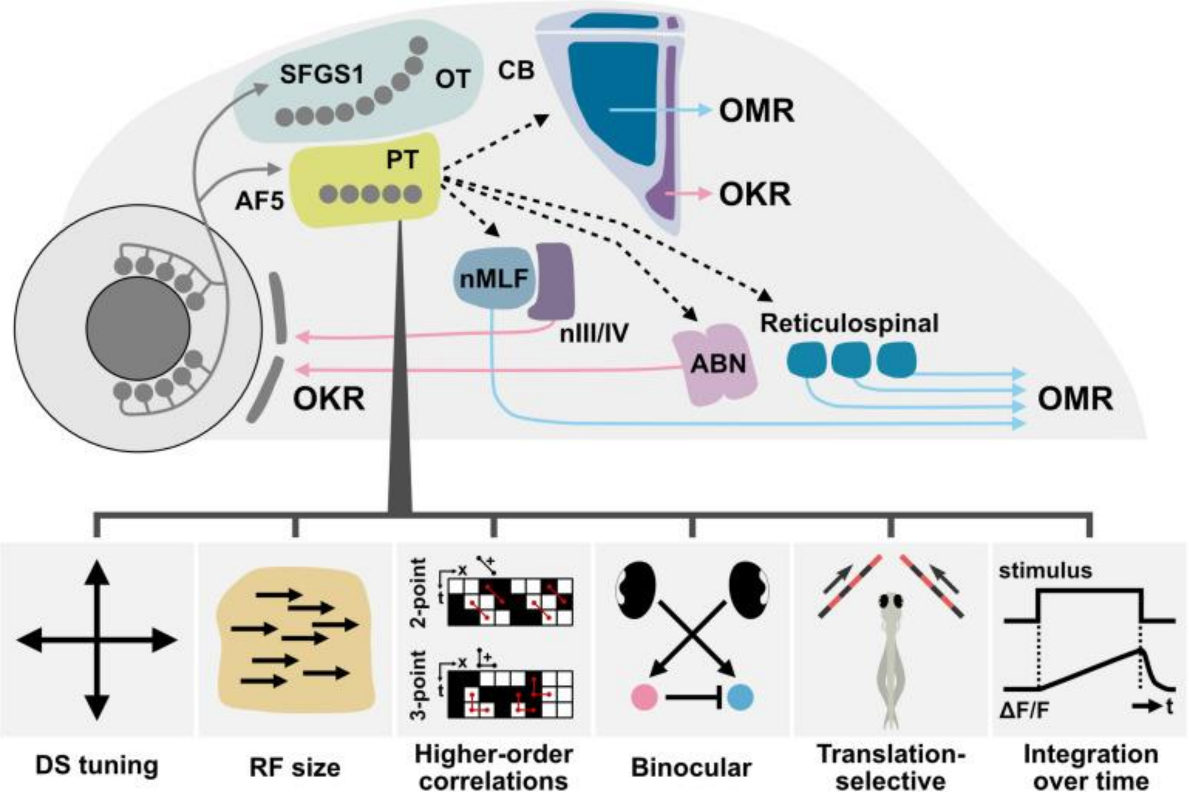

Figure 4. The configuration of the optic flow circuitry in the brain of the zebrafish larvae. The directional selective (DS) of the RGC projects to the optic tectum (OT), specifically to the SFGS1 neuropil layer and the AF5 neuropil layer in the pretectal (PT) region. In OKR, the pretectum propagates the signal either directly or indirectly to the ocular motor system (oculomotor nIII, abducens nuclei (ABN), and trochlear nIV) that consist of the motor neurons that are responsible for regulating the extraocular muscles. In the case of OMR, the medial longitudinal fasciculus (nMLF) of the midbrain and the reticulospinal (RS) system of the hindbrain are the main regions involved that receive the visual signal from the pretectum for regulating swimming (Figure acquired from Matsuda & Kubo (2021)).

1.4.2 The mechanism of saccadic-like eye movements in the zebrafish

The OKR is comprised of two phases **(Fig. 5)**, a slow phase that perceives the tracking motion of the object through a rotating eye movement pattern, as well as a fast phase that creates a fast saccadic eye movement in which the eye returns to its original position after the slow phase (Matsuda & Kubo, 2021). The fast phase, also known as the smooth pursuit of the moving target, helps to re-centre the gaze to maintain a stable vision as the object continues to move (Matsuda & Kubo, 2021). The OKR investigates how the fish stabilizes gaze by generating saccadic-like-eye-movement with respect to optic flow (Matsuda & Kubo, 2021). The OMR is associated with how the fish adjusts its body position and direction of swimming to optic flow. (Orger et al., 2000). Since OKR and OMR are both innate responses, behavioral assays could be conducted at larval stages to test the function of the RGCs output in the retina by analyzing the spatiotemporal nature of light (Muto et al., 2005).

The saccadic drifting evoked by the OKR response of the 5dpf larvae showed that the eye movement shows a faster saccadic drift response from nasal to temporal than the movement from temporal-to-nasal direction demonstrating an asynchronous pattern between the two eyes (Chen et al., 2014). In another study by Chen and colleagues (2016), it was reported that the amplitude of the saccades and the peak velocity of the saccades are higher in the nasal-to-temporal direction compared to the temporal-to-nasal direction. This observation of asynchronous activity can be due to the different firing times of the bursting neuron from each eye exposed to the leftward and rightward moving grating, suggesting the existence of two different neuronal populations for each eye due to having lateral eyes (Chen et al., 2016). Different pathologies can change the frequency, size, and timing of the saccades (Jensen et al., 2019). Depending on which parameters are displaying an abnormal pattern, the pathologies can represent cerebellar disorders and/or neurodegenerative disorders (Kassavetis et al., 2022). The amplitude of the saccades of the eye represents the distance the eye has traveled between two fixation points and the amplitude shows that the eye gaze is closer to the target of interest (Paeve & Laurent, 2011). Abnormal saccadic amplitude is observed in pathological conditions such as saccadic dysmetria where the patient displays short saccades due to monocular muscular weakness (Paeve & Laurent, 2011). The velocity of the saccade is characterized by the duration of generating saccades and abnormal conditions such as slow saccades have been linked to neurological disorders such as progressive supranuclear palsy, affecting the function of the midbrain (Garbutt et al., 2004). The slow saccades can also be linked to spinocerebellar ataxia, an autosomal dominant disorder that has been suggested to be due to reduced activity of the brainstem (Szmulewicz et al., 2011). This can be due to inhibition of the excitatory burst neurons that leads to generating slow saccades both horizontally and vertically (Szmulewicz et al., 2011). In addition, slow saccadic eye movement has also been linked to patients with advanced Parkinson’s disease displaying increased hypometria where they underreach the object of interest during voluntary muscle movement (Garbutt et al., 2004). In this condition, it takes more time to reach the object of interest and as a result, exhibit slow saccades. Slowing of saccades can also be observed in other neurological conditions such as Huntington’s disease, Lewy bodies, and corticobasal degeneration (Jensen et al., 2019). Fast saccades are less common that lead to irregular generation of saccade bursts causing ocular flutter and have been linked to cerebellar disorders as well (Grossman & Rucker et al., 2023). The deficiencies in generating saccadic eye movement are indicative of ocular motor deficiencies which is linked to neurological disorders (Grossman & Rucker et al., 2023).

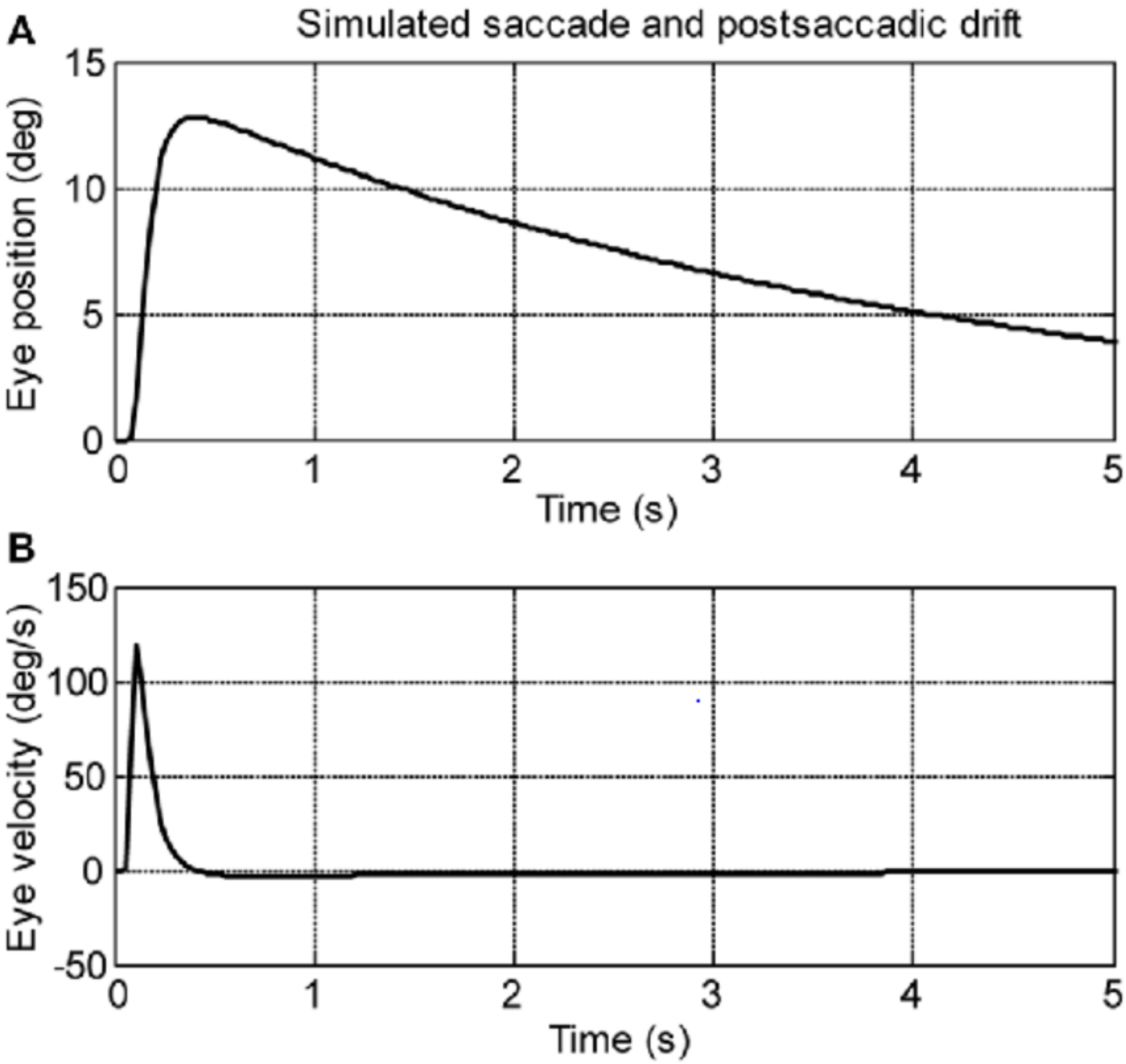

Figure 5. Simulated saccadic-like eye movements in the zebrafish larvae. Saccadic-like eye movements with a saccade lasting around 10-20ms, followed by a post-saccadic-like drift of approximately 5 seconds going back to the resting position. The eye velocity is around 130 deg/s but can go up to 400-500 deg/s depending on the parameters (Figure acquired from Chen et al., 2016).

1.5. Introduction to the habenula and axon guidance pathfinding

The habenula (Hb) region is a conserved structure in a vertebrate's brain and it is associated with emotion-related behaviors via the integration of the basal ganglia and the limbic system which are the upstream region of the Hb (Hikosaka, 2010). Different studies have reported the involvement of the Hb region in fear, anxiety, depression, nicotine withdrawal, and reward processing (Li et al., 2011; Matsumoto, 2007; Yamaguchi et al., 2013). Work done by Agetsuma and colleagues (2010) showed that genetic inactivation of the dorsal Hb leads to an increase in freezing responses to conditioned stimuli. In the rodent model, light contrast sensitivity was associated with tonically inhibiting or activating the neurons in both the lateral and medial Hb (Zhao & Rusak, 2005). Studies by Zhang and colleagues (2017) have also shown that lesions to the left dorsal Hb are associated with regulating light-preference behavior in the zebrafish by receiving the visual information from the specific subtypes of the RGCs via the eminentia thalami (EmT). This innate behavior is crucial for animal survival and inactivation of the left dorsal Hb causes impairment in the retinal input dependent on light luminescence. Another study by Cherng and colleagues (2020) demonstrated that silencing the habenula-interpeduncular nucleus pathway in the zebrafish impairs left-right-dependent decision-making. In addition, changes in light signals can lead to changes to the neural activity of the lateral habenula, disrupting the circadian rhythm activities (Young et al., 2021). The lateral habenula is a region located within an extensive neural circadian circuitry and is regulated by receiving input from the master circadian pacemaker (located in the suprachiasmatic nucleus), retina, and other hypothalamic circadian oscillators involved in the circadian mood and timing (Guilding et al., 2009; Hatings et al., 2018; Poller et al., 2013). Electrophysiology data showed an increase in the burst firing of the lateral habenula which was associated with depression and circadian rhythm disruptions (Cui et al., 2018). Interestingly, the increase in these burst firings in the lateral habenula was associated with an increased expression of astrocytes in this brain region, which implicates the burst firings and changes to circadian oscillations leading to experiencing depression (Cui et al., 2018).

There is a functional lateralization when the circuitry and morphology of the individual neurons of the lateralized habenular nuclei are examined (Bianco et al., 2008). The functional asymmetries of the left side and right side of the brain have shown that is associated with higher cognitive performance, as well as social behavior (Bianco et al., 2008). However, the asymmetrical nature is described when it comes to the level of neurons, shape, and size of neurons in the subnuclear region and this affects the expression of neurotransmitters. However, not much has been focused on the functional circuitry of individual neurons that unravels the underlying left and right differences when it comes to neuronal processing (Bianco et al., 2008). A study by Bianco and colleagues (2008) used the telencephalon-habenulo-interpedunclear system of the 4dpf zebrafish larvae which is a common regional model for investigating the functional connectivity of brain asymmetries due to sharing a unipolar structure. The study found that there are two subtypes of axon arbor where the left-sided and right-sided neurons describe the structure in different frequencies. The study has shown that the distinct composition of the cell types explains the asymmetrical circuitry of the left and right habenula. In addition, when the projection and structure of the individual post-synaptic neurons were analyzed, it was suggested that the nucleus is capable of integrating the right and left input together or integrating them separately and as a result relaying the input of the left and right habenula through down-stream pathways and preserving the right and left coding at a single project axonal neuron (**Fig. 6)**. For the habenula to regulate circadian rhythms and mood, it needs to form precise neural connections and hence depends on axon guidance mechanisms.

Throughout development, all axons are guided to the appropriate targets with the help of guidance molecules. Axons go through complex pathways to reach their destination and based on these guidance cues, the tip of the axons or the growth cone gets repelled or attracted towards precise directions for their specific neural connection (Tesssier-Lavigne & Goodman, 1996). The retinotectal projection of zebrafish forms the retinal ganglion cells (RGC) in the eye, and the extended axons (which regulate the neuronal cytoskeleton) interconnect with the optic tectum. The axons of the RGCs grow in a way that reaches the optic disc, then leaves the eye and connects with the optic nerve, extending to the optic chiasm (Tesssier-Lavigne & Goodman, 1996). The inner retina is interconnected with the pretectum, habenula (Hb), and optic tectum involved in circadian rhythmicity, regulating light sensitivity, as well as locomotion in the zebrafish larvae (Safarian et al., 2021).

There are essential axon guidance molecules such as semaphorins, netrins, slits, and ephrins which are involved in directing the habenular axons through specific pathways interconnecting the habenula with different brain regions. and the retina for properly integrating visual inputs to elicit a behavior response (Bianco et al., 2008).

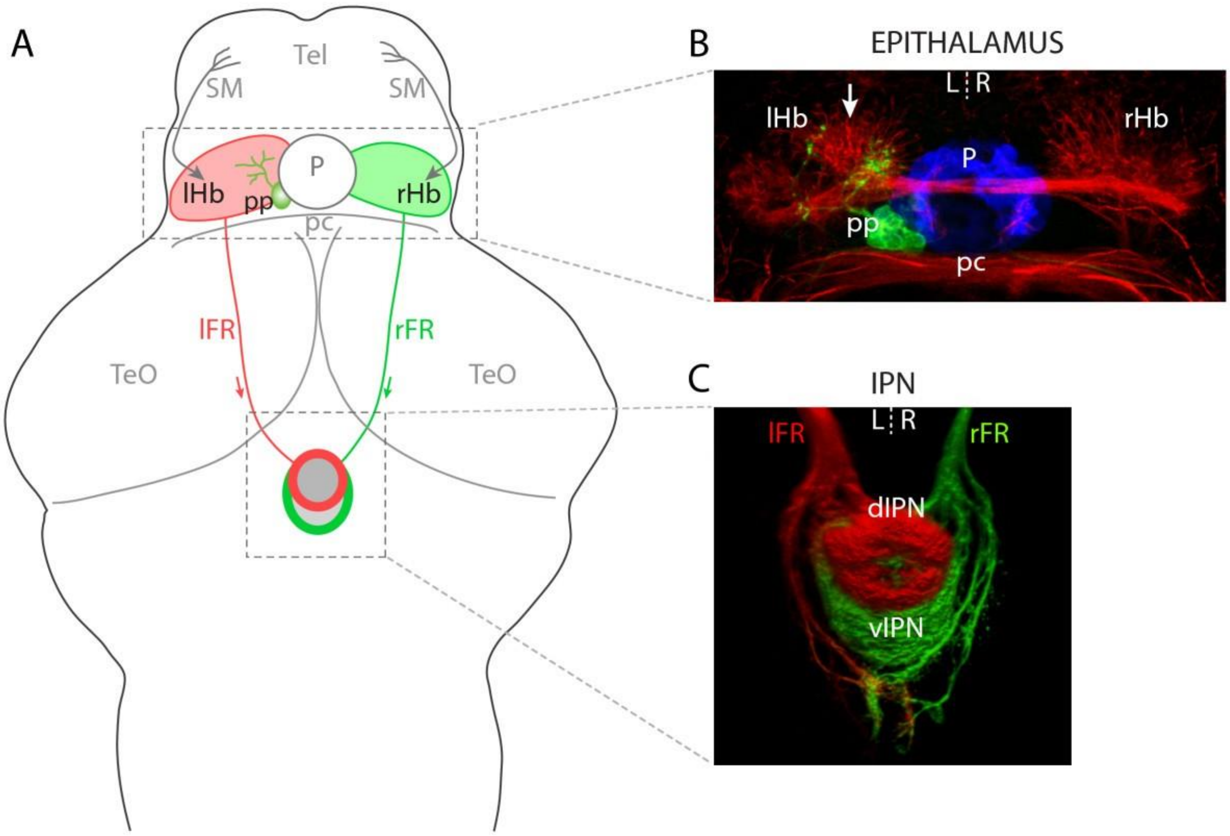

Figure 6. Schematic representation of the asymmetrical nature at the level of the morphology of axon terminal of the left-right telencephalon-habenula-interpeduncular nucleus pathway. A) The bilateral paired habenular (Hb) of the 4dfp zebrafish larvae receiving the afferent signal from the Hb nuclei to the Tel (telencephalon) through the stria medullaris (SM). The efferent signal of the habenula neurons goes through the fasciculi retroflexus (FR) to the interpeduncular nuclei (IPN) through the ventral midbrain. B) The neuroanatomical asymmetrical structure depicted with the anti-acetylated tubulin antibody staining showing the left habenula contains a higher density of neuropils. C) 3D structure of the ventral midbrain showing the habenular axon terminals using lipophilic dyes (Figured acquired from Bianco et al., 2008).

2. Research design and thesis aim

This thesis aims to address the gaps in knowledge related to the functional role(s) of Panx1a and Panx1b in the physiology of the zebrafish larvae visual system. This project is a continuation of the work done by Safarian and colleagues (2021) that the Panx1b knockout fishline has problems with navigating leftward motion in low light conditions using OMR. In addition, the Panx1b was suggested to be a modulator of the circadian clock system and regulate the luminance response of zebrafish larvae (Safarian et al., 2021). The loss of Panx1a in zebrafish larvae also led to changes in visuomotor behavior and was associated with light decrement detection and abnormal responses to visual stimulus through the retinal OFF-pathway via dopaminergic and adenosine signaling pathways (Safarian et al., 2020). The inner retina is interconnected with the pretectum, habenula (Ha), and optic tectum involved in circadian rhythmicity, regulating light sensitivity, as well as locomotion in the zebrafish larvae (Safarian et al., 2021). **Figure 7** provides an overview of the retinal ganglion cell ends connecting to the habenula, this illustrates the connection of the habenula with the axon projections linking to the retina. The images derive from the MapZeBrain atlas, which includes connectome information.

The hypothesis of my thesis was that Panx1a and Panx1b modulate the axonal growth in axon guidance pathfinding and together are interconnected to the habenula region, leading to synaptic plasticity of the retinal neural circuitry, and regulating visually guided locomotion in the zebrafish larvae.

This project was designed to investgiate the larvae's optic flow response to their biased direction selectivity in the Panx1a-KO and Panx1b-KO fish lines at the molecular, systems, and behavioral levels.

The specific aims were:

- Investigating the development of the axon guidance pathfinding genes during the early stages of the zebrafish larvae on a molecular level by performing RT-qPCR of the axon guidance pathfinding genes and analyzing RNA-seq data. The goal was to see if there is abnormal regulation of these genes during the early stages of larval development in the Panx1a-KO and Panx1b-KO fishlines compared to the TL.
- To investigate the saccadic eye movement of the 6dpf Panx1a-KO and Panx1b-KO larvae compared to TL using OKR which tests the function of the RGC response and see whether the fish exhibit ocular motor deficiencies and/or if they can follow the direction of the motion. The strategy aimed at understanding the kinematic properties of eye movement in the knockout fishlines by exposing the fish to three different contrasts, three different spatial frequencies, leftward and rightward directions of moving grating, and a constant speed to evaluate the response of their eye movements.
- To investigate the OMR response to see whether Panx1a-KO and Panx1b-KO fishlines exhibit directional bias when exposed to leftward and rightward moving gratings.
- The last goal was to perform immunohistochemistry to determine whether Panx1a and Panx1b co-localize with the habenula region. The approach was to use custom-made antibodies to perform double-staining immunohistochemistry followed by image analysis using intensity plots and Manders colocalization

coefficient analysis to quantify the fluorescent intensity overlap between the two channels.

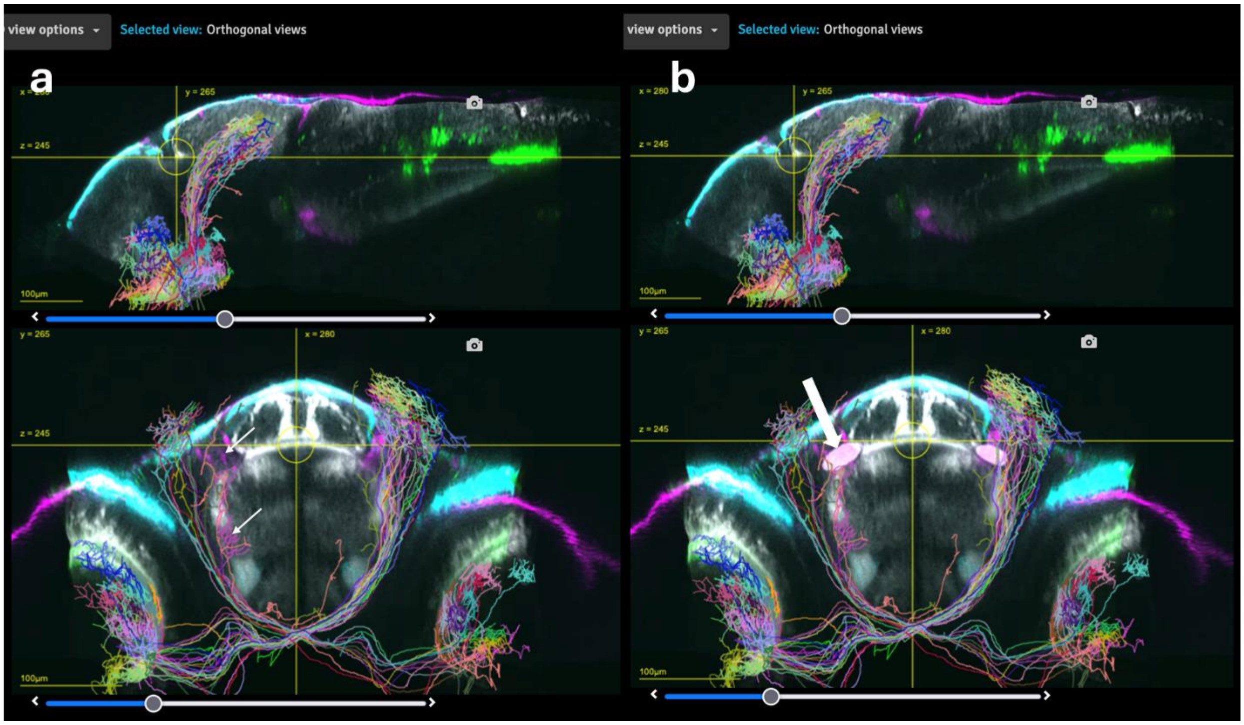

Figure 7. Overview of axons projecting from the retinal ganglion cells (in pink color) ending in the habenula (white color). a) Illustrates the synaptic end contacts (in pink color) pointed with white arrows from the retinal ganglion cells ending in the habenula. b) The ROI has been added to the image on the right illustrating the location of the habenula (in white color) pointed with a white arrow. *(*Figure acquired from https://mapzebrain.org/).

3. Materials

3.1. Abbreviations used for the model organism, the generation of the KO fish lines, and biosafety

Zebrafish *(Danio rerio)* Tupfel long fin (TL) was used as the model organism for the study. The unmodified strains of TL were considered as the wild-type or the control line. The Pannexin1 (Panx1) KO transgenic fish lines are referred to as Panx1a$^{-/-}$ and Panx1a-KO in text as the fish line that does not have a functional Panx1a channel (Panx1a$^{-/-}$: Panx1b$^{+/+}$), and Panx1b gene transgenic lines (Panx1b$^{-/-}$: Panx1a$^{+/+}$), as well as the double knockout (DKO) transgenic fishline that does not have a functional Panx1a and Panx1b (Panx1a$^{-/-}$: Panx1b$^{-/-}$). Knockout transgenic fishlines were produced in-house (See Safarian et al., 2020; Safarian et al., 2021) using TALEN technology, and each fish line was bred till the 3rd generation before conducting experiments on the larvae.

All laboratory experiments were conducted in a level two laboratory setting as per institutional and provincial safety standards. WHMIS II, Biosafety hazard training, and autoclave training were required before starting experimental research. In addition, prior to working and handling animals, the completion of the animal care and training certificate was required before accessing the vivarium facility. This certification adheres to the regulations set by the Canadian Council for Animal Care. The protocol was approved by the Animal Care Committee before work with animals started (GZ: 2019-7-R2 and GZ: 2020-7-R3).

3.2. Reagents and chemicals

3.2.1 Reagents for handling the larvae

Solutions	Composition	Source
E3 Medium	60ppm of Instant Ocean$^{@}$ Sea Salt combined with RO water (pH 7.2-7.4)	Instant Ocean$^{@}$

3.2.2 Reagents and solutions for molecular biology

PROTOCOL	REAGENTS	SOURCE
TISSUE LYSIS & RNA EXTRACTION	RLT Plus Lysis Buffer, βME, RPE Wash Buffer, RW1 Wash Buffer, RNase-free water, 70% Ethanol	QIAGEN (RNeasy Plus mini kit)
DNA/RNA VISUALIZATION	Agar, Formaldehyde, 1x TAE Buffer, 100bp DNA Ladder, EtBr	ThermoFisher Scientific
CDNA SYNTHESIS	iScript Reverse Transcriptase, 5x iScript Reaction Mix, Nuclease-free water	Bio-Rad
18S PCR PRODUCT	HotStarTaq DNA Polymerase, dNTPs, 10mM 10S FP and RP solutions, 1x PCR Buffer, Nuclease-free water	QIAGEN (HotStar Taq Pl Kit)
RT-QPCR	Ssofast^{TM} EvaGreen ®	Bio-Rad

3.2.3 Solutions for Immunohistochemistry (IHC) and whole mount IHC

Reagents	In-text appearance	Source
4% Paraformaldehyde	4% PFA	Sigma-Aldrich
OCT Medium	OCT	cat#95057-838
DAPI	DAPI	Vector
Potassium hydroxide	KOH	Sigma-Aldrich
Sodium Phosphate Dibasic Anhydrous	Na_2HPO_4	Fisher BioReagents
Methanol	Methanol	CALEDON
Glycerol	Glycerol	Fisher Scientific
Potassium phosphate monobasic	KH_2PO_4	Sigma
Potassium Chloride	KCl	Fisher BioReagent
Sodium Chloride	NaCl	Bioshop

3.4. Oligonucleotides

3.4.1 Primers designed for RT-qPCR

The sequences of the desired genes were obtained from NCBI (https://www.ncbi.nlm.nih.gov/). The gene accession number was acquired from the website. The FORWARD and REVERSE primers were generated using IDT (https://www.idtdna.com/pages). The sequences were then added to SnapGene Viewer software to map and annotate the features of the genes for amplicon sequencing to target our specific genomic region.

Table 3. Summary of primers used for conducting RT-qPCR.

Gene Name	**Gene Accession Number**	**Forward Primer (5'-3')**	**Reverse Primer (3'-5)**
cdk5	NM_131719	TTAAACCACAAAACCTGCTCATC	AGCACCAAACAGTACATCCG
dpysl3	NM_001020512	TGTTTGTGGCTGTGACGAG	GATGTGTTTTGGCAGTGATGG
plxna4	NM_001004495	GAACACTGGTGACTATCCGTG	CCGCTTTTCCCATTTCACAC
plxna3	NM_001098489	GCTGTTTATAAAGGCATCCCG	GTGTTCAGTCTCTTCCAGTCG
plxna2	XM_684688	AAGTCTGGCATCTGGTGAAG	AAAGAGTCTCGAACAGGTCATC
nrp1a	NM_181497	CAAATGATCCTTCGTTCTGCG	GTAGATGAAGTTCCCTGATCCG
nrp2b	NM_212966	GGATGAGAATGGAGATACTGGC	CACCCAGAGACGAAAGAGTAG
efnb3a	XM_687578	GACCTAACAGCAAAATCCCAG	ATCACAATGGCGATCAGTAGG
efnb3b	NM_131806	ATCATTGCTACATCAGACGGG	GGTTTTGGAGATTTGGCTGG
robo2	XM_021481461	TGGGAGAAGTTATTGTGCGG	TCTGCCTGTACAAAACCCTG
sema3aa	NM_131060	ACTTCATGGGACGAGACTTTG	CTTCAGGATTATCGCTCCG
sema3ab	NM_131061	TCCCGATACTTTCCAACAGC	ACAGTCTTATCCAGCAAGCC
slit2	NM_131735	AAGACTACCGCTCAAAACTAGG	GCTGTATACTGAGGGATGTGG

3.5. Antibodies used for IHC

Table 4. Summary of antibodies used for conducting Immunohistochemistry.

Primary Antibody	**Company**	**Primary Antibody Species**	**Secondary Antibody**	**Secondary Antibody Species**	**Dilution Concentration (µl)**	**Structure**
ZN-12 (ANZN-12)	ZIRC	Mouse Monoclonal Antibody	Alexa 488/568nm	Goat anti-mouse	1:200	Amacrine Cells, Inner Nuclear Layer, Inner Plexiform Layer, & Ganglion Cells
ZN-8 (ANZN-8)	ZIRC	Mouse Monoclonal Antibody	Alexa 488/568nm	Goat anti-mouse	1:200	Ganglion Cells, Ganglion Cell Axons, and neuronal cell surface marker
Panx1a	DAVIS	Rabbit Polyclonal Antibody	Alexa 488/568nm	Goat anti-rabbit	1:50	Horizontal cells & ON/OFF GCL
Panx1b	DAVIS	Rabbit Polyclonal Antibody	Alexa 488/568nm	Goat anti-rabbit	1:50	Ganglion Cells & Muller Glia Cells
GFAP (Zrf1)	ZIRC	Mouse Monoclonal Antibody	Alexa 488/568nm	Goat anti-mouse	1:200	Muller Glia Cells
Acetylated Tubulin	Sigma	Mouse Monoclonal Antibody	Alexa 488/568nm	Goat anti-mouse	1:400	Habenula and axonal tract

3.6. Hardware Instruments

3.6.1 Summary of equipment used for molecular RT-qPCR.

Protocol	*Equipment*	*Source*
Tissue lysis	TissueLyser LT Adapter, 12-tube	QIAGEN
	Sorvall™Legend™Micro 21R Microcentrifuge	Thermo Scientific
RNA extraction	QIAcube	QIAGEN
cDNA PCR	Mastercycler® nexus	Eppendorf, Canada
RNA & DNA visualization	Nanodrop 2000 Photospectrometer	Thermo Scientific
	Mini-Sub Cell GT System	Bio-Rad
	AlphaImager™ HP System	Alpha Innotech
RT-qPCR	CFX96™ Real-Time PCR Detection System	Bio-Rad

3.6.2 Summary of equipment used for performing OMR and OKR on 6dpf larvae.

Protocol	*Equipment*	*Source*
OMR	DESKTOP-VKER083, Intel®Core™ i7-3740QM CPU	DELL
	35mm/F1.65 59872	EDMUND OPTICS
	ASUS P3B 800-Lumen LED portable projector	SonicMaster
OKR	DESKTOP-14H0H9V, Intel®Core™ i7-9700 CPU	DELL
	DESKTOP-VKER083, Intel®Core™ i7-3740QM CPU	DELL
	OLED	AliExpress
	55mm/F2.0 59873	EDMUND OPTICS

3.6.3 Summary of equipment used for Immunohistochemistry

Protocol	Equipment	Source
IHC	LSM 700 T-PMT Microscope	ZEISS
	DESKTOP-14H0H9V, Intel®Core™ i7-9700 CPU	DELL

3.7. Software

3.7.1 Software utilized for molecular RT-qPCR

Application	Software
Gene sequence retrieval	NCBI-nucleotide
Primer Design	IDT-RealTime qPCR tool
Primer location	SnapGene Viewer 5.3.2
RT-qPCR data acquisition	CFX Manager software™
Relative expression analysis	REST 2009 ©

3.7.2 Software used for RNA-seq

Application	Software
Pre-processing of p-adjusted values (<0.01)	Excel (2016)
Figure generation	GraphPad Prism 10.2.3

3.7.3 Software used for OMR and OKR

Application	Software
Pre-processing and cleaning the files to analyze certain parameters	Excel (2016)
Video analysis of eye movement and body movement	Stytra 0.8
Figure composition and statistical analysis	GraphPad Prism 10.2.3

3.7.4 Software used of IHC

Application	Software
Image processing of IHC samples	ZEN Software
Channel adjustments and scale bar	ImageJ
Image configuration	PowerPoint (2016)

4. Methods

4.1. Zebrafish Acquisition

All zebrafish lines were maintained at 28° raised in 14 hours of light cycle and 10 hours of dark cycle period. To generate Panx1a knockout, Panx1b knockout, and double knockout (DKO) fish lines, the Tupfel long fin (TL) zebrafish were used. TALEN technology was used to generate the mutations. The DKO fish model does not have a functional Panx1a and Panx1b channel. Animal regulations took place at the zebrafish vivarium facility in the S2 biosafety laboratory at York University. All policies are according to the Canadian Council for Animal Care (CCAC) guidelines after acquiring approval from the Animal Care Committee (ACC) protocols (GZ: 2020-7-R3).

4.2. Tissue Fixation, Tissue Embedding, & Tissue Sectioning

Tissues were fixated with 4% Paraformaldehyde (PFA) for 5 days at the 4° fridge, followed by an overnight fixation with 15% sucrose, and another overnight fixation with 30% sucrose the following day. An OCT medium (obtained from VWR clear Frozen Section Compound, cat#95057-838) was used for freezing the tissues at room temperature (RT).

A Cryotome FSE machine (serial#CC0220C0904) acquired from ThermoSCIENTIFIC was used to cut 15µm tissue slices. The settings were adjusted to the cryobar being -19°, tissue cryosection to 15µm, chamber to -20°, and specimen temperature was set to -20°. After tissue cutting was done, the tissue slices were stored at the -80° freezer for long-term storage.

4.3. Immunohistochemistry Assay & Microscopy

The tissue slides were taken from the -80° freezer. To eliminate unwanted debris, the tissues were placed in 1xPBS medium (obtained from 100ml of 10xPBS, 900ml of distilled water, and 2ml of 0.1% Tween®20). The tissues were washed 3x for 5 minutes for a total of 15 minutes of washing with 1xPBS. The tissues were then placed in a moist chamber and an antibody dilution blocker was added to each slice. Tissues were left at RT for an hour. This was followed by another 3x wash with 1xPBS and then placed in the wet chamber and the primary antibody was applied onto the tissues and left at 4° fridge for 2 hours. Afterward, another 3x wash with 1xPBS, and then the secondary antibody was applied. Slides were kept in the dark at RT for an hour. This was followed by the last 3x wash with 1xPBS and one wash with distilled water to wash out the ions. 10µl DAPI was applied onto the tissues to stain the nuclei and microscopic cover glass (18x18mm) was placed onto the tissue slides. The LSM 700 laser scanning microscope was used to visualize the staining and ZEISS ZEN software was used to capture the high-resolution images (2048x2048 pixels). The **Figure 8** illustrates a bigger picture of the entire procedure from cutting the tissues and then staining it with primary antibody, followed by tagging with the florescence secondary antibody, and then visualizing under the confocal microscope.

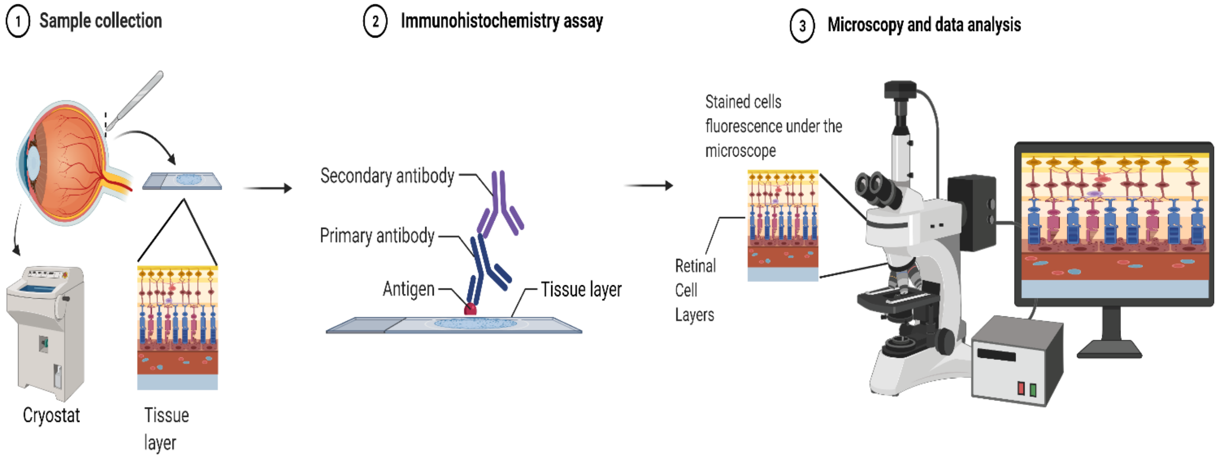

Figure 8. Workflow summary outlining the immunohistochemistry protocol.

4.4. Optomotor Response (OMR)

A custom-made OMR setup was built to perform OMR assay. The moving grating stimulus was projected onto the plates via ASUS P3B 800-Lumen LED portable projector. The moving grating was recorded by presenting a moving grating stimulus in binary sequences of black and white or gray and white stripes using two different speeds (72 and 144 pixels/second), three different spatial frequencies (64, 128, and 256 pixels/cycle), and contrasts 10 and 100 using a moving grating program that was programmed onto the computer using python. The videos were taken at a rate of 70 frames per second (fps) 30-second intervals videos were recorded with 4 larvae at a time. The larvae used in this study were 6dpf. The videos were taken using a USB 3.1 high-speed camera (XIMEA GmbH from Germany) containing a 35mm/F1.65 59872 lens to prevent infrared illumination. All the videos acquired from OMR were analyzed using Stytra (acquired from https://portugueslab.com/stytra/) which is a python-based software used to analyze the body movement and behavioral movement, giving an excel file as an output for further analysis.

4.5. Optokinetic Response (OKR)

A setup like OMR was used for the OKR assay except with a different lens and parameters (**Fig. 9**). A different lens was used to investigate the eye movements of the larvae (55mm/F2.0 59873, acquired from EDMUND OPTICS). The videos were captured at 40fps. A constant speed of 0.01 degree/second was used to evoke an OKR response and 60-second videos were recorded. For the OKR analysis, the OKR response was captured at three different contrasts (20%, 50%, 100%) and three different spatial frequencies (0.2 cycle/degree, 0.15 cycle/degree, 0.1 cycle/degree). For OKR, 6dpf larvae were used for the experiments, and in each run, 1 larvae was placed in a plate and was mobilized with 6% methylcellulose under the OKR camera. All the videos acquired from OKR were analyzed using Stytra (acquired from https://portugueslab.com/stytra/) to investigate the eye movement pattern, giving an Excel file as an output for further analysis.

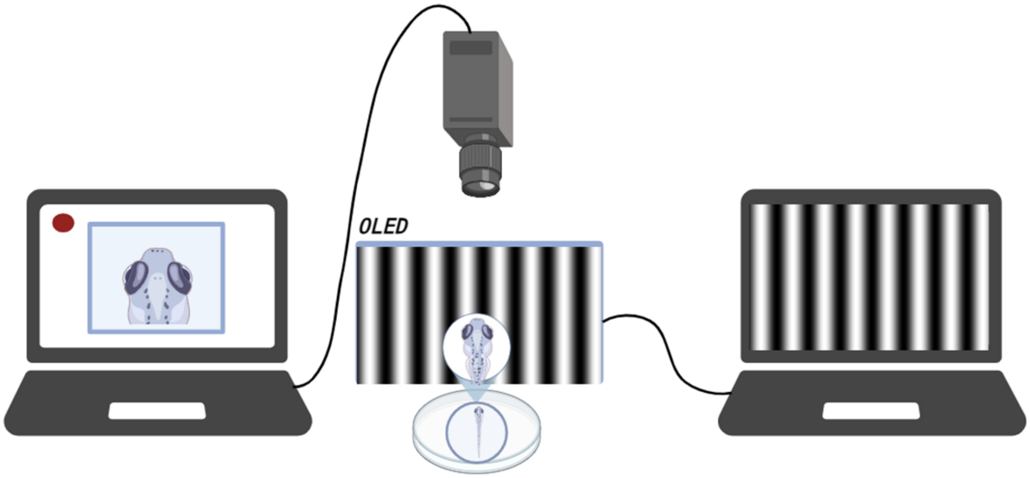

Figure 9. Workflow summary outlining the OKR protocol.

The Python code was created using Psychopy:

```
from psychopy import visual, core, event
# Create a window (full screen)
win0 = visual.Window([1000, 800], screen=0, monitor='testMonitor', color=[0, 0, 0], units='deg')
# Get the screen dimensions
screen_width, screen_height = win0.size
# Create a grating stimulus that covers the whole screen
grat_stim = visual.GratingStim(win0, tex='sin', units='deg', pos=(0.0, 0.0), size=(screen_width, screen_height), sf=0.1, ori=0.0, phase=0.0, contrast=1.0)
# Variable to control animation
running = True
left_moving = True
while True:
    for key in event.getKeys():
```

```
        if key == 'space':
            running = not running  # Toggle the animation on and off
        elif key == 'escape':
            win0.close()  # Close the window if 'escape' is pressed
        elif key == 'left':
            left_moving = True  # Set grating direction to left
        elif key == 'right':
            left_moving = False  # Set grating direction to right
        elif key == 'up':
            grat_stim.contrast += 0.1  # Increase contrast by 0.1
        elif key == 'down':
            grat_stim.contrast -= 0.1  # Decrease contrast by 0.1
            grat_stim.contrast = max(0.0, grat_stim.contrast)  # Ensure contrast is not negative
    if running:
        if left_moving:
            grat_stim.setPhase(0.01, '-')
        else:
            grat_stim.setPhase(0.01, '+')
        grat_stim.draw()
        win0.flip()
```

4.6. RNA extraction, cDNA Synthesis, & 18s control PCR

In order to extract RNA, 30 6dpf larvae were collected in 2ml tubes and stored in -80° freezer. Metal beads were added to the 2ml tubes containing 30 larvae. The following solutions were added to the 2ml tubes with metal beads and 30 larvae: 350µl RLT, 3.5µl BME (solutions acquired from the RNeasy Plus Mini Kit (#74134). The tube was lysed at 50Hz for 3 minutes in the tissue lyser. To get rid of the foam created by lysing, the tubes were spun down at 13k rpm for 3 minutes. The supernatant was transferred to a fresh 2ml tube and placed in the Qiacube machine. Once the preparation was completed, the tubes were collected and the optical density (the measurement of OD absorbance ratio at wavelength 260-280 nm was measured) was used to see how much RNA was extracted from each sample tube. The measurements should ideally be around 200 ng/µl.

To check the purity of the RNA samples a 2% agarose gel was cast with TAE to make sure there was no contamination in our samples. 2% agarose with TAE was used to make a gel with wells. In each well, we had 200-500 ng/RNA in 4µl of H_2O. The tubes were heated at 55° for 10 minutes and then 1µl stop mix with EtBr was added to each tube. Each sample was assigned a well for 40 minutes at 80V. After checking the purity, the RNA tubes were stored in -80° freezer.

From the script cDNA synthesis kit, Bio-Rad, 170-8890, 0.5ml PCR tubes were acquired. The following solutions were added for cDNA synthesis: 1µl RNA, 4µl 5x iScript buffer, 1µl reverse transcriptase, and topped with 20µl of PCR water. Once the solution was made it was placed in the PCR machine for about 48minutes of run-time. Samples were followed by a short spin and 30µl of H_2O was added to each tube for a total volume of about 50µl per tube and stored at -20° freezer.

The following solutions were added to 0.5ml tubes: 17µl of H_2O, 2µl 10x buffer, 0.4µl dNTPs (10µM), 0.5µl primer mix (10µM each), 0.1µl Taq Polymerase for a total volume of 20µl per tube. Afterward, 1µl of cDNA was added to each tube and placed in the PCR machine (CFC connect real-time system, Bio-Rad) for about 17 cycles. After running the 18s PCR, a gel was cast to see whether the cDNA contained any contamination. 2% agarose in a 40ml test tube was poured and 3ml of EtBr was added in the tube. Afterward, 10µl of the solution was added to the wells, and the gel was left to run for about 30 minutes.

4.7. RT-qPCR

For the RT-qPCR 69 well plates were used. The following solutions was added to 0.5ml tubes: 2x Sybr 5µl, 0.25µl of prediluted primer, and 4.75µl of H_2O for a total of 10ml mixture. This is followed by adding 1µl of cDNA. The mixture was pipetted with filter tips onto the well plate 10µl for each well. The wells were placed in the PCR machine, the RNA was analyzed in triplicates by RT-qPCR using the CFX Manager Bio-Rad software. The primers used in the study were designed for RT-qPCR. The NCBI was used to acquire genomic information (https://www.ncbi.nlm.nih.gov/). The gene ID was acquired from the website and pasted onto IDT and the FORWARD and REVERSE primers were generated by the website (https://www.idtdna.com/pages). The sequences were then added to SnapGene Viewer software to map and annotate the features of the genes for amplicon sequencing to target our specific genomic region. RT-qPCR could be done once the primers were designed and ordered from IDT.

4.8. RNA-Seq analysis of Panx1a, Panx1b, and DKO 6dpf fish line

All the transcriptome of the RNA-seq analysis for all the zebrafish lines (Panx1a, Panx1b, and DKO) was done by the Centre for Applied Genomics (SickKids, Toronto, Canada). Moreover, to find the genes that are involved specifically with axon guidance, retinal axon guidance, synapse, axon, and dendrite the ZFIN (https://zfin.org/) database was used. Both the gene lists acquired from ZFIN and the RNA-seq data were added to an Excel file and using conditional formatting, the regulated genes involved with each process were filtered.

4.9. Whole-Mount Immunohistochemistry

Fix larvae in 4% PFA in PBS (pH 7.4) overnight (O/N) at 4°C. Before beginning the rest of the protocol, the larvae should be transparent; Hence, tissue clearing is performed with H_2O_2. The protocol is as follow: 3ml H_2O_2 + 47ml H_2O to obtain 3% H_2O_2. 12.5ml of the 3% H_2O_2 is combined with 0.7g KOH and topped with fresh egg water for a total of 25ml and this solution is used to make the larvae transparent. Afterward, wash with 1xPBS three times (5 min each). Dehydrate larvae through a graded 25 % methanol in 1XPBS, 50% methanol in 1XPBS, 75% methanol in 1XPBS, and 100% methanol in 1XPBS respectively (5min in each solution). Afterward, transfer larvae to fresh 100% methanol in 1XPBS and store O/N (or for months) at -20°C.

The next day or anytime after, rehydrate larvae through graded methanol in 1XPBS series: 75%, 50%, and 25% respectively, each solution for 5min. Following that wash the larvae with 1xPBS 0.1% Tween (1xPBSTw) medium (obtained from 100ml of 10xPBS, 900ml of distilled water, and 2ml of 0.1% Tween®20) three times for a total of 15min. In order to retrieve the antigen, wash larvae with Tris buffer (150mM Tris-HCL, pH 9.0) for 5 min. This is followed by equilibrating the larvae in Tris buffer at 70°C for 15min. After this procedure, larvae were washed two times with 1xPBSTw for a total of 10min. To permeabilize the tissues, wash larvae three times with distilled water on ice for a total of 15min. Soak with prechilled acetone (stored at -20°C) for 20min. Rinse the larvae with distilled water for 5min and this is followed by rinsing twice with 1xPBSTw for a total of 10min. To block unspecific binding incubate larvae in 10% BSA in 1xPBSTw for 1-2h at RT or O/N at 4°C. Next, Incubate the larvae with primary antibody diluted in 1% BSA in 1xPBSTw at least O/N on a rocking table (Have a negative control with only 1% BSA). After incubating, wash the larvae four times with 1xPBSTw for a total of 20min.

This is followed by incubating the larvae with a secondary antibody diluted in 1% BSA in 1xPBSTw for 4h at RT or O/N at 4°C fridge. Wash the larvae four times with 1xPBSTw for a total of 20min and then rinse three times with 1xPBS for a total of 15min. Finally, wash in a series of glycerol in 1xPBS: 25%, 50%, and 75% glycerol in 1xPBS respectively (20min in each solution) and then transfer to 100% glycerol in 1xPBS and store at 4°C fridge till imaging day.

4.10. Statistical analysis of behavior studies

To quantify the OMR and OKR percentage of positive response, a non-parametric one-way ANOVA (Kruskal- Wallis) test was used to compare the two treatments (Panx1a$^{-/-}$, Panx1b$^{-/-}$) to the control condition (TL) using GraphPad Prism 10.2.3. This test was appropriate for three independent groups assuming the data is not normally distributed. The Kruskal- Wallis test was followed by a Dunn's test which is a common post-hoc test used for non-parametric pairwise multiple-comparison to see the mean rank of which specific group differs significantly from the control group (https://www.graphpad.com/guides/prism/latest/statistics/stat_nonparametric_multiple_compari.htm) For the statistical analysis of the OKR parameters, a parametric one-way ANOVA followed by a Dunnett test has been conducted for the significance of the findings (https://www.graphpad.com/guides/prism/latest/statistics/stat_the_methods_of_tukey_and_dunne.htm). This analysis was appropriate to compare multiple treatments against the control group assuming normal distribution and equal variances among groups.

For representing the significance of the findings based on the statistical test conducted (non-parametric one-way ANOVA and parametric one-way ANOVA), (ns) is indicative of the findings being non-significant, a P-value less than 0.05 is indicated with (*), a P-value less than 0.01 is represented by (**), P-value less than 0.001 is (***), and P-value less than 0.0001 represents a significance by (****). For each independent condition, (n = 12) larvae were used for each genotype. A sample size of 12 was used for each genotype from each condition.

4.11. Statistical analysis of immunohistochemistry double staining colocalization

To examine the fraction of fluorescent intensity in pixels and measure the colocalization of the proteins according to their channel, a Manders Colocalization Coefficient analysis (Manders et al., 1993) was conducted in ImageJ. There are two coefficients used in Manders: M1 coefficient, which represents the fraction of intensity of the red fluorescence channel overlapping with the green fluorescence channel, and M2 which illustrates the green fluorescence in regions with red fluorescence (Manders et al., 1993). A Mander’s coefficient that is above 0.5 represents a significant overlap where more than 50% of the signal from one channel overlaps with the other channel and as a result shows a substantial colocalization.

5. Results

5.1 Panx1a & Panx1b expression overlap within the Habenula region, arborization field, optic nerve, & optic chiasm

6dpf TL (Wild-type strain) was used to perform immunohistochemistry for potential co-localization of Panx1a and Panx1b with other antibodies. The heads of the larvae were fixated, embedded, and cut with 15µm thickness. The one-day immunohistochemistry protocol was used to perform the double staining of polyclonal rabbit Panx1a or Panx1b with a monoclonal antibody, followed by an intensity plot analysis to examine the regional overlap. All images were captured using the ZEISS LSM 700 microscope and further processed using the ZEN software, followed by ImageJ for further processing. To examine the fraction of fluorescent intensity in pixels and measure the colocalization of the proteins according to their channel, a Manders Colocalization Coefficient analysis (Manders et al., 1993) was conducted in ImageJ. There are two coefficients used in Manders; M1 coefficient, which represents the fraction of intensity of the red fluorescence channel overlapping with the green fluorescence channel, and M2 which illustrates the green fluorescence in regions with red fluorescence (Manders et al., 1993). A Mander colocalization coefficient that is above 0.5 represents a significant overlap where more than 50% of the signal from one channel overlaps with the other channel and as a result shows a substantial colocalization.

The expression of Panx1a can be seen in the brain and the retina (**Fig.10**). The Panx1a is expressed in the horizontal cell layer (HC) and the ON and OFF ganglion cell layer, as previously stated (Safarain et al., 2020). The Panx1a also stains the habenula (Hb) and the arborization fields (AF). The Panx1b protein is expressed in the horizontal cell layer, ganglion cell layer, as well as the end feet of the muller glia astrocytes as previously published (Safarain et al., 2021). The Panx1b protein is also found in the optic chiasm, arborization fields, as well as the habenula (**Fig.11**).

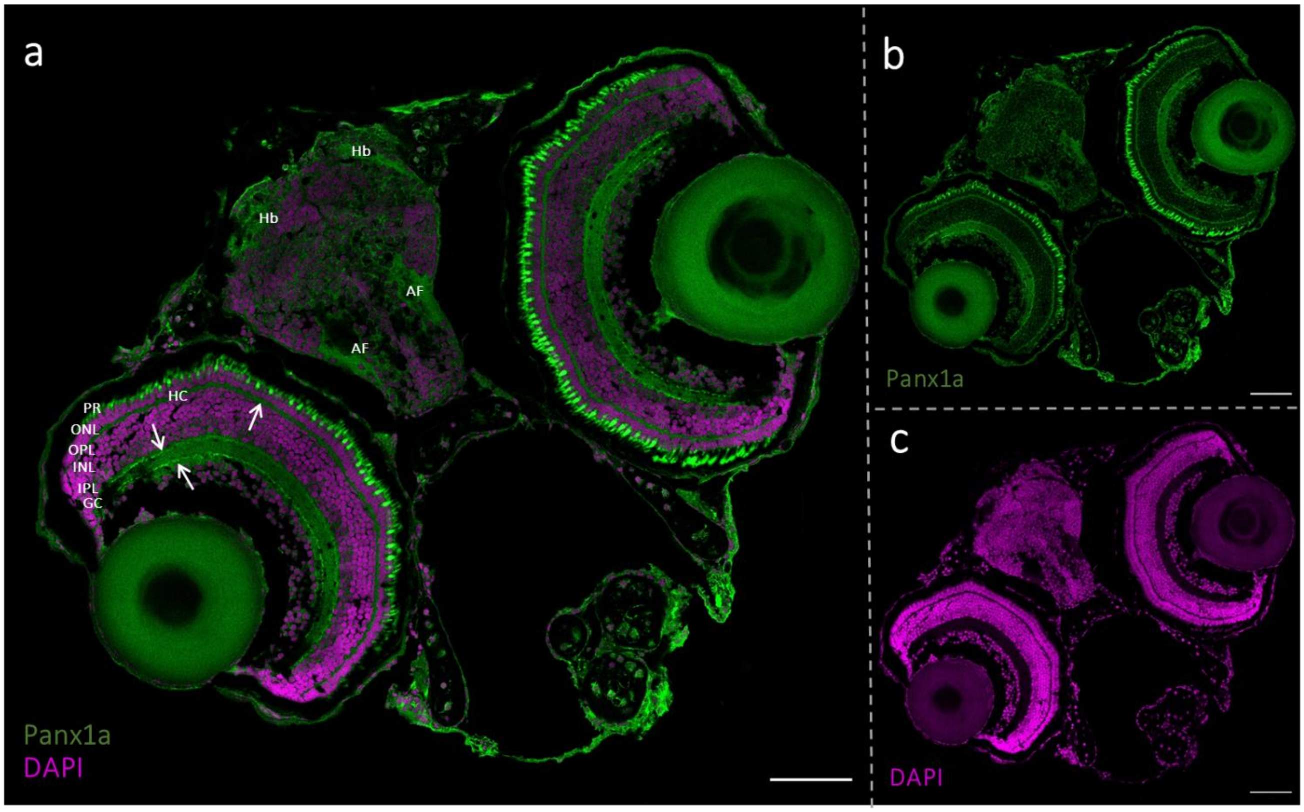

Figure 20. Expression and localization of the polyclonal rabbit Panx1a antibody in the brain and retina. a) The Panx1a protein (in green) is localized in the horizontal cell (HC) layers, as well as the ON and OFF ganglion cell (GC) layers demonstrated with an arrow. DAPI (in Magenta) is used to stain the nuclei. 6 slice z-stack at 20X magnification was acquired using the Leica Stellaris microscope. Scale = 50µm. b) The Panx1a antibody staining, Scale = 50µm. c) illustrates the DAPI staining, Scale = 50µm.

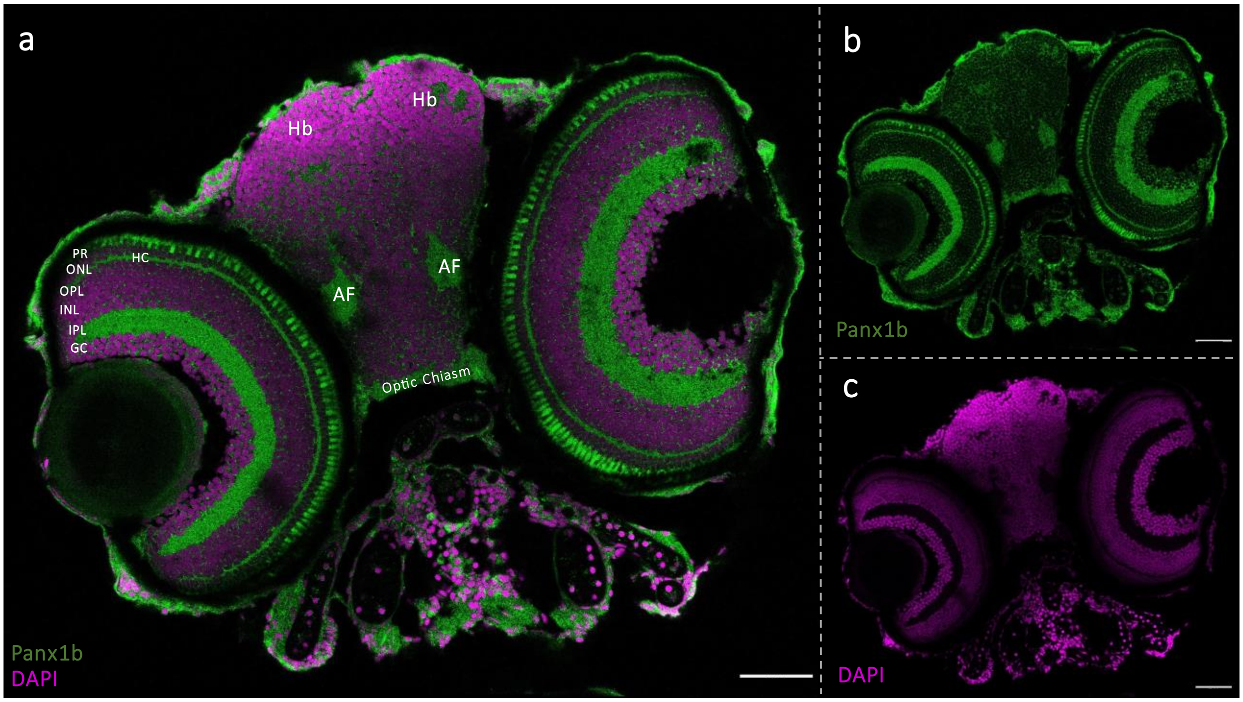

Figure 11. Expression and localization of the polyclonal rabbit Panx1b antibody in the brain and retina. a) The Panx1b protein (in green) is localized in the horizontal cell (HC) layers, the ganglion cell (GC) layers, as well as at the end feet of the muller glia astrocytes. The Panx1b protein is also expressed in the optic chiasm, arborization fields (AF), as well as the habenula (Hb). DAPI (in Magenta) is used to stain the nuclei. 6 slice z-stack at 20X magnification was acquired using the Leica Stellaris microscope. Scale = 50µm. b) The Panx1b antibody staining, Scale = 50µm. c) illustrates the DAPI staining, Scale = 50µm.

From previous work done by Safarian and colleagues (2021), the Panx1b polyclonal rabbit antibody overlapped with the monoclonal mouse GFAP antibody staining the end feet of the muller glia astrocytes in the retina. This project further explored the expression of Panx1b in the brain to see whether Panx1b is also found in the astrocytes and neurons in the brain. The monoclonal mouse zn-12 antibody stains the amacrine cells, inner nuclear layer, inner plexiform layer, ganglion cells, as well as neurons. The monoclonal mouse zn-8 antibody stains the ganglion cells, ganglion cell axons, and neuronal cell surface markers. Since, both antibodies are monoclonal mouse, a double staining can be done with the polyclonal rabbit panx1b antibody. The double staining of Panx1b and zn-12 (**Fig.12a, b, c**), followed by an intensity plot (**Fig.11g**) demonstrates the regional overlap of the Panx1b antibody with zn-12, suggesting the potential localization of the Panx1b protein in neurons. To quantify the colocalization of the two fluorescent signals (Panx1b and zn-12), the Manders Colocalization Coefficient analysis was conducted using ImageJ. The analysis demonstrated a substantial proportion of the signal from the first fluorescent channel did overlap with the signal from the second channel (M1= 0.85), and similarly there was overlap between the green fluorescence channel with the red channel (M2= 0.94). The double staining of Paxn1b and zn-8 (**Fig.12d, e, f**), followed by an intensity plot (**Fig.11 h**) also demonstrates the regional overlap of the Panx1b antibody with zn-8 depicted by the trend seen in the intensity plot with the peaks, suggesting the potential localization of the Panx1b protein in the neuronal cell surface in the brain. The intensity plots were measured using the ImageJ software for fluorescent detection and analysis. After conducting the Manders colocalization coefficient for the two proteins (Panx1b and zn-8), the analysis showed a substantial proportion of the signal from the first fluorescent channel did overlap with the signal from the second channel (M1= 0.88), and similarly, there was overlap between the green fluorescence channel with the red channel (M2= 0.99). The expression and co-localization of the polyclonal rabbit Panx1b antibody with the monoclonal mouse GFAP antibody was also tested followed by an intensity plot analysis to detect the intensity of the fluorescent signal (**Fig.13**). The double staining of Panx1b (in green) combined with GFAP (in magenta) (**Fig.13a, b, c**) with the arrow pointing towards the habenula region. The habenula region contains a high concentration of astrocytes (Cui et al., 2018) and the GFAP stains the astrocytes in this region. The intensity plot analysis (**Fig 13d, e**) using the ImageJ software, illustrates the intensity of the fluorescent signal for both antibodies, and the regional intensity overlap can be observed by the trends of the peaks. After conducting a Manders colocalization coefficient analysis to quantify the colocalization of Panx1b and GFAP in the brain, the analysis demonstrated a substantial proportion of the signal from the first fluorescent channel did overlap with the signal from the second channel (M1= 0.88), and similarly, there was overlap between the green fluorescence channel with the red channel (M2= 0.98).

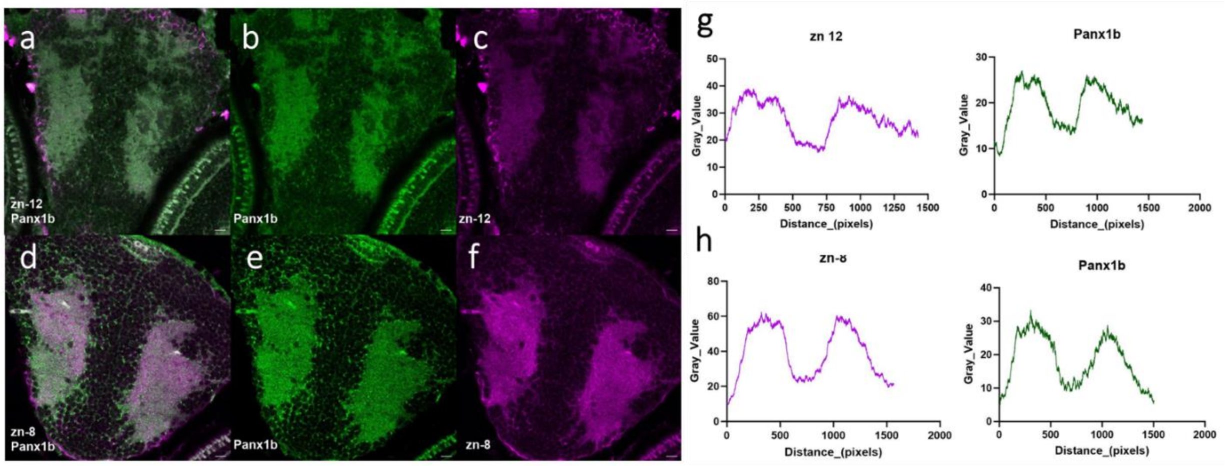

Figure 12. The expression and co-localization of the polyclonal rabbit Panx1b antibody with monoclonal mouse zn-12 and monoclonal mouse zn-8 respectively. **a)** Illustrated the zn-12 (in magenta) and Panx1b (in green) double staining using the 6dpf TL brain, 15µm slice at 63x magnification, Scale =10 µm. **b)** Panx1b staining (in green), 15µm slice at 63x magnification, Scale =10 µm. **c)** Staining of the zn-12 antibody (in magenta), 15µm slice at 63x magnification, Scale =10 µm. **d)** Illustrated the zn-8 (in magenta) and Panx1b (in green) double staining using the 6dpf TL brain, 15µm slice at 63x magnification, Scale =10 µm. **e)** Panx1b staining (in green), 15µm slice at 63x magnification, Scale =10 µm. **f)** staining of the zn-8 antibody (in magenta), 15µm slice at 63x magnification, Scale =10 µm. **g)** Intensity plot of zn-12 (in magenta) and Panx1b (in green) of the entire brain region slice to measure the potential colocalization of the two antibodies. **h)** Intensity plot of zn-12 (in magenta) and Panx1b (in green) of the entire brain region slice to measure the potential colocalization of the two antibodies.

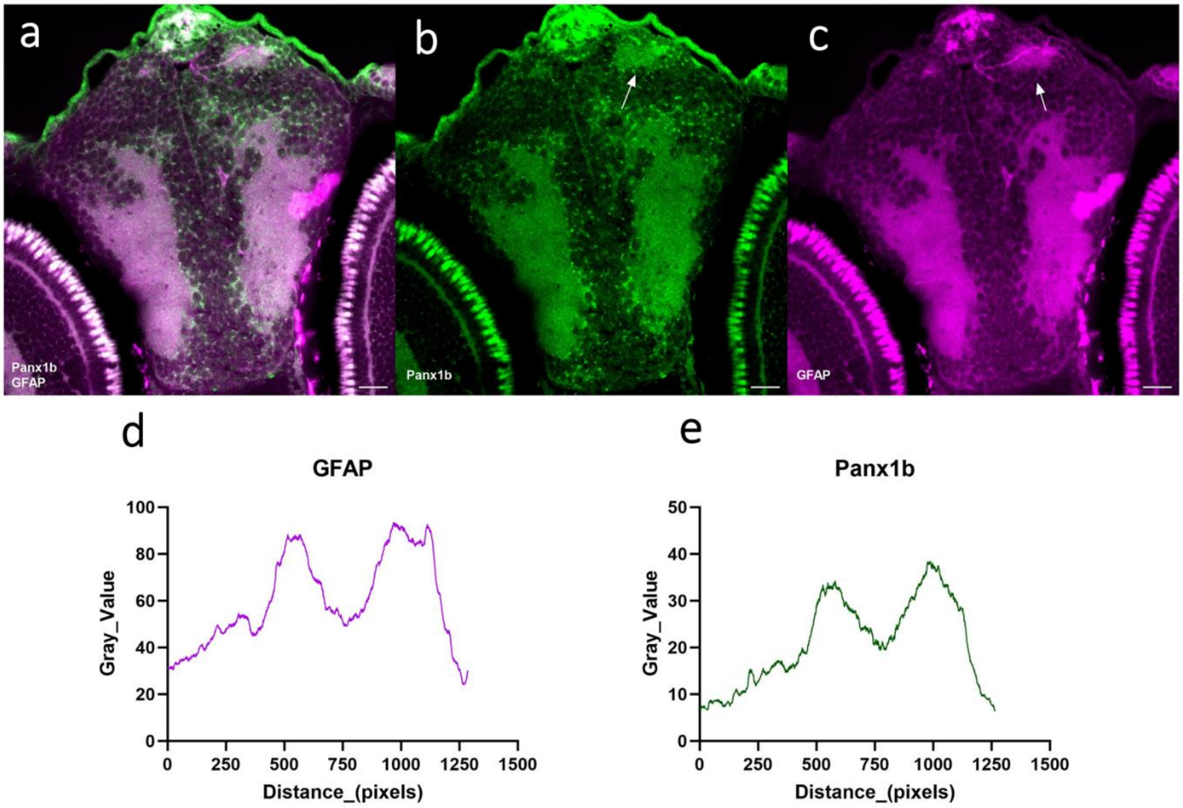

Figure 13. The expression and co-localization of the polyclonal rabbit Panx1b antibody with monoclonal mouse GFAP antibody **a)** GFAP (in magenta) and Panx1b (in green) double staining using the 6dpf TL brain, 15µm slice at 63x magnification, Scale =12 µm. **b)** Panx1b staining (in green), 15µm slice at 63x magnification, Scale =12 µm. **c)** staining of the GFAP antibody (in magenta), 15µm slice at 63x magnification, Scale =12 µm. **d)** The intensity plot of GFAP of the brain region with the peaks illustrating the highest intensity of the antibody. **e)** The intensity plot of Panx1b expression in the brain with the peaks showing the highest intensity of the protein.

The monoclonal mouse acetylated tubulin antibody is commonly used to stain the axonal track and since the habenula has a dense concentration of these axonal tract, the acetylated tubulin antibody can also be used as a habenula marker. The double staining of the polyclonal rabbit Panx1b antibody (in green) with the monoclonal mouse acetylated tubulin antibody (in magenta) illustrates the expression and co-localization of the two antibodies in the habenula region (**Fig. 14a, b, c**). The intensity plot analysis of the selected rectangular region (**Fig. 14b, c**) was processed using ImageJ software that detects the intensity of the fluorescent signals (**Fig. 14d, e**), and the overlapping peak between the two plots shows the highest intensity of the fluorescence signal, suggesting that Panx1b is also expressed in the habenula region. A Manders colocalization coefficient was also used to quantify the colocalization of Panx1b and acetylated tubulin. The analysis demonstrated a substantial proportion of the signal from the first fluorescent channel did completely overlap with the signal from the second channel (M1= 1), and similarly, there was overlap between the green fluorescence channel with the red channel (M2= 0.82). Likewise, the double staining (**Fig. 15a, b, c**) of the polyclonal rabbit Panx1a (in green) with the monoclonal mouse acetylated tubulin (in magenta) also suggests an intensity overlapped that Panx1a is also expressed in the habenula region when the trends of the intensity plots are observed (**Fig. 15d, e**). A Manders colocalization coefficient analysis was used to quantify the colocalization of Panx1a and acetylated tubulin, the analysis showed a substantial proportion of the signal from the first fluorescent channel did completely overlap with the signal from the second channel (M1= 1), and similarly, there was overlap between the green fluorescence channel with the red channel (M2= 0.87).

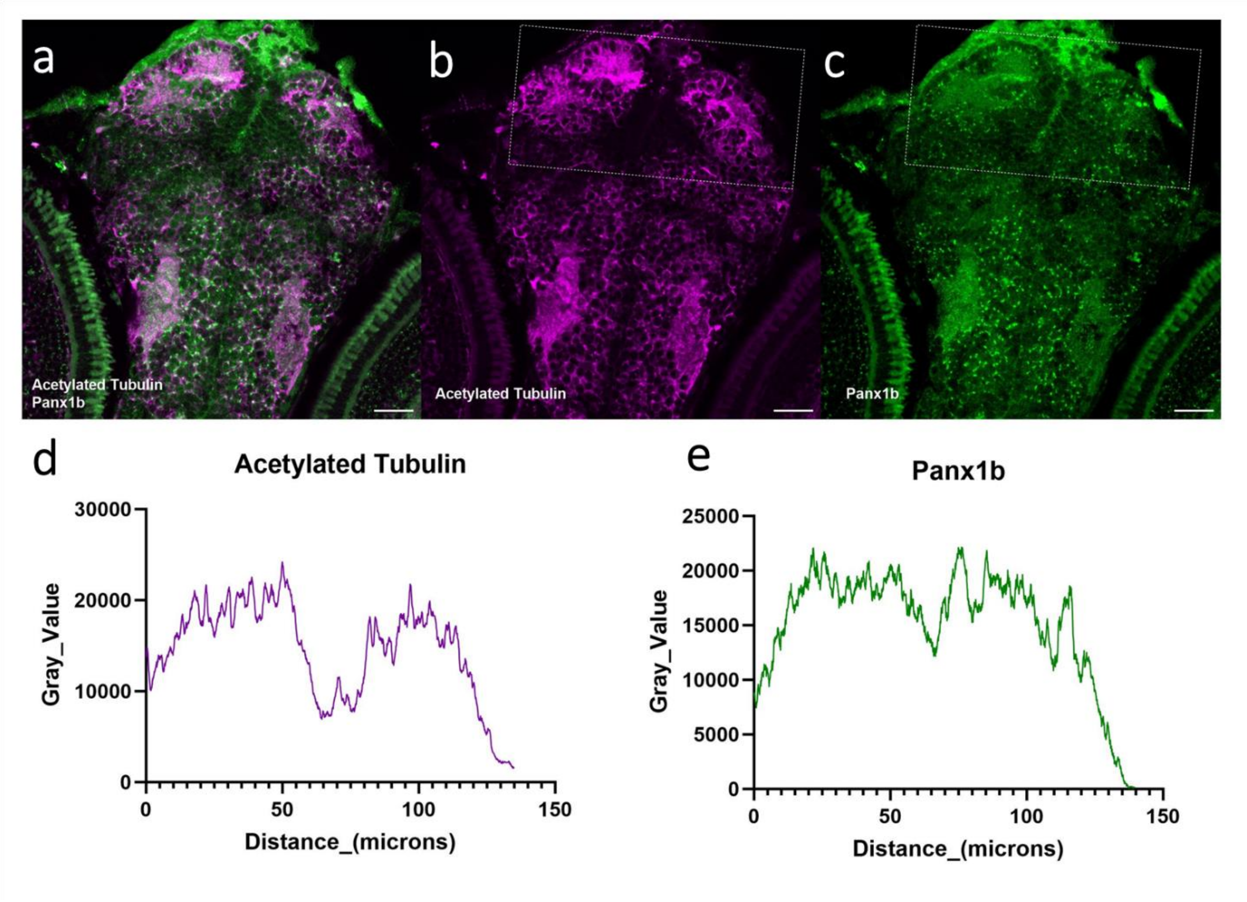

Figure 14. The expression and co-localization of the polyclonal rabbit Panx1b antibody with monoclonal mouse acetylated tubulin antibody **a)** acetylated tubulin (in magenta) and Panx1b (in green) double staining using the 6dpf TL brain, 15µm slice at 63x magnification, Scale =20 µm. **b)** Panx1b staining (in green), 15µm slice at 63x magnification, Scale =20 µm. **c)** staining of the acetylated tubulin antibody (in magenta), 15µm slice at 63x magnification, Scale =20 µm. **d)** The intensity plot of acetylated tubulin of the habenula region with the peaks illustrating the highest intensity of the antibody. **e)** The intensity plot of Panx1b expression in the habenula region with the peaks showing the highest intensity of the protein.

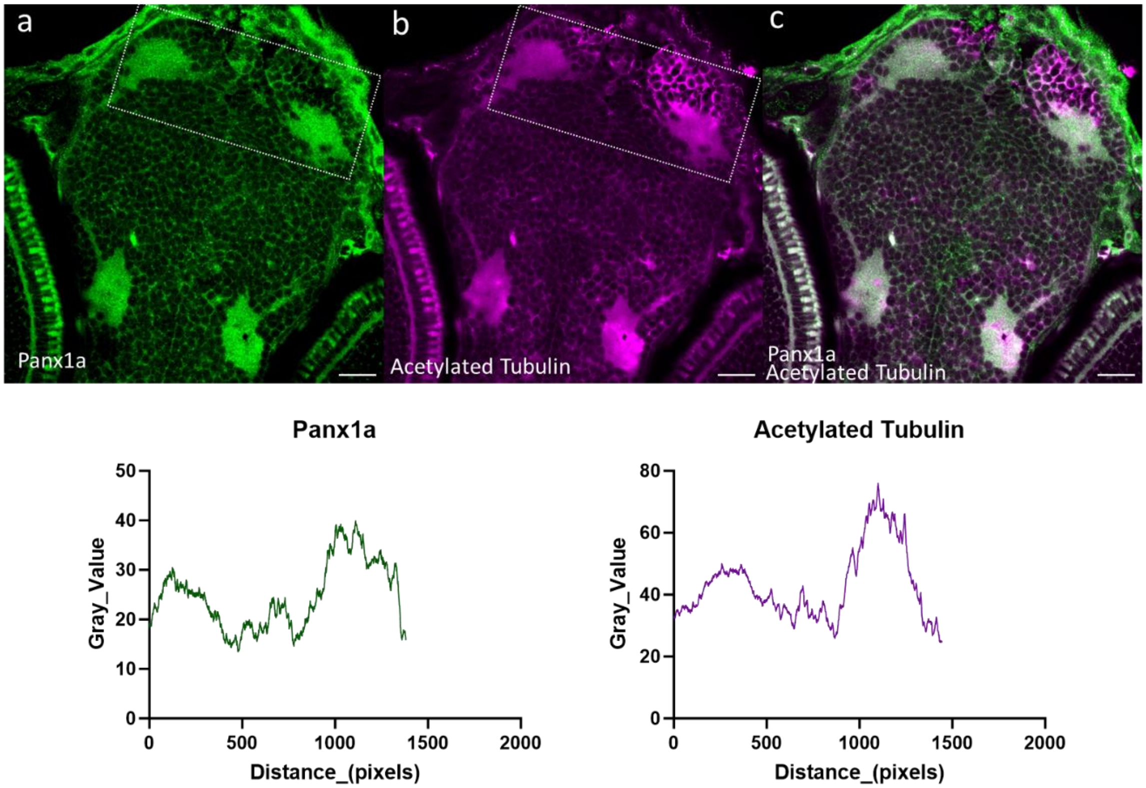

Figure 15. The expression and co-localization of the polyclonal rabbit Panx1a antibody with monoclonal mouse acetylated tubulin antibody **a)** Acetylated tubulin (in magenta) and Panx1a (in green) double staining using the 6dpf TL brain, 15µm slice at 63x magnification, Scale =20 µm. **b)** Panx1a staining (in green) capturing the habenula region (rectangular box), 15µm slice at 63x magnification, Scale =20 µm. **c)** Staining of the acetylated tubulin antibody (in magenta), 15µm slice at 63x magnification, Scale =20 µm. **d)** The intensity plot of acetylated tubulin of the habenula region with the peaks illustrating the highest intensity of the antibody. **e)** The intensity plot of Panx1a expression in the habenula region with the peaks showing the highest intensity of the protein.

5.2. The optomotor response (OMR) of the 6dfp larvae declines in the absence of functional Panx1a and Panx1b

The optomotor response (OMR) test was used to see how the fish responded to the exposed moving grating stimuli (**Fig.16**). For this test, the fish was exposed to three different spatial frequencies (64, 128, 256) measured in pixels/cycle, two different speeds (72, 144) measured in pixels/seconds, low contrast (10%) and high contrast (100%), as well as the leftward and rightward moving grating for 30 seconds at 70fps. For each of the conditions, a sample size of 12 for each genotype and each condition was tested. For the statistical analysis, the significance was calculated using a non-parametric one-way ANOVA (Kruskal- Wallis) test for the two treatments (Panx1a$^{-/-}$, Panx1b$^{-/-}$) compared to the control condition (TL). For most conditions, both Panx1a$^{-/-}$ and Panx1b$^{-/-}$ exhibited problems with left and right decision-making with spatial frequencies 64 and 128, which are narrower bands compared to 256 (n=12 for each independent condition). For representing the significance of the findings based on the statistical test conducted, (ns) is indicative of the findings being non-significant, a P-value less than 0.05 is indicated with (*), a P-value less than 0.01 is represented by (**), a P-value less than 0.001 is (***), and a P-value less than 0.0001 represents a significance by (****).

Both **Table 3** and **Table 4** summarize the significance (using the P-value) of the larvae OMR response using the Krustal-Wallis test of the two treatments compared to the control. When larvae were exposed to leftward and rightward moving grating, spatial frequency 64, speed 144, and contrast 10 Panx1a$^{-/-}$ had a significant decline in OMR response, same for Panx1b$^{-/-}$. The Panx1a$^{-/-}$ group also showed a significant OMR decline when exposed to leftward moving grating at contrast 10, spatial frequency 256, speed 72, as well as at contrast 100, spatial frequency 128, speed 72 for both leftward and rightward moving grating. Lastly, the Panx1a$^{-/-}$ fishline also showed a significant decline in their OMR response when exposed to leftward moving grating at spatial frequency 128, contrast 100, and speed 144. The Panx1b$^{-/-}$ also showed a significant decline in their OMR response when exposed to different left and right moving grating conditions. There was a significant decline in OMR response when the larvae were exposed to a contrast of 10, spatial frequency of 128, and the leftward moving grating at speed 72, as well as the leftward and rightward moving grating at speed 144. A significant decline was also observed when the larvae were exposed to rightward moving grating at contrast 10, spatial frequency 64, and speed 144, as well as leftward moving grating at contrast 10, spatial frequency 256, and speed 72. The larvae also struggled with the rightward moving grating at contrast 10, spatial frequency 256, and speed 144. When the trends for contrast 100% were observed, Panx1b$^{-/-}$ exhibited a significant decline in OMR response when exposed to leftward and rightward moving grating at speed 144 and spatial frequency 64. Lastly, Panx1b$^{-/-}$ showed a decrease in response towards the leftward moving grating at speed 72 and spatial frequency 128, as well as the leftward moving grating at speed 144 and spatial frequency 128.

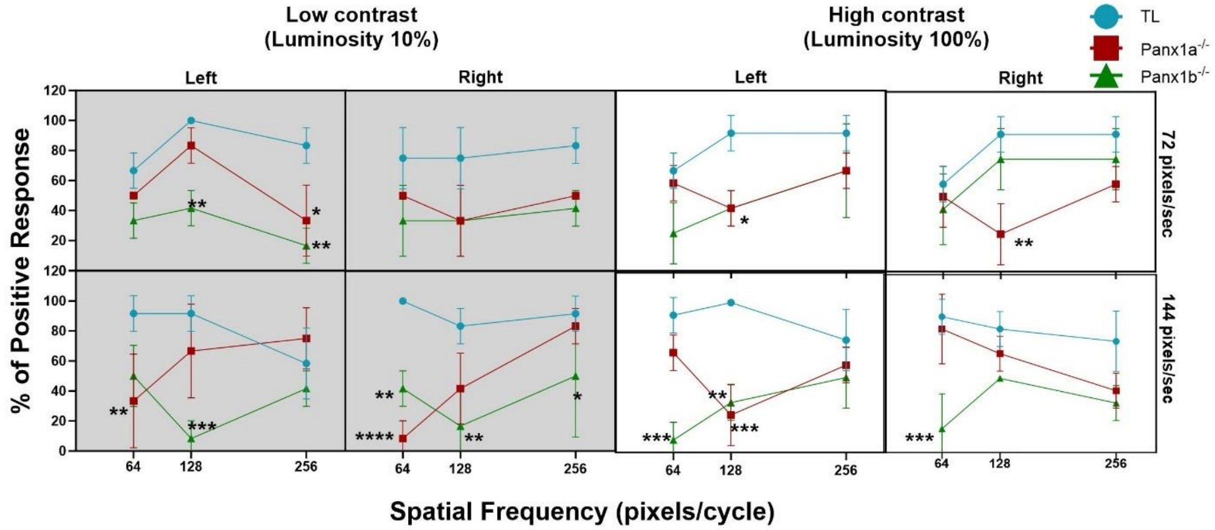

Figure 16. The optomotor response of the 6dpf larvae declines in the absence of functional Panx1a and Panx1b. The percentage of positive response represents the average number of larvae that responded to the setting of the moving grating stimuli. Both Panx1a$^{-/-}$ (in red) and Panx1b$^{-/-}$ (in green) showed a lower visual acuity when at low contrast compared to TL (in blue). The difference in their percentage response was also significant when the spatial frequency stimuli were set to 64 and 128 pixels/cycle, which are narrower moving grating bands (n=12). A Kruskal-Wallis (one control = TL, two treatments = Panx1a$^{-/-}$, Panx1b$^{-/-}$) followed by a Dunn's test. Significance '*' Alpha < 0.05. Error bars = SEM.

Table 3. Multiple comparison of the OMR response of TL (control) compared to Panx1a$^{-/-}$ (treatment) larvae.

Contrast Levels		**Low (10%)**			**High (100%)**		
Speed (pixels/s)	Direction	Spatial Frequencies (pixels/cycles)					
		64	128	256	64	128	256
72	Leftward	0.84	0.71	0.0302*	>0.99	0.02*	0.33
	Rightward	0.45	0.09	0.21	>0.99	0.0019**	0.13
144	Leftward	0.0085**	0.21	0.83	0.45	0.0006***	0.82
	Rightward	<0.0001****	0.089	>0.99	0.69	0.78	0.45

Table 4. Multiple comparison of the OMR response of TL (control) compared to Panx1b$^{-/-}$ (treatment) larvae.

Contrast Levels		**Low (10%)**			**High (100%)**		
Speed (pixels/s)	Direction	Spatial Frequencies (pixels/cycles)					
		64	128	256	64	128	256
72	Leftward	0.21	0.0023**	0.0024**	0.088	0.02*	0.33
	Rightward	0.087	0.088	0.083	0.84	0.43	0.71
144	Leftward	0.08	0.0001***	0.83	0.0001***	0.0025**	0.43
	Rightward	0.0097**	0.0025**	0.04*	0.0003***	0.17	0.08

5.3. The Optokinetic response (OKR) of the 6dfp larvae declines in the absence of functional Panx1a

The optokinetic response (OKR) test was used to test the function of the retinal ganglion cells by investigating the response of the larvae's saccadic eye movement to detect ocular motor deficiencies. The test was conducted using three different spatial frequencies (0.1, 0.15, 0.2) in cycle/degree, with 0.2 representing the narrowest band, at three different contrasts (20%, 50%, 100%), and exposed to the leftward and rightward moving grating. A constant speed of 0.01 degree/sec was used to evoke an OKR response. The amplitude of the saccadic eye movement represents the distance the eye has traveled between two fixation points showing that the eye gaze is closer to the target of interest (Paeve & Laurent, 2011). The spatial frequency is defined by the number of pairs of bars that capture the larvae's visual field (Chen et al., 2016). In this study, a spatial frequency of 0.2 cycle/degree captures around 8 pairs of bars (black and white), 0.15 cycle/degree is about 5 pairs of black and white bars (because the width of the bar is wider than 0.2), and 0.1 which contains the widest width contains about 3 pairs of bars. Contrast is defined by a difference in luminance and is the intensity of light that is projected onto the visual field (Chen et al., 2016). For measuring the significance of the percentage of positive response, a nonparametric one-way ANOVA (Kruskal-Wallis) test was conducted followed by a Dunn's test. For representing the significance of the findings based on the statistical test conducted, (ns) is indicative of the findings being non-significant, a P-value less than 0.05 is indicated with (*), a P-value less than 0.01 is represented by (**), a P-value less than 0.001 is (***), and a P-value less than 0.0001 represents a significance by (****). For each independent condition, n=12 larvae were used for each genotype.

The percentage of positive response at spatial frequency 0.2 (**Fig.17**) demonstrated that the Panx1b$^{-/-}$ fishline responded similarly to TL and no significance was observed when compared. The Panx1a$^{-/-}$ exhibited a lower OKR response compared to TL when the moving grating was towards the rightward motion for all conditions (20%, 50%, 100%) were significant, with P-values 0.04, 0.03, and 0.0014 respectively. When exposed to leftward moving grating at 100%, Panx1a$^{-/-}$ also showed a decline in their OKR response (P-value = 0.014).

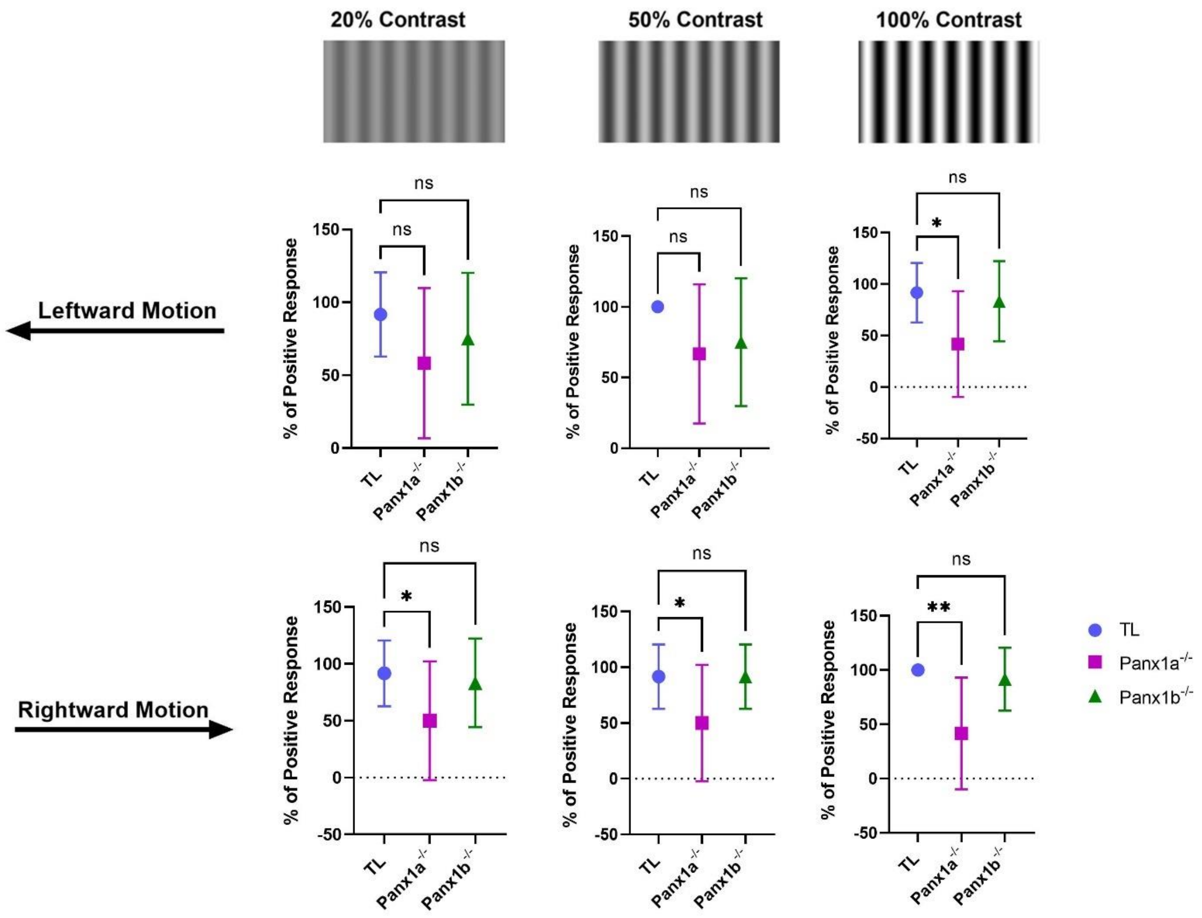

Figure 17. The optokinetic response (OKR) of the 6dpf larvae declines in the absence of functional Panx1a. The % of positive response represents the average number of the 6dpf larvae that responded to leftward and rightward moving grating at three different contrasts (20%, 50%, 100%), spatial frequency 0.2cycle/degree, and speed 0.01 degree/sec (n=12 for each). The top graph represents the response to the leftward-moving grating and bottom graph shows the response of the rightward moving grating. Both Panx1a$^{-/-}$ (in magenta) and Panx1b$^{-/-}$ (in green) were compared to TL (in blue) using a Kruskal-Wallis test followed by a Dunn's test to determine the significance '*' Alpha < 0.05. Error bars = SEM.

The percentage of positive response at spatial frequency 0.15 (**Fig.18**) demonstrated that the Panx1b$^{-/-}$ fishline responded similarly to TL and no significant trends were observed. The response of the Panx1a$^{-/-}$ fishline declined in all conditions except when exposed to the leftward moving grating at 100% contrast. When Panx1a$^{-/-}$ was exposed to the rightward moving grating at 20% contrast (P-value = 0.0175), at 50% contrast (P-value = 0.0493), and at 100% contrast (P-value = 0.0023) showed a significant response. Likewise, the Panx1a$^{-/-}$ exhibited a lower OMR response when exposed to the leftward moving grating at 20% contrast (P-value = 0.022) and 50% contrast (P-value = 0.0016).

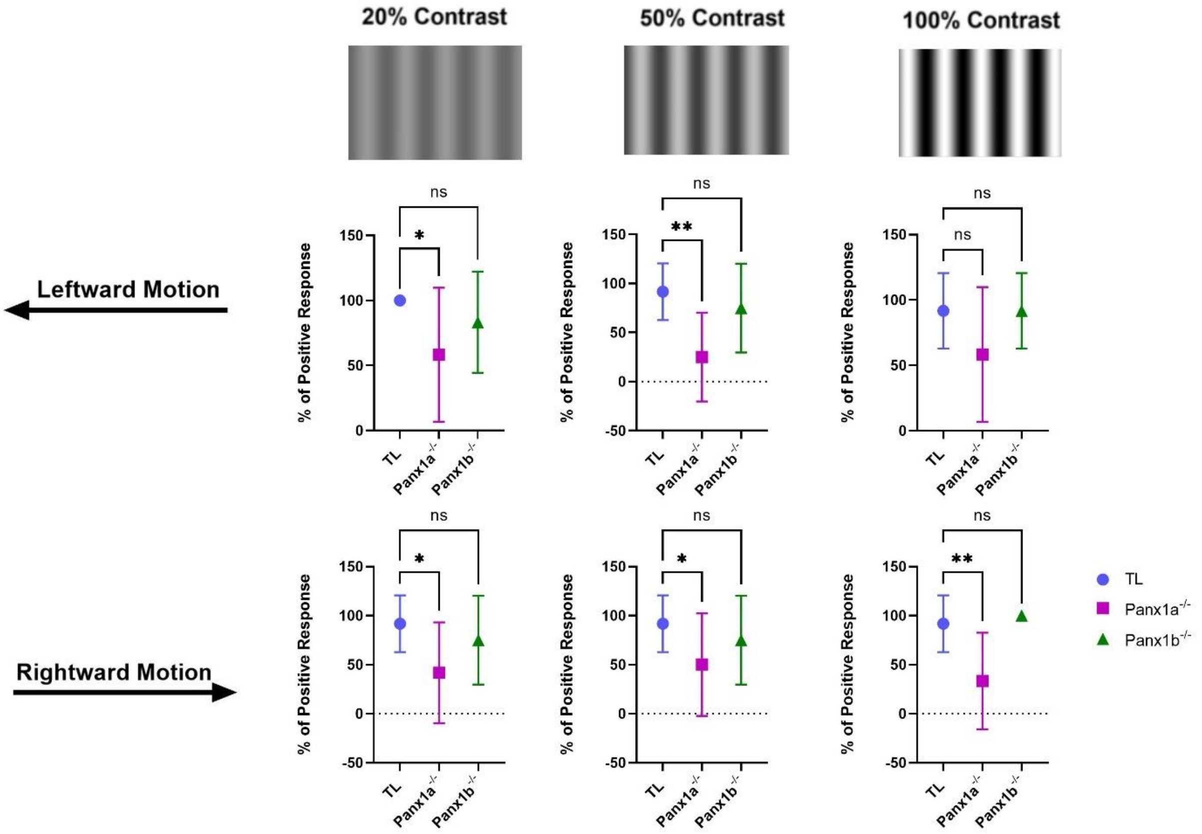

Figure 18. The optokinetic response (OKR) of the 6dpf larvae declines in the absence of functional Panx1a. The % of positive response represents the average number of the 6dpf larvae that responded to leftward and rightward moving grating at three different contrasts (20%, 50%, 100%), spatial frequency 0.15cycle/degree, and speed 0.01 degree/sec (n=12 for each). The top graph represents the response to the leftward-moving grating and bottom graph shows the response of the rightward moving grating. Both Panx1a$^{-/-}$ (in magenta) and Panx1b$^{-/-}$ (in green) were compared to TL (in blue) using a Kruskal-Wallis test followed by a Dunn’s test to determine the significance ‘*’ Alpha < 0.05. Error bars = SEM.

The percentage of positive response at spatial frequency 0.1 (**Fig. 19**) illustrated that the Panx1b$^{-/-}$ responded similarly to TL in all conditions. The Panx1a$^{-/-}$ showed a decrease in OMR response when exposed to the leftward moving grating at 50% contrast (P-value = 0.002). In addition, the Panx1a$^{-/-}$ also showed a decline in OMR response when exposed to the rightward moving grating at 20% contrast (P-value= 0.0056) and 50% contrast (P-value = 0.031).

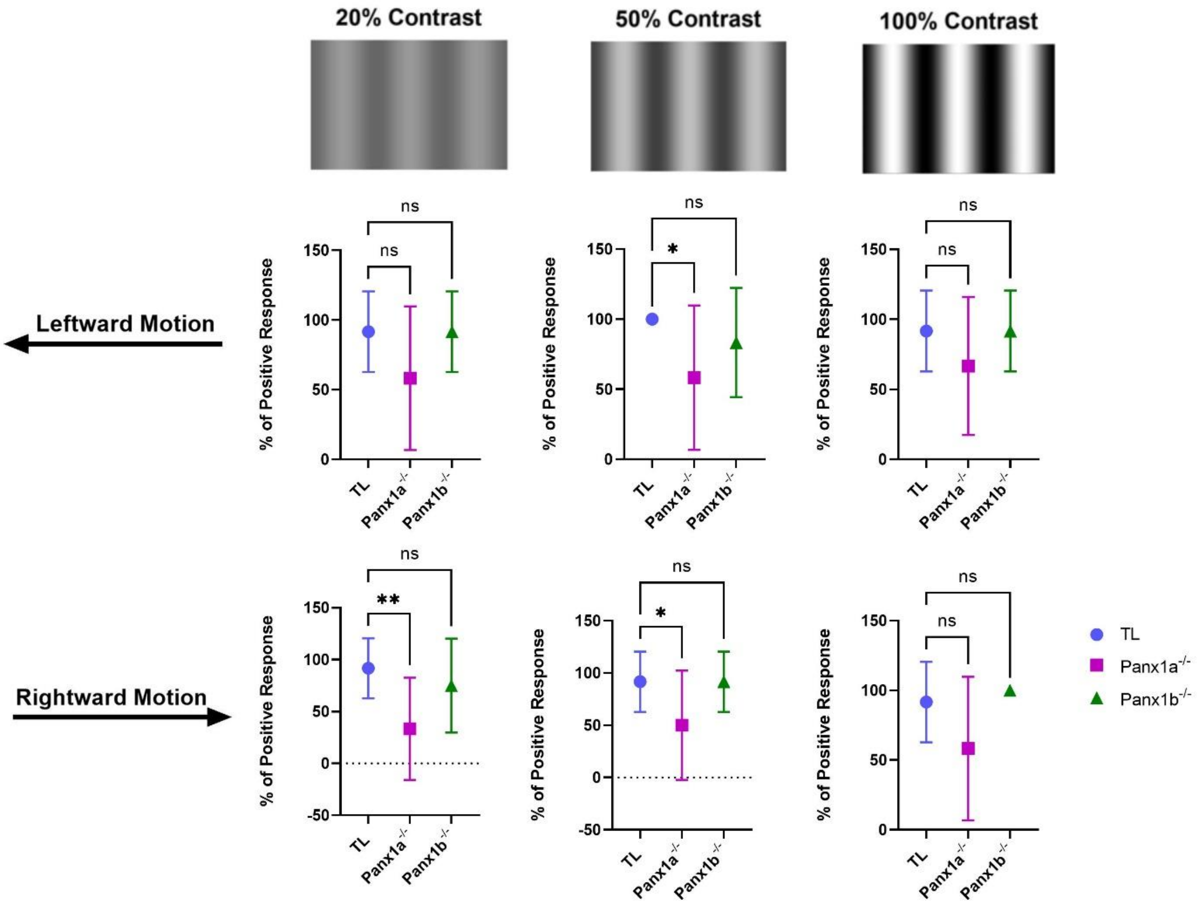

Figure 19. The optokinetic response (OKR) of the 6dpf larvae declines in the absence of functional Panx1a. The % of positive response represents the average number of the 6dpf larvae that responded to leftward and rightward moving grating at three different contrasts (20%, 50%, 100%), spatial frequency 0.1 cycle/degree, and speed 0.01 degree/sec (n=12 for each). The top graph represents the response to the leftward-moving grating and bottom graph shows the response of the rightward moving grating. Both Panx1a$^{-/-}$ (in magenta) and Panx1b$^{-/-}$ (in green) were compared to TL (in blue) using a Kruskal-Wallis test followed by a Dunn's test to determine the significance '*' Alpha < 0.05. Error bars = SEM.

5.4. The Optokinetic response (OKR) of the 6dfp larvae showed that Panx1a$^{-/-}$ is unable to generate functional saccades

The optokinetic response (OKR) test was used to test the function of the retinal ganglion cells by looking into the response of the larvae's saccadic eye movement to detect ocular motor deficiencies. The test was conducted using three different spatial frequencies (0.1, 0.15, 0.2) in cycle/degree, with 0.2 representing the narrowest band, at three different contrasts (20%, 50%, 100%), and exposed to the leftward and rightward moving grating. A constant speed of 0.01 degree/sec was used to evoke an OKR response. An example of the saccadic eye-movement pattern at spatial frequency 0.2 cycle/degree for the leftward and rightward moving grating has been demonstrated (**Fig. 20, Fig. 21 respectively**). At spatial frequency 0.2 cycle/degree which is considered the narrowest band exposed to the larvae, the 6dpf larvae can generate the highest number of saccades per minute and as the contrast setting is lowered to 20%, the larvae take more time to generate a single saccade. At 100% contrast, TL can generate around 13-14 saccades/min, Panx1b$^{-/-}$ can generate 11-12 saccades/min. At 50% contrast, the TL generates around 8-9 saccades, and Panx1b$^{-/-}$ also generates around 6-7 saccades per minute. Interestingly, when the larvae are exposed to 20% contrast, TL can generate 6-7 saccades per minute, and Panx1b$^{-/-}$ generates 11-12 saccades per minute. The majority of Panx1a$^{-/-}$ (**Fig. 17**) are unable to generate functional saccades when exposed to leftward and rightward moving gratings at different contrasts (**Fig. 20, Fig. 21 respectively**). NOTE: This is just an example of the saccade performance extracted from one larvae of each genotype, various patterns of saccades have been observed as there are individual differences among larvae and a sample size of 12 has been collected for each genotype for each condition.

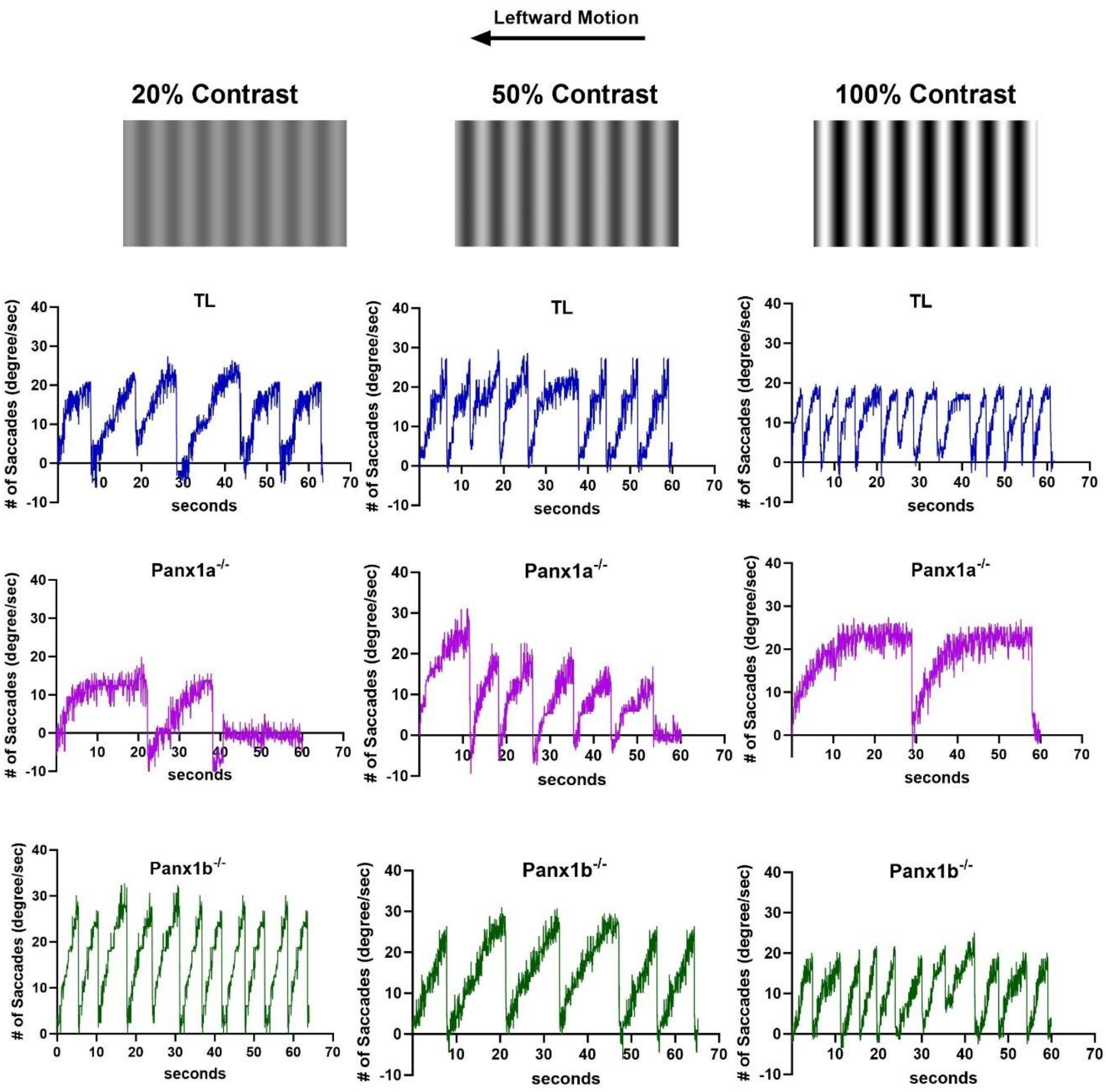

Figure 20. Demonstration of the optokinetic response (OKR) pattern at 0.2 spatial frequency. The saccadic eye-movement pattern of the 6dpf larvae exposed to the leftward moving grating at 20%, 50%, and 100% contrast. Panx1a$^{-/-}$ (in purple) OKR response declines at all contrasts. TL (in blue) and Panx1b$^{-/-}$ (in green) can generate around 12-13 and 11-12 saccades respectively at 100% contrast. As the contrast goes down the number of saccades for both TL and Panx1b$^{-/-}$ declines.

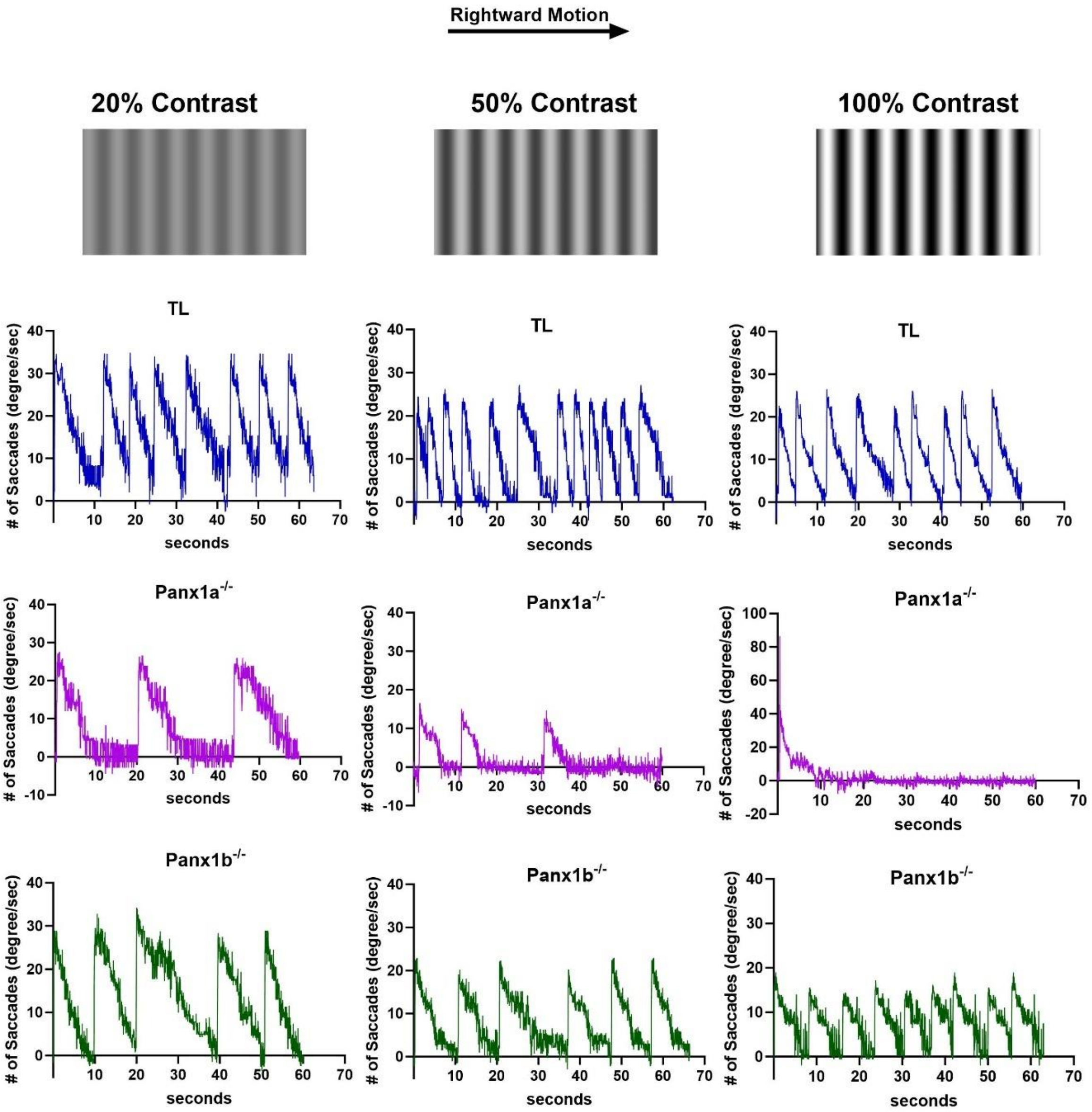

Figure 21. Demonstration of the optokinetic response (OKR) pattern at 0.2 spatial frequency. The saccadic eye-movement pattern of the 6dpf larvae exposed to the rightward moving grating at 20%, 50%, and 100% contrast. Panx1a$^{-/-}$ (in purple) OKR response declines at all contrasts. TL (in blue) and Panx1b$^{-/-}$ (in green) can generate around 9-10 and 9-10 saccades respectively at 100% contrast. As the contrast goes down the number of saccades for both TL and Panx1b$^{-/-}$ declines.

An example of the saccadic eye-movement pattern at spatial frequency 0.15 cycle/degree for the leftward and rightward moving grating has been demonstrated (**Fig. 22, Fig. 23 respectively**). At spatial frequency 0.15 cycle/degree which is considered the middle band (not too narrow and not too wide) exposed to the larvae, where at 100% contrast the larvae can generate the most saccades, and as the contrast setting is lowered to 20%, the larvae take more time to generate a single saccade. At 100% contrast, TL can generate around 8-9 saccades/min, Panx1b$^{-/-}$ can generate 6-7 saccades/min. At 50% contrast, the TL generates around 6-7 saccades, and Panx1b$^{-/-}$ also generates around 5-6 saccades per minute. When the larvae are exposed to 20% contrast, TL can generate 4-5 saccades per minute, and Panx1b$^{-/-}$ generates 4-5 saccades per minute. Most of Panx1a$^{-/-}$ (**Fig. 18**) cannot generate functional saccades when exposed to leftward and rightward moving gratings at different contrasts (**Fig. 22, and Fig. 23 respectively**). NOTE: This is just an example of the saccade performance extracted from one larvae of each genotype, various patterns of saccades have been observed as there are individual differences among larvae and a sample size of 12 has been collected for each genotype for each condition.

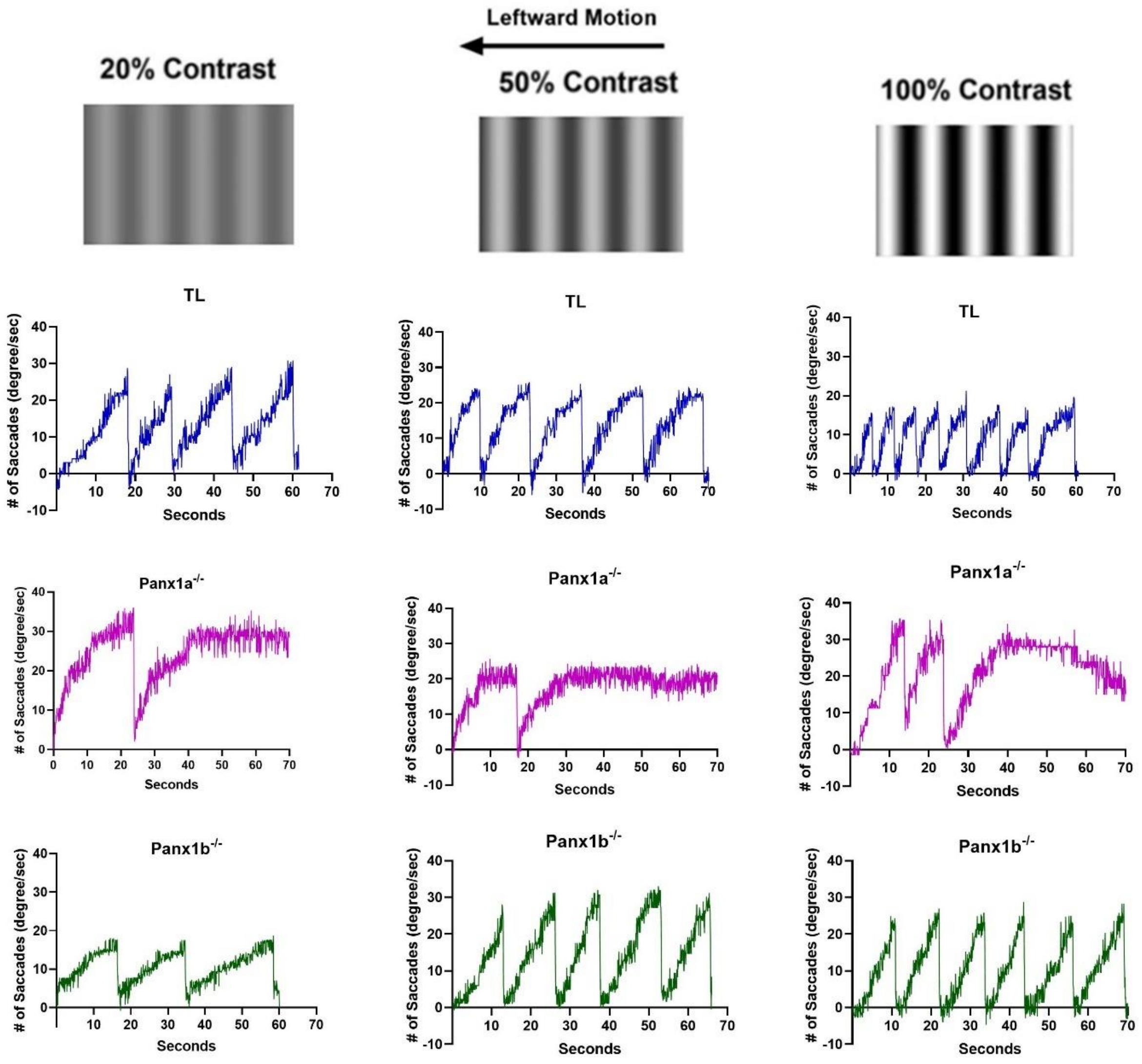

Figure 22. Demonstration of the optokinetic response (OKR) pattern at 0.15 spatial frequency. The saccadic eye-movement pattern of the 6dpf larvae exposed to the leftward moving grating at 20%, 50%, and 100% contrast. Panx1a$^{-/-}$ (in purple) OKR response declines at all contrasts. TL (in blue) and Panx1b$^{-/-}$ (in green) can generate around 12-13 and 11-12 saccades respectively at 100% contrast. As the contrast goes down the number of saccades for both TL and Panx1b$^{-/-}$ declines.

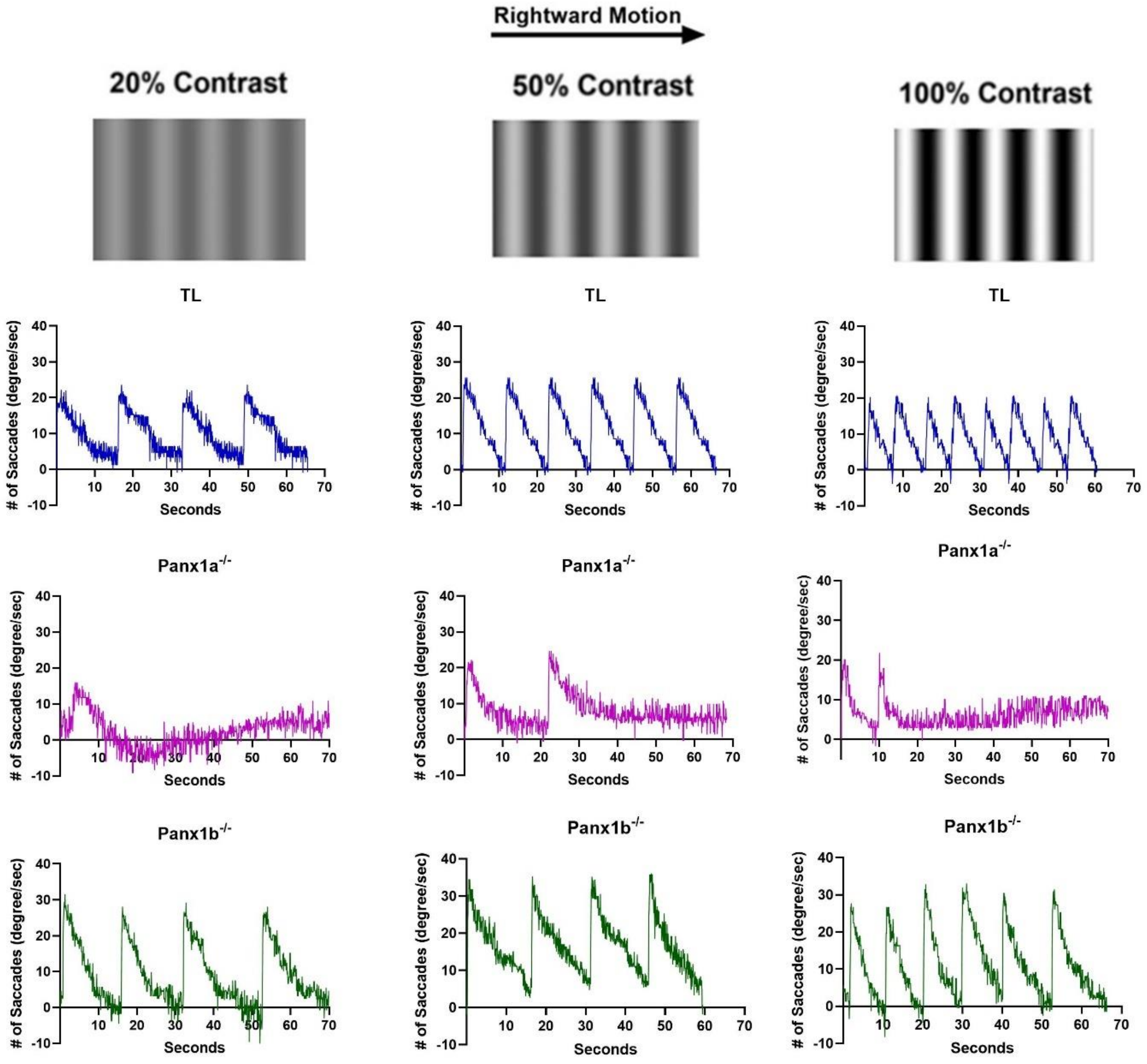

Figure 23. Demonstration of the optokinetic response (OKR) pattern at 0.15 spatial frequency. The saccadic eye-movement pattern of the 6dpf larvae exposed to the rightward moving grating at 20%, 50%, and 100% contrast. Panx1a$^{-/-}$ (in purple) OKR response declines at all contrasts. TL (in blue) and Panx1b$^{-/-}$ (in green) can generate around 9-10 and 9-10 saccades respectively at 100% contrast. As the contrast goes down the number of saccades for both TL and Panx1b$^{-/-}$ declines.

An example of the saccadic eye-movement pattern at spatial frequency 0.1 cycle/degree for the leftward and rightward moving grating has been demonstrated (**Fig. 24, Fig. 25 respectively**). At spatial frequency 0.1 cycle/degree which is the widest band among 0.2 and 0.15 spatial frequencies. The larvae can generate the most saccades at 100% contrast and as the contrast setting is lowered to 20%, the larvae take more time to generate a single saccade. At 100% contrast, TL can generate around 5-6 saccades/min, Panx1b$^{-/-}$ can generate 5-6 saccades/min. At 50% contrast, the TL generates around 5-6 saccades, and Panx1b$^{-/-}$ also generates around 5-6 saccades per minute. When the larvae are exposed to 20% contrast, TL can generate 4-5 saccades per minute, and Panx1b$^{-/-}$ generates 4-5 saccades per minute. The majority of Panx1a$^{-/-}$ (**Fig. 19**) cannot generate functional saccades when exposed to leftward and rightward moving gratings at different contrasts (**Fig. 24, Fig. 25 respectively**). NOTE: This is just an example of the saccade performance extracted from one larvae of each genotype, various patterns of saccades have been observed as there are individual differences among larvae and a sample size of 12 has been collected for each genotype for each condition.

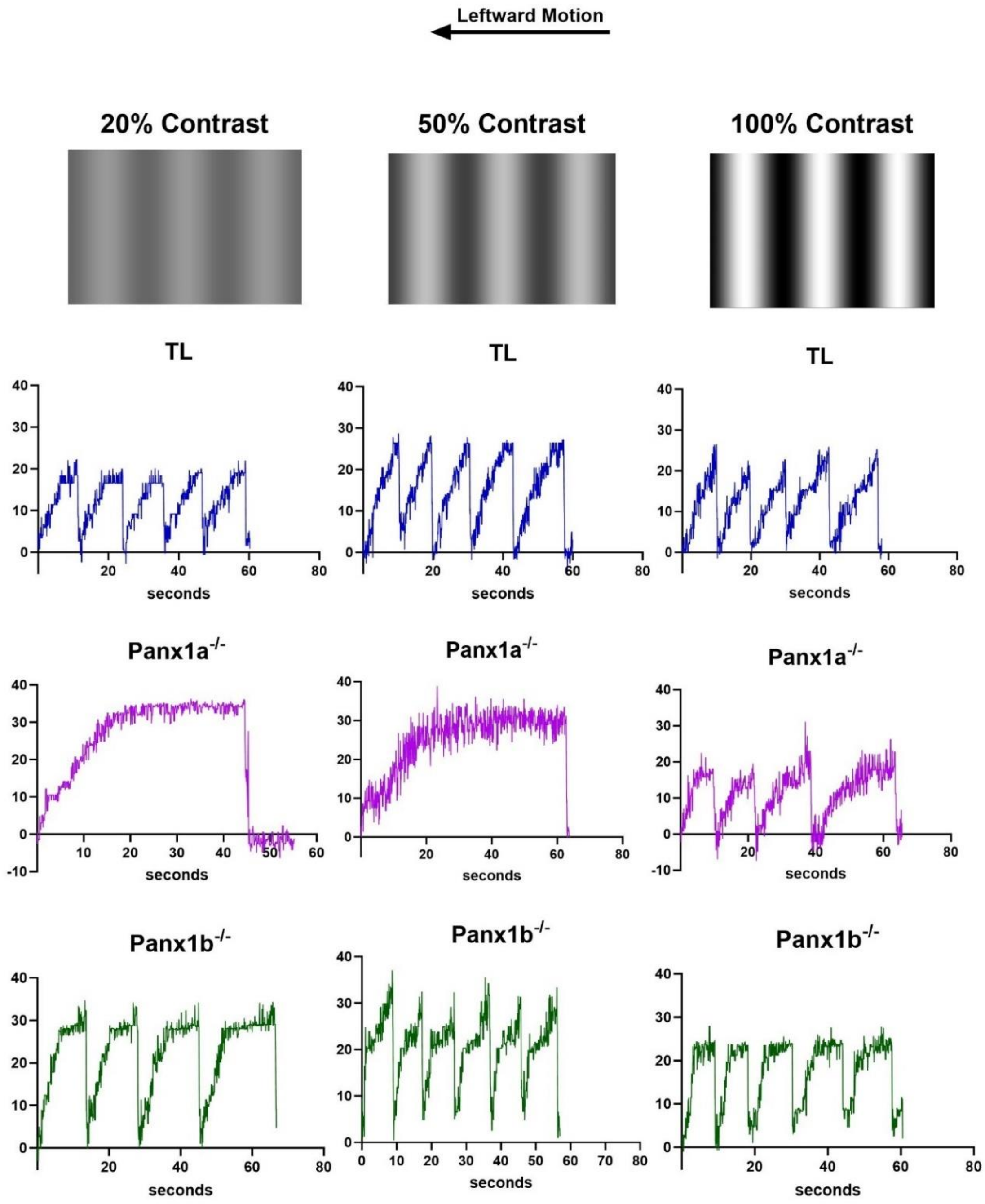

Figure 24. Demonstration of the optokinetic response (OKR) pattern at 0.1 spatial frequency. The saccadic eye-movement pattern of the 6dpf larvae exposed to the leftward moving grating at 20%, 50%, and 100% contrast. Panx1a$^{-/-}$ (in purple) OKR response declines at all contrasts. TL (in blue) and Panx1b$^{-/-}$ (in green) can generate around 4-5 at 100% contrast. As the contrast goes down the number of saccades for both TL and Panx1b$^{-/-}$ declines.

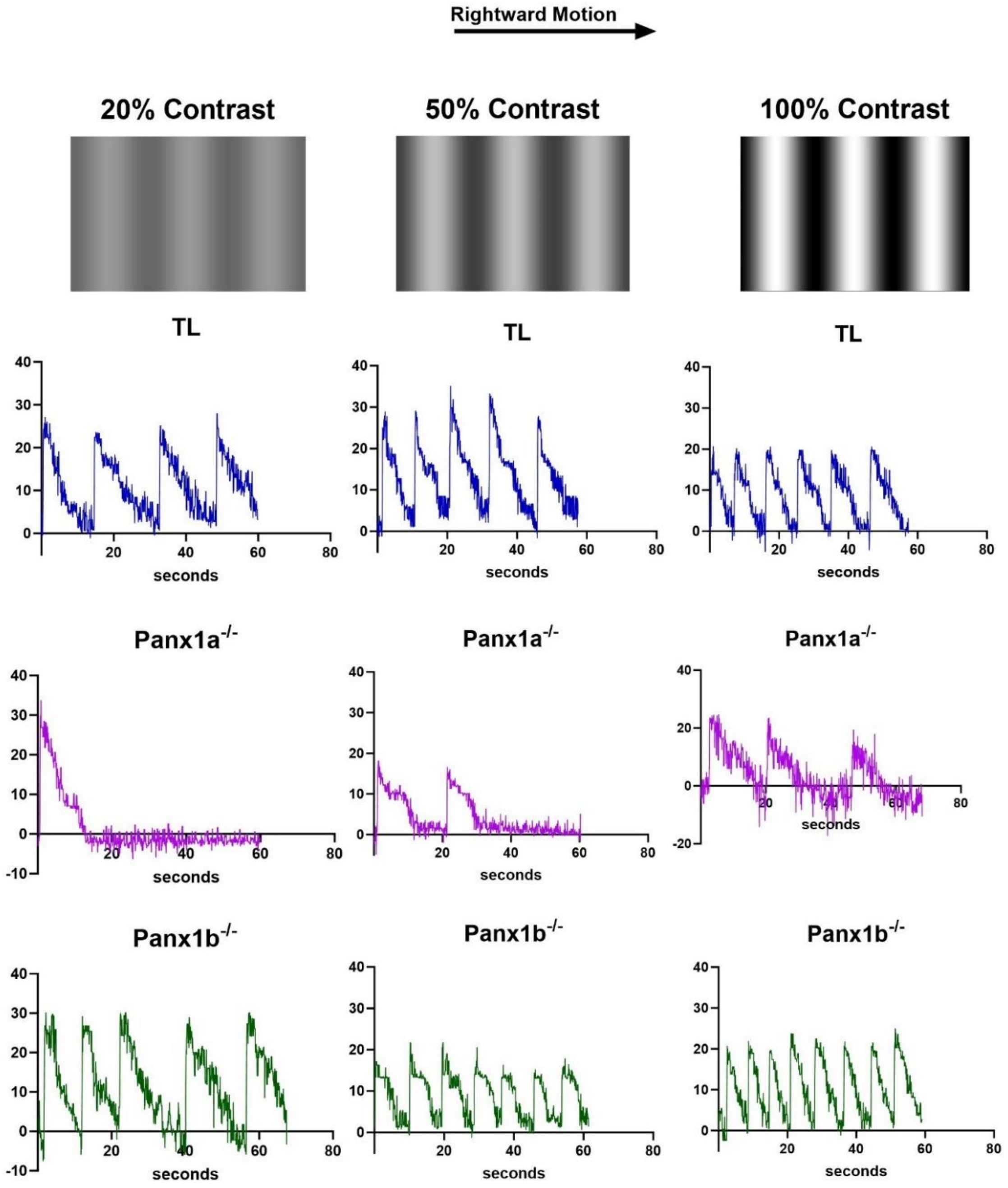

Figure 25. Demonstration of the optokinetic response (OKR) pattern at 0.1 spatial frequency. The saccadic eye-movement pattern of the 6dpf larvae exposed to the leftward moving grating at 20%, 50%, and 100% contrast. Panx1a$^{-/-}$ (in purple) OKR response declines at all contrasts. TL (in blue) and Panx1b$^{-/-}$ (in green) can generate around 5-6 and 7-8 saccades respectively at 100% contrast. As the contrast goes down the number of saccades for both TL and Panx1b$^{-/-}$ declines.

5.5. Loss of functional Panx1a and Panx1b alters OKR spatial frequency response

In this section, a detailed analysis of the OKR response pattern of the saccades has been conducted by measuring three different parameters: The tracking velocity (how long it takes for the larvae to generate a saccade or the pursuit phase), OKR amplitude (at what amplitude the larvae performs the fast phase or the rapid saccade), and delta peak of saccades (the frequency of the larvae generating the next saccades by averaging the distance between the peaks of two saccades) at three different spatial frequencies (0.2, 0.15, 0.1) exposing the larvae to the leftward and rightward moving grating. For the statistical analysis, a parametric one-way ANOVA followed by a Dunnett test has been conducted for the significance of the findings. For representing the significance of the findings based on the statistical test conducted, (ns) is indicative of the findings being non-significant, a P-value less than 0.05 is indicated with (*), a P-value less than 0.01 is represented by (**), a P-value less than 0.001 is (***), and a P-value less than 0.0001 represents a significance by (****). For each independent condition, n=12 larvae were used for each genotype.

Different patterns can be observed when the 6dpf larvae are exposed to different spatial frequencies. For the first condition, the larvae were exposed to the leftward moving grating at 0.2 cycles/degree (**Fig. 26**). This was the narrowest band threshold for the larvae to be able to generate saccades. The two knockout fishlines (Panx1a$^{-/-}$ and Panx1b$^{-/-}$) were individually compared to the wild-type (TL). After conducting the statistical analysis (one-way ANOVA followed by the Dunnett test), both Panx1a$^{-/-}$ and Panx1b$^{-/-}$ exhibit irregular patterns when generating saccades. At 20% contrast, the Panx1b$^{-/-}$ tracking velocity was significant (P-value = 0.0002) compared to TL, showing that at low contrast, the Panx1b$^{-/-}$ generates a greater number of saccades compared to TL. The OKR amplitude of the Panx1a$^{-/-}$ was significant (P-value is

<0.0001) compared to TL, exhibiting a shorter amplitude. When the larvae are exposed to 50% contrast, the tracking velocity for both Panx1a$^{-/-}$ and Panx1b$^{-/-}$ was significant (P-value < 0.0001 and P-value = 0.0435 respectively). The rate of the frequency of saccades for Panx1a$^{-/-}$ and Panx1b$^{-/-}$ were also significant (P-value = 0.001 and P-value = 0.034 respectively). Hence, Panx1a$^{-/-}$ fishline takes significantly longer to generate a saccade. Panx1b$^{-/-}$ takes longer than TL to generate a saccade and cascade of saccades. At 100% contrast, the tracking velocity, and the frequency rate of generating saccades of the Panx1a$^{-/-}$ were significant (P-value = 0.0051, P-value = 0.0006). The Panx1b$^{-/-}$ fishline demonstrated a significant (P-value = 0.0024) when measuring the tracking velocity where the 6dpf Panx1b$^{-/-}$ larvae generated longer saccades compared to TL. The OKR amplitude of Panx1b$^{-/-}$ was significant (P-value < 0.0001) at 100% contrast where the larvae generated bigger amplitudes compared to TL. The frequency rate of the saccades for Panx1b$^{-/-}$ was also significant (P-value = 0.0007) and two populations of Panx1b$^{-/-}$ are demonstrated (**Fig. 26**) where one responds similarly to TL and the other takes longer to generate subsequent saccades. The larvae were also exposed to the rightward moving grating at 0.2 cycles/degree. A constant speed of 0.01 degree/sec was used to evoke a saccadic response (**Fig. 27**). At 20% contrast, the Panx1a$^{-/-}$ fishline showed a significant difference in all three parameters, Tracking velocity (P-value <0.0001), OKR amplitude (P-value = 0.0187), and frequency of delta peak (P-value <0.0001). At 20% contrast, the OKR amplitude of the Panx1b$^{-/-}$ fishline was significantly different (P-value <0.0001) where the fishline demonstrated a shorter OKR amplitude compared to TL. At 50% contrast, the rate of the frequency response of the delta peak for both Panx1a$^{-/-}$ and Panx1b$^{-/-}$ was significant (P-value = 0.0227 and P-value = 0.0217 respectively). When the larvae were exposed to 100% contrast the OKR amplitude of the Panx1b$^{-/-}$ was significantly (P-value <0.0001) shorter than the TL.

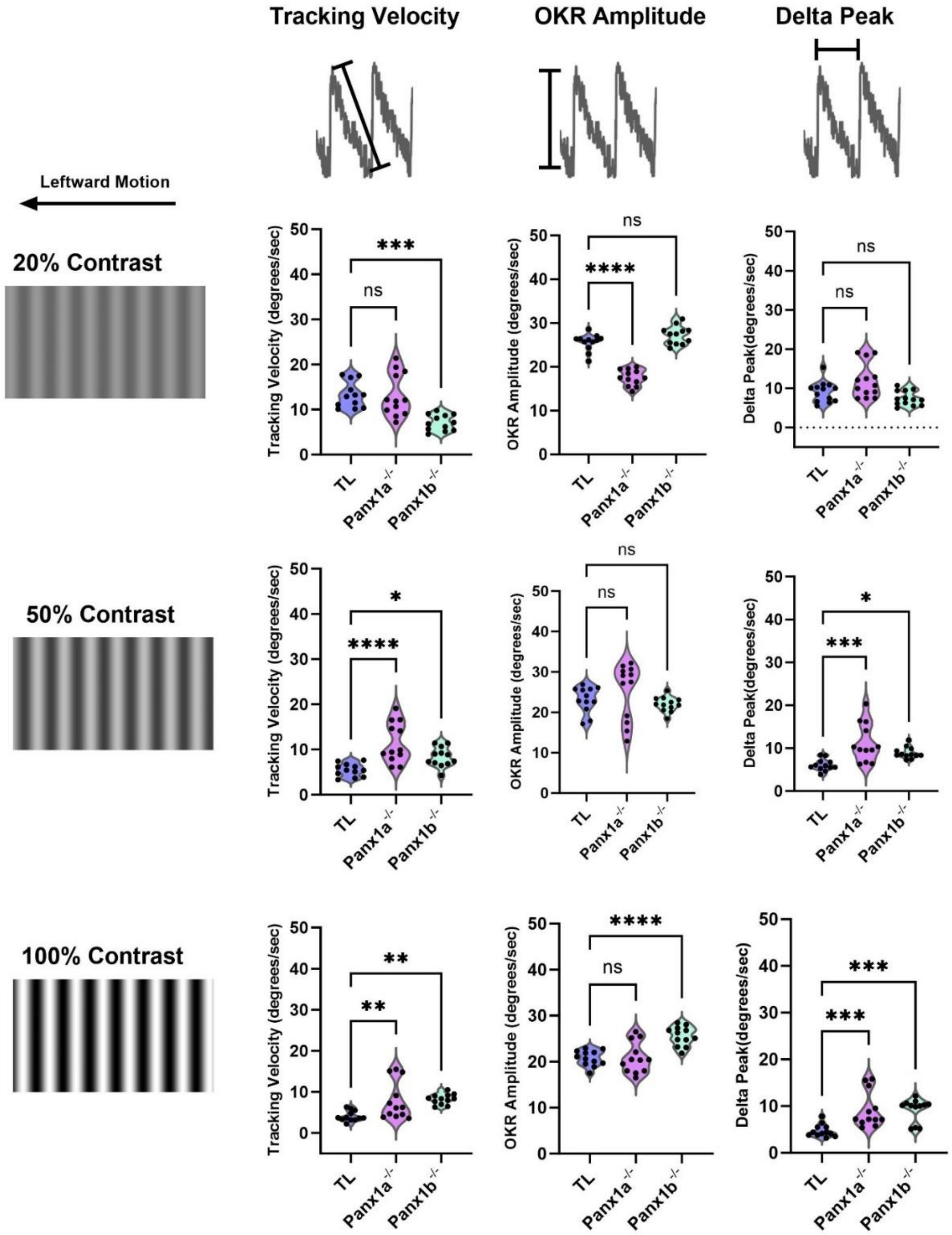

Figure 26. OKR of the 6dpf larvae exposed to leftward moving grating at spatial frequency 0.2. Three parameters were tested: Tracking Velocity, Amplitude, and Delta Peak frequency of saccades. A constant speed of 0.01 degree/second was used to evoke an OKR response at three different contrasts (20%, 50%, 100%). The two treatment lines, Panx1a$^{-/-}$(in magenta) and Panx1b$^{-/-}$(in green), were compared to TL (in blue), and a one-way ANOVA was conducted followed by the Dunnett test was for significance, Alpha < 0.05, Error = SEM.

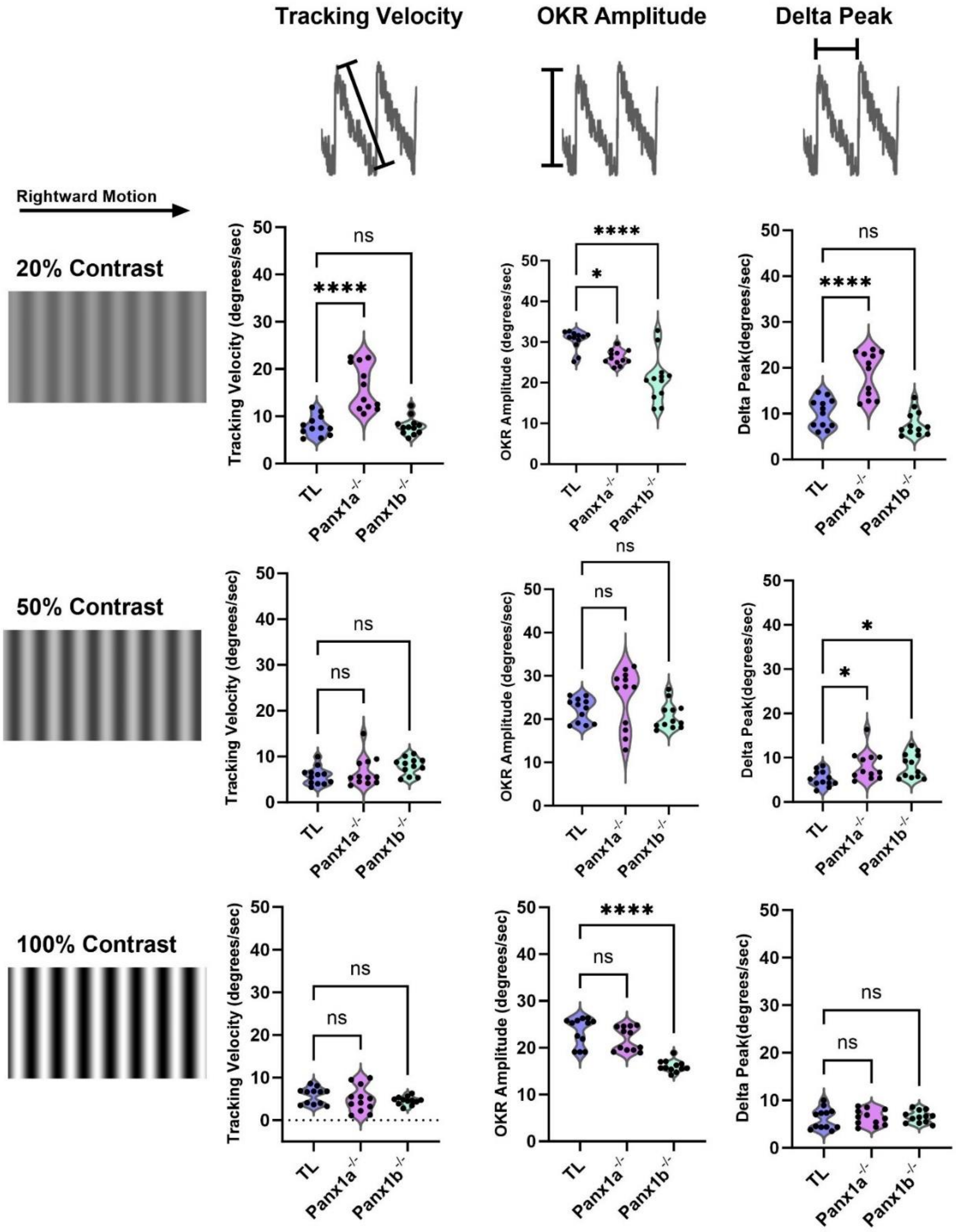

Figure 27. OKR of the 6dpf larvae exposed to rightward moving grating at spatial frequency 0.2. Three parameters were tested: Tracking Velocity, Amplitude, and Delta Peak frequency of saccades. A constant speed of 0.01 degree/second was used to evoke an OKR response at three different contrasts (20%, 50%, 100%). The two treatment lines, Panx1a$^{-/-}$(in magenta) and Panx1b$^{-/-}$(in green), were compared to TL (in blue), and a one-way ANOVA was conducted followed by the Dunnett test was for significance, Alpha < 0.05, Error = SEM.

The second spatial frequency condition that the larvae were tested at was at 0.15 cycle/degree. When the larvae were exposed to the leftward moving grating (**Fig. 28**), the Panx1a$^{-/-}$ demonstrated a significant difference (P-value = 0.0066) when the tracking velocity parameter was analyzed at 20% contrast. This illustrates that the Panx1a$^{-/-}$ fishline takes a long time to generate a single saccade. The Panx1b$^{-/-}$ fishline showed a significant difference at 20% contrast for all three parameters (tracking velocity (P-value = 0.0104), OKR amplitude (P-value = 0.0318), and Delta-peak (P-value = 0.0283)). At 50% contrast, the Panx1a$^{-/-}$ demonstrated a significant difference compared to TL considering parameters like tracking velocity (P-value = 0.0004) and frequency rate of the delta peak (P-value = 0.0075). No significant trends were observed for Panx1b$^{-/-}$ at 50% contrast. At 100% contrast, the response of the Panx1a$^{-/-}$ was significant for all three parameters of tracking velocity (P-value <0.0001), OKR amplitude (P-value = 0.0418), and delta peak (P-value = 0.0013). When the larvae were exposed to the rightward moving grating (**Fig. 29**), the Panx1a$^{-/-}$ demonstrated a significant difference (P-value = 0.0014) in the OKR amplitude response where the genotype generated high amplitude compared to TL at 20% contrast. The Panx1b$^{-/-}$ did not show a significant difference at 20% contrast. There were no significant differences at 50% contrast for the Panx1a$^{-/-}$ fishline. The Panx1b$^{-/-}$ demonstrated a significant difference in tracking velocity (P-value = 0.0014) and OKR amplitude (P-value = 0.0014) at 50% contrast. Finally, at 100% contrast the Panx1a$^{-/-}$ demonstrated a significant difference in tracking velocity (P-value = 0.0003) and frequency of delta peak (P-value = 0.0003). The Panx1b$^{-/-}$ demonstrated a significant difference in the OKR amplitude (P-value = 0.0007) compared to TL.

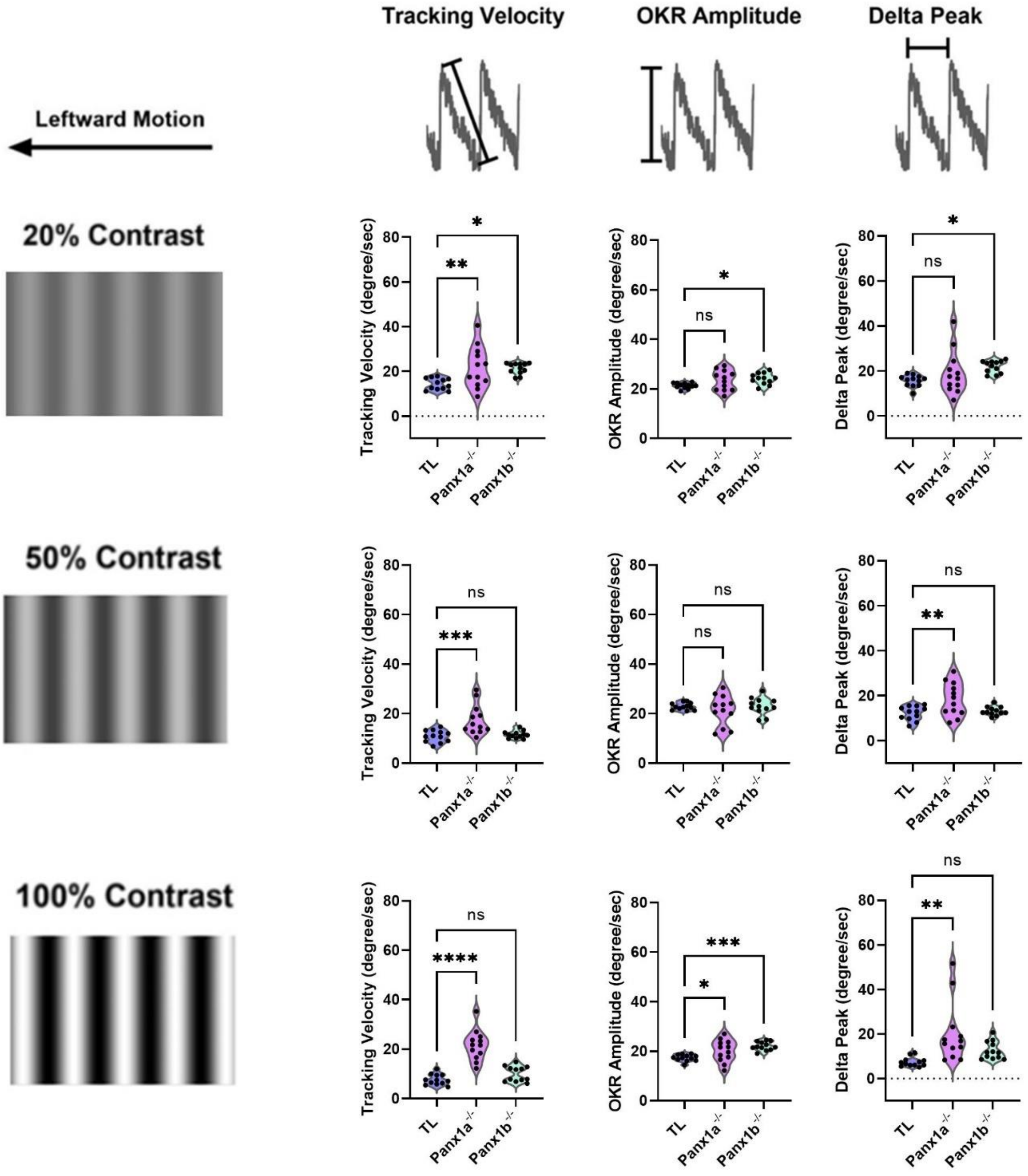

Figure 28. OKR of the 6dpf larvae exposed to leftward moving grating at spatial frequency 0.15. Three parameters were tested: Tracking Velocity, Amplitude, and Delta Peak frequency of saccades. A constant speed of 0.01 degree/second was used to evoke an OKR response at three different contrasts (20%, 50%, 100%). The two treatment lines, Panx1a$^{-/-}$(in magenta) and Panx1b$^{-/-}$(in green), were compared to TL (in blue), and a one-way ANOVA was conducted followed by the Dunnett test was for significance, Alpha < 0.05, Error = SEM.

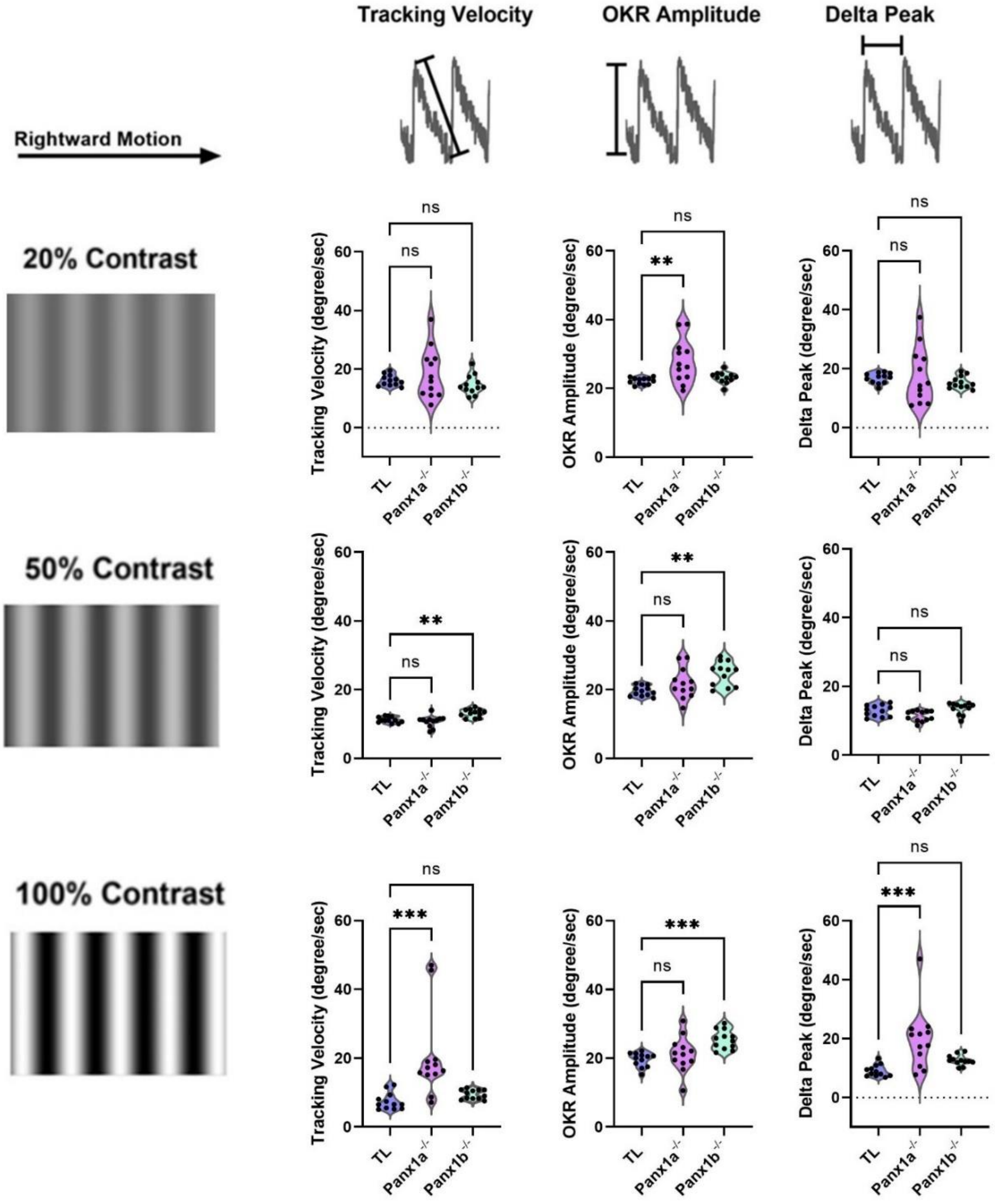

Figure 29. OKR of the 6dpf larvae exposed to rightward moving grating at spatial frequency 0.15. Three parameters were tested: Tracking Velocity, Amplitude, and Delta Peak frequency of saccades. A constant speed of 0.01 degree/second was used to evoke an OKR response at three different contrasts (20%, 50%, 100%). The two treatment lines, Panx1a$^{-/-}$(in magenta) and Panx1b$^{-/-}$(in green), were compared to TL (in blue), and a one-way ANOVA was conducted followed by the Dunnett test was for significance, Alpha < 0.05, Error = SEM.

The last spatial frequency condition was tested at 0.1 cycle/degree which was the threshold for the widest band where the larvae were able to generate saccades. When the larvae were exposed to the leftward moving grating at 0.1 cycle/degree at 20% contrast (**Fig. 30**), the tracking velocity and delta peak in the Panx1a$^{-/-}$ fishline were significant (P-value = 0.0024 and P-value = 0.0261 respectively). The tracking velocity (P-value = 0.0112) and OKR amplitude (P-value <0.0001) of Pax1b$^{-/-}$ at 20% contrast was significant where the fishline took longer to generate a saccade and generated bigger OKR amplitudes compared to TL. At 50% contrast, the response of the tracking velocity (P-value <0.0001) and delta peak (P-value <0.0001) in Panx1a$^{-/-}$ was significant compared to TL. The OKR amplitude of the Panx1a$^{-/-}$ fishline at 50% contrast was significant compared to TL where in this case the average amplitude of the OKR response was significantly smaller (P-value <0.0001). Interestingly at 100% contrast, with a sample size of 12 for Panx1a$^{-/-}$ the tracking velocity was significant compared to TL where the knockout fishline took less time to generate a single saccade compared to TL (P-value = 0.0366). The tracking velocity and delta peak at 100% contrast for the Panx1b$^{-/-}$ fishline was significant compared to TL (P-value = 0.0033 and P-value = 0.0019 respectively).

When the larvae were exposed to the rightward moving grating at 0.1 cycle/degree (**Fig. 31**) at 20% contrast, the Panx1a$^{-/-}$ had a significantly higher OKR amplitude compared to TL (P-value = 0.0102). At 50% contrast the tracking velocity and delta peak of Panx1a$^{-/-}$ are significant compared to TL (P-value = 0.0072 and P-value = 0.0069). The OKR amplitude of the Panx1b$^{-/-}$ was significantly shorter than TL at 50% contrast (P-value = 0.0459). At 100% contrast the Panx1a$^{-/-}$ showed a significant delta peak compared to TL (P-value = 0.0108). The Panx1b$^{-/-}$ showed a significantly faster tracking velocity OKR response compared to TL (P-value = 0.0001).

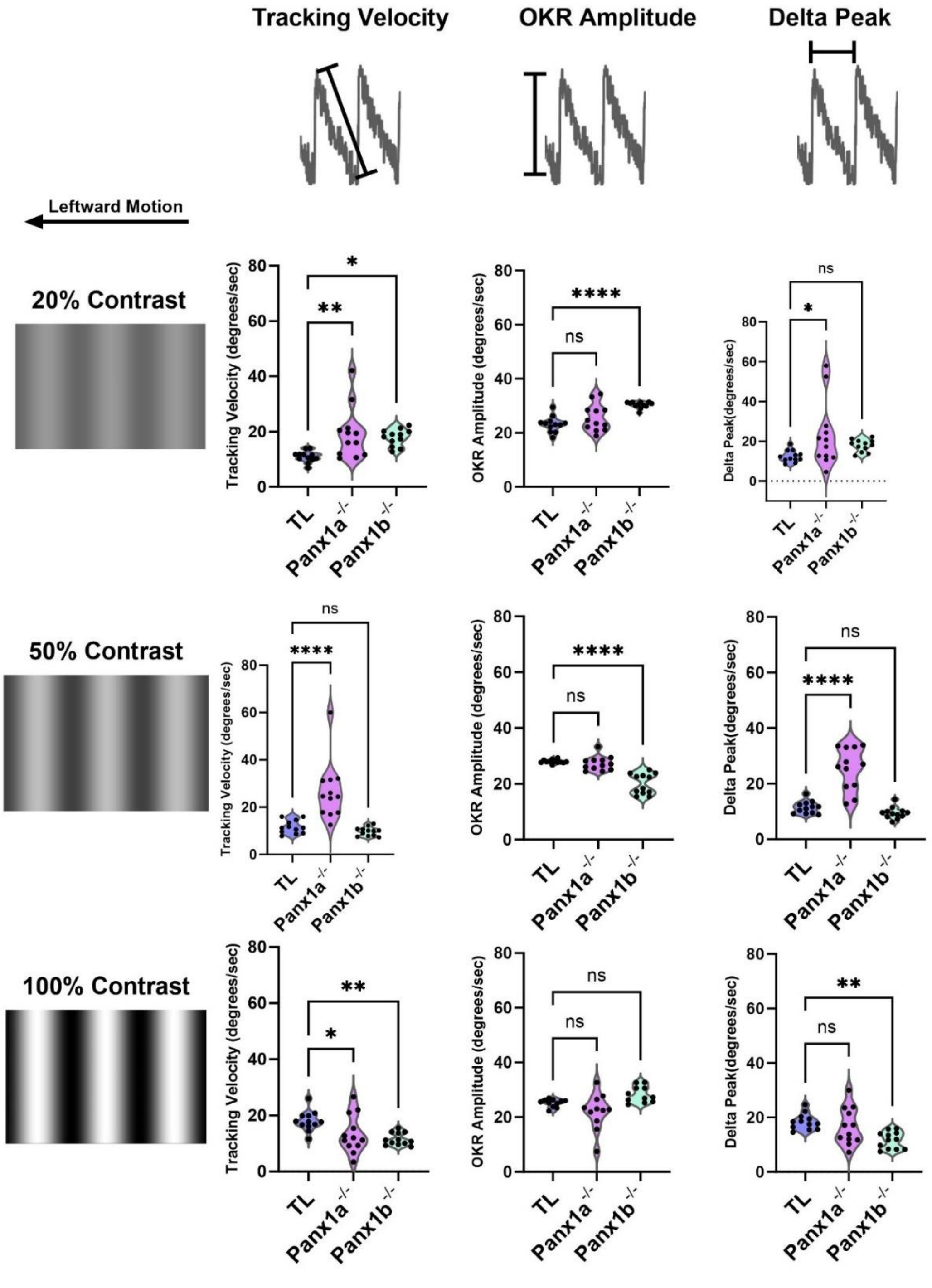

Figure 30. OKR of the 6dpf larvae exposed to the leftward moving grating at spatial frequency 0.1. Three parameters were tested: Tracking Velocity, Amplitude, and Delta Peak frequency of saccades. A constant speed of 0.01 degree/second was used to evoke an OKR response at three different contrasts (20%, 50%, 100%). The two treatment lines, Panx1a$^{-/-}$(in magenta) and Panx1b$^{-/-}$(in green), were compared to TL (in blue), and a one-way ANOVA was conducted followed by the Dunnett test was for significance, Alpha < 0.05, Error = SEM.

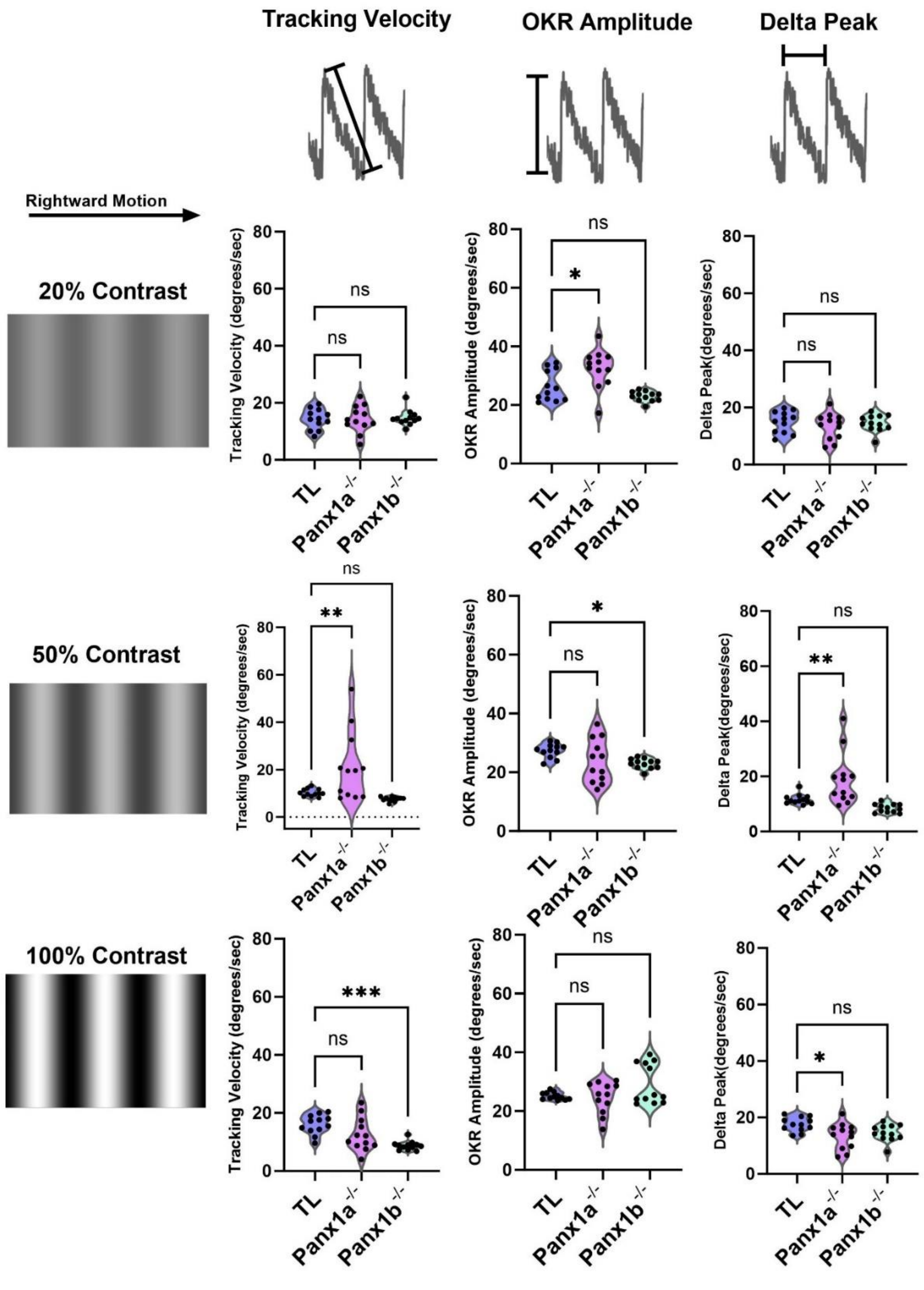

Figure 31. OKR of the 6dpf larvae exposed to the rightward moving grating at spatial frequency 0.1. Three parameters were tested: Tracking Velocity, Amplitude, and Delta Peak frequency of saccades. A constant speed of 0.01 degree/second was used to evoke an OKR response at three different contrasts (20%, 50%, 100%). The two treatment lines, Panx1a$^{-/-}$(in magenta) and Panx1b$^{-/-}$(in green), were compared to TL (in blue), and a one-way ANOVA was conducted followed by the Dunnett test was for significance, Alpha < 0.05, Error = SEM.

5.6. RT-qPCR detected the differential expression of axon guidance pathfinding genes at 3dpf and 6dfp Panx1a-KO and Panx1b-KO

The RT-qPCR protocol was utilized to investigate the regulation of the axon guidance pathfinding genes during early development (3dpf) in the knockout fishlines and was compared to later development (6dpf). Primer pairs were designed to test the expression of 16 genes at 3dpf compared to 6dpf in both Panx1a-KO and Panx1b-KO fishlines (**Fig. 32**).

There was a significant down-regulation of the bdnf3 isoform (0.658-fold) during the early stages of development (3dpf) Panx1a-KO. Interestingly, when the same set of genes was tested at the 6dpf stage of development for Panx1a-KO, there was a significant upregulation of plxna2 (1.68-fold) instead. This demonstrates that there are abnormal regulations during the early developmental stages for Panx1a-KO. The 3dpf Panx1b-KO also showed a significant down-regulation of sema3aa (0.677-fold) and up-regulation of cdk5 (1.854-fold) and plxna2 (1.809-fold). When the same set of genes were tested for the 6dpf Panx1b-KO no significant regulations were observed. This demonstrates that many axon guidance pathfinding genes are regulated during the early stages of development which might impact other processes as the larvae develop. The relative gene expression comparison of the 3dpf larvae with the 6dpf larvae for each genotype (TL, Panx1a-KO, Panx1b-KO) was conducted for the axon guidance pathfinding genes (**Fig. 33**). We found a downregulation of the gene expression for all genotype as the larvae develop showing that either there is more tissue to gene ratio, or the axon guidance pathfinding genes are not as expressed during the later stages of larval development.

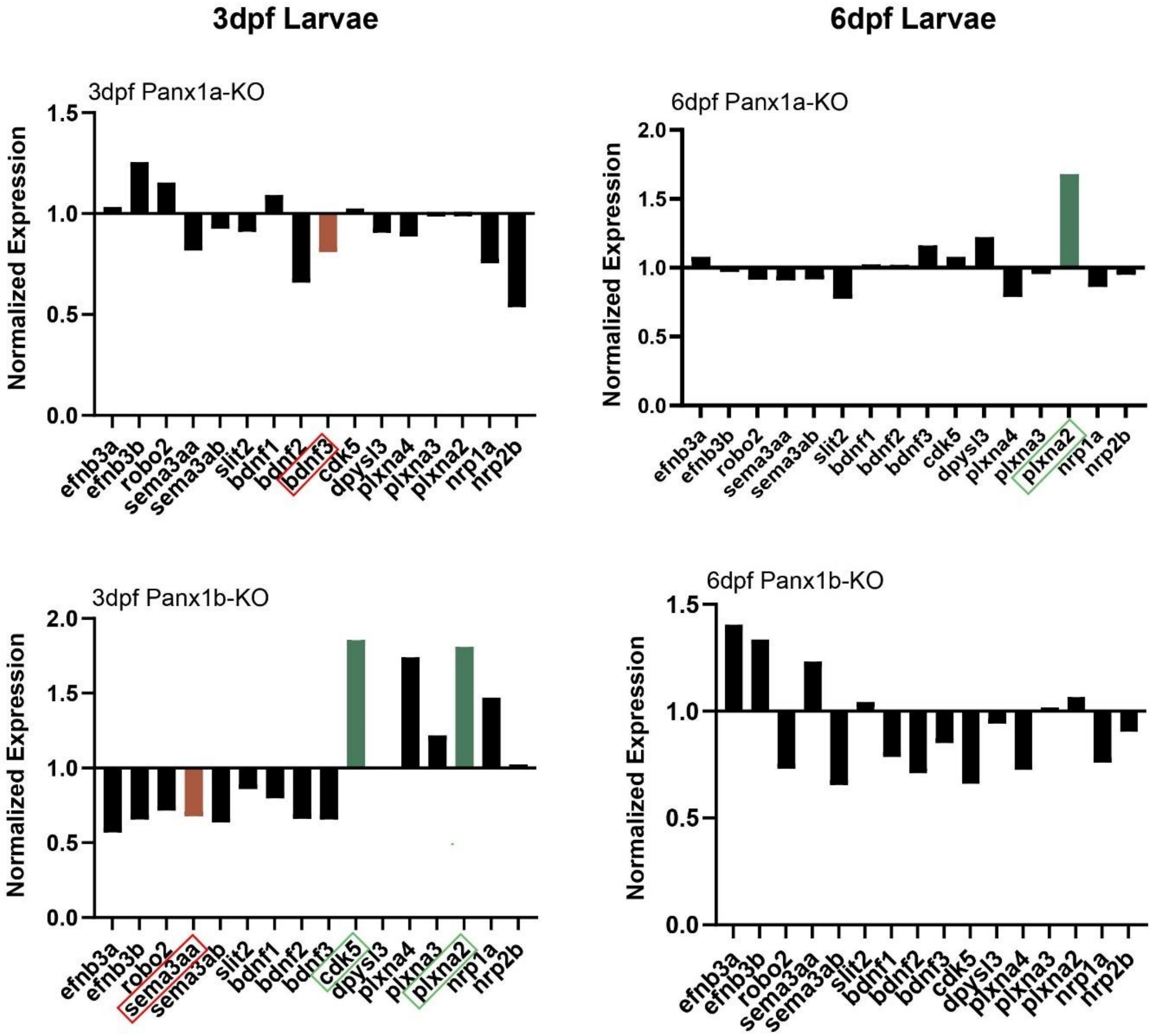

Figure 32. The differential expression of axon guidance pathfinding genes in 3dpf and 6dpf Panx1a-KO and Panx1b-KO was determined through RT-qPCR and compared with 3dpf and 6dpf TL. Sixteen genes were selected from the axon guidance pathfinding pathway. The regulation of genes in the 3dpf Panxla-KO, 6dpf Panx1a-KO, 3dpf Panx1b-KO, and the 6dpf Panx1b-KO. The gene expression was normalized to 1. The red bars represent downregulation, and the green bars represent upregulation of the selected genes.

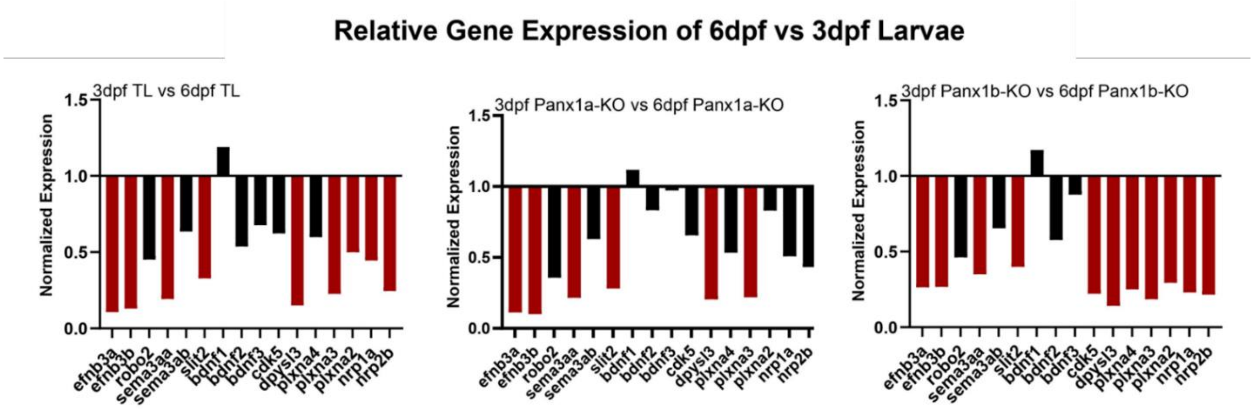

Figure 33. The differential expression of axon guidance pathfinding genes in 3dpf compared to 6dpf TL, Panx1a-KO, and Panx1b-KO was determined through RT-qPCR. Sixteen genes were selected from the axon guidance pathfinding pathway. The regulation of genes in the 3dpf larvae was compared to 6dpf larvae for each genotype (TL, Panxla-KO, Panx1b-KO). The relative gene expression was normalized to 1. The red bars represent downregulation, either representing a decrease in expression as the larvae grow or a more tissue-to-gene ratio.

5.7. Loss of Panx1a and Panx1b ablation effects differential gene expression confirmed by RNA-seq analysis

In this section, the RNA-seq data involved in regulating astrocytes, axons, dendrites, synapses, retinal axon guidance, and axon guidance pathfinding genes were screened using Excel (2016). The analysis of the RNA-seq data for the 6dpf Panx1a$^{-/-}$ and Panx1b$^{-/-}$ was conducted at SickKids (Toronto, ON). The genes involved in the specific regulations were downloaded from the Zebrafish Information Network (ZFIN) database (https://zfin.org/) and compared to the RNA-seq data acquired for 6dpf Panx1a$^{-/-}$ and Panx1b$^{-/-}$ and screened, sorted, and analyzed with Excel (2016). The screening of the RNA-seq data demonstrated that there are many upregulations and down-regulations of genes involved in regulating astrocytes, axons, dendrites, synapses, retinal axon guidance, and axon guidance pathfinding genes for both the 6dpf Panx1a$^{-/-}$ and Panx1b$^{-/-}$ (**Fig. 34-39**). This shows knocking out functional Panx1a and Panx1b may result in abnormal gene regulations, which affects the organization of the neuronal circuitry and cell-to-cell communications in these fishlines.

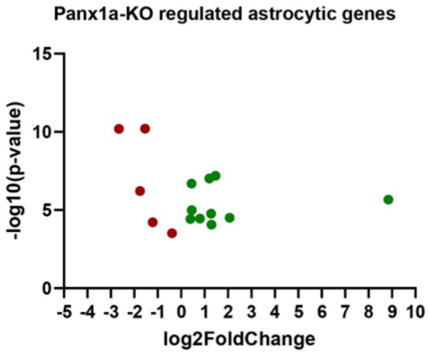

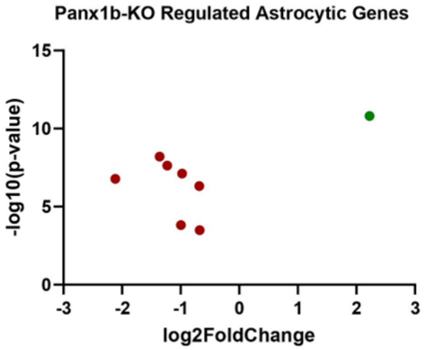

TL VS PANX1A$^{-/-}$

GENE NAME	*log2FoldChange*	*pvalue*	*padj*
IGF1RB	0.396903	3.7E-05	0.001769
INS	1.280769	1.7E-05	0.00094
INSRA	0.441692	2.01E-07	2.17E-05
ITGA6B	0.808309	3.46E-05	0.001675
ITGA6B	1.200599	9.69E-08	1.13E-05
KMT2A	-2.65699	6.31E-11	1.52E-08
KMT2A	0.451506	1.02E-05	0.00062
NPHP1	-1.21401	6.04E-05	0.002622
PCNA	-1.7571	6.08E-07	5.49E-05
RNASET2	-1.53356	6.23E-11	1.51E-08
RNASET2	1.468365	6.4E-08	7.8E-06
S100A10A	1.297178	8.58E-05	0.003458
SART1	-0.38452	0.000302	0.009267
SLCO1C1	8.845234	2.15E-06	0.000165
SOX9A	2.070326	3.13E-05	0.001546

TL VS PANX1B$^{-/-}$

GENE NAME	*log2FoldChange*	*pvalue*	*padj*
ATP1A2A	-0.67597	0.00032	0.008661
F8	-0.99612	0.000152	0.00471
GNL3	-0.68087	4.8E-07	3.79E-05
KCNJ13	-1.22796	2.37E-08	2.75E-06
KMT2A	-2.11408	1.64E-07	1.51E-05
MAK16	-0.9764	7.63E-08	7.86E-06
RNASET2	-1.35765	6.22E-09	8.54E-07
S100A10A	2.223369	1.55E-11	3.62E-09

Figure 34. The differential expression of astrocytic genes in 6dpf Panx1a-KO and 6dpf Panx1b-KO. The analysis of the RNA-seq data was performed at SickKids (Toronto, ON). The genes were extracted, sorted, and analyzed using Excel with the adjusted p-value (p-value<0.01). GraphPad Prism was used for the scatter plots using the log2FoldChange with -log10(p-value).

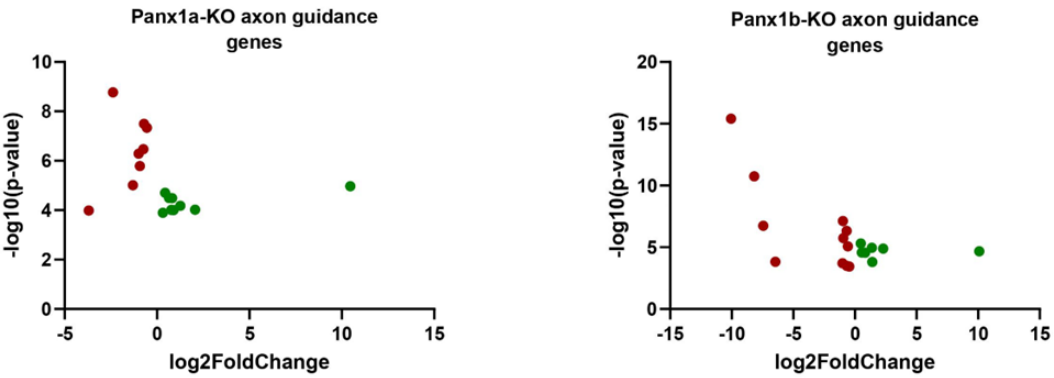

TL VS PANX1A$^{-/-}$

GENE NAME	***log2FoldChange***	***pvalue***	***padj***
ACLYA	-0.55045342	4.63E-08	5.85E-06
ARNT2	0.646246493	3.21E-05	0.001581
CDH11	-0.702550426	3.21E-08	4.21E-06
DPYSL5A	-1.301131695	9.67E-06	0.000598
EFNA1A	0.437616587	1.99E-05	0.001071
KIF1B	-0.926950254	1.64E-06	0.000131
LRTM2A	0.770368185	9.64E-05	0.00379
MYOT	0.891024345	9.85E-05	0.003855
NFASCA	10.46436036	1.06E-05	0.00064
NFASCA	-0.995262728	5.11E-07	4.69E-05
PLOD3	2.057285941	9.47E-05	0.003742
SEMA4AB	0.813451711	3.26E-05	0.001594
SEMA4AB	-2.385950196	1.69E-09	2.94E-07
SI:DKEY-49N23.1	-3.690420844	0.000102	0.003957
SLC17A6B	1.263326444	6.56E-05	0.002818
SPAST	-0.742974603	3.38E-07	3.4E-05
WNK1B	0.317761513	0.000128	0.00474

TL VS PANX1B$^{-/-}$

GENE NAME	***log2FoldChange***	***pvalue***	***padj***
ABHD12	-0.579361415	8.39E-06	0.00044
ACHE	-0.45753352	0.000361	0.00939
COL4A6	1.375827496	1.1E-05	0.000544
EFNA1A	0.469816286	4.87E-06	0.00028
GNL3	-0.680872323	4.8E-07	3.79E-05
MAK16	-0.976398904	7.63E-08	7.86E-06
NCALDB	-1.003416649	0.000193	0.005723
NFASCA	10.09996667	2.13E-05	0.000963
NFASCA	-0.946842635	1.81E-06	0.000122
PLOD3	-6.462564623	0.000147	0.004583
PLOD3	2.293346374	1.29E-05	0.000625
RAB33BA	0.55991601	2.65E-05	0.001152
RAG1	1.415737482	0.000154	0.004737
SEMA4AB	0.822051371	2.74E-05	0.001179
SEMA4AB	-10.06367304	3.85E-16	2.2E-13
SI:DKEY-49N23.1	-7.439086376	1.78E-07	1.61E-05
SLC17A6B	-8.183042013	1.81E-11	4.19E-09
VASNA	-0.660314905	0.000321	0.008674

Figure 35. The differential expression of axon guidance genes in 6dpf Panx1a-KO and 6dpf Panx1b-KO. The analysis of the RNA-seq data was performed at SickKids (Toronto, ON). The genes were extracted, sorted, and analyzed using Excel with the adjusted p-value (p-value<0.01). GraphPad Prism was used for the scatter plots using the log2FoldChange with -log10(p-value).

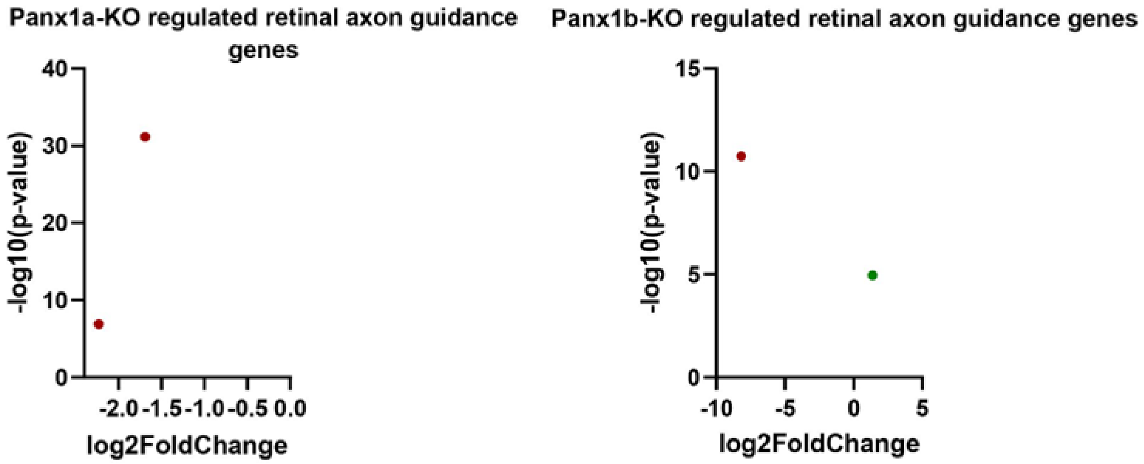

TL VS PANX1A$^{-/-}$

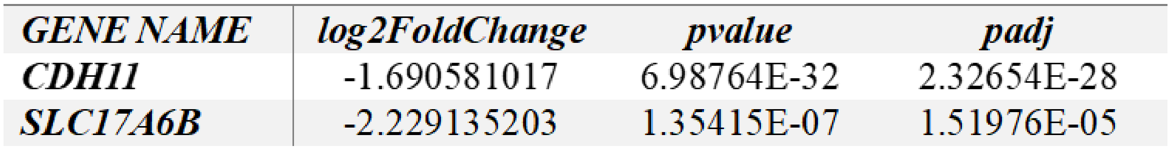

GENE NAME	***log2FoldChange***	***pvalue***	***padj***
CDH11	-1.690581017	6.98764E-32	2.32654E-28
SLC17A6B	-2.229135203	1.35415E-07	1.51976E-05

TL VS PANX1B$^{-/-}$

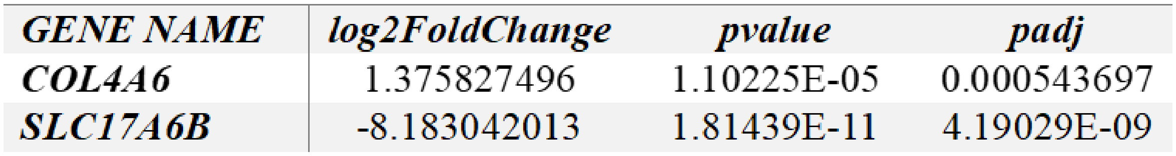

GENE NAME	***log2FoldChange***	***pvalue***	***padj***
COL4A6	1.375827496	1.10225E-05	0.000543697
SLC17A6B	-8.183042013	1.81439E-11	4.19029E-09

Figure 36. The differential expression of retinal axon guidance genes in 6dpf Panx1a-KO and 6dpf Panx1b-KO. The analysis of the RNA-seq data was performed at SickKids (Toronto, ON). The genes were extracted, sorted, and analyzed using Excel with the adjusted p-value (p-value<0.01). GraphPad Prism was used for the scatter plots using the log2FoldChange with -log10(p-value).

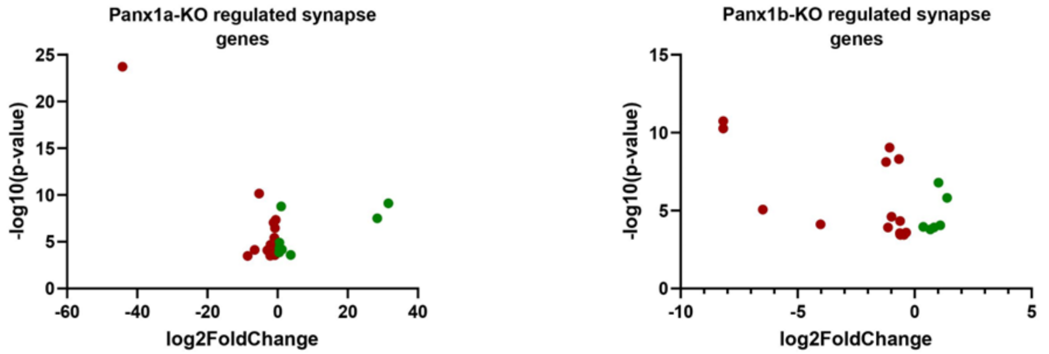

TL VS $PANX1A^{-/-}$

GENE NAME	***log2FoldChange***	***pvalue***	***padj***
ACLYA	-0.55045342	4.63E-08	5.85E-06
ATP6V0CB	-0.817007678	0.000242	0.007748
BCR	-0.925708581	3.73E-06	0.000268
CACNB4A	3.738400371	0.000257	0.008177
DOC2D	-5.256944646	6.88E-11	1.63E-08
GPHNA	-44.18898743	1.93E-24	2.97E-21
HIP1	-2.943138298	8.03E-05	0.003284
KIF3B	28.42205401	3.13E-08	4.13E-06
NETO2B	31.59042977	7.68E-10	1.5E-07
P2RX7	-1.12651694	8.8E-08	1.03E-05
PSEN2	-0.53705449	0.000134	0.004941
RBM8A	-0.340736233	0.000129	0.004775
SDCBP2	-0.605470103	0.000152	0.005422
SI:DKEY-11O1.6	-2.093672333	0.000315	0.009571
SLC12A7A	1.052946147	1.67E-09	2.93E-07
SLC17A6B	1.263326444	6.56E-05	0.002818
SLITRK6	0.504273355	1.23E-05	0.000723
SNAPIN	-0.756115924	0.000273	0.008561
SNTB2	-6.538485769	7.34E-05	0.003068
SPAST	-0.742974603	3.38E-07	3.4E-05
STAU1	-8.554053437	0.000324	0.009811
TIAM1A	0.559630551	0.000104	0.003991
TJP1B	0.411124639	3.43E-05	0.001665
UTRN	0.471040215	0.000136	0.004976
VWA1	-2.000805645	2.13E-05	0.001131

TL VS $PANX1B^{-/-}$

GENE NAME	***log2FoldChange***	***pvalue***	***padj***
ACHE	-0.45753352	0.000361	0.00939
ATF4A	-0.361182736	0.000253	0.007105
CHRNB1	-0.624852864	4.7E-05	0.001845
CHRNE	-0.989973266	2.49E-05	0.001093
FXR1	-1.074504814	8.96E-10	1.47E-07
FXR2	-0.667433833	4.96E-09	6.96E-07
GAN	0.832553378	0.000121	0.00394
GRM6B	-8.17579129	5.38E-11	1.15E-08
MYLKB	-0.61986225	0.000344	0.00909
MYO7AA	0.370179301	0.000109	0.003644
NLGN4XB	-4.0170918	7.62E-05	0.00273
SLC12A7A	0.668516408	0.000159	0.004881
SLC17A6B	-8.183042013	1.81E-11	4.19E-09
SLC1A2A	-1.137197081	0.000122	0.003958
SLC8A1B	1.018916613	1.62E-07	1.49E-05
SNAPIN	-1.220966374	7.58E-09	1.01E-06
SNCGA	-0.630707075	0.000274	0.007602
SNCGA	1.092141276	8.87E-05	0.003068
SYNGR2B	-0.600367306	0.000361	0.009385
SYNM	-0.452365434	0.00034	0.009012
SYT1A	1.385765814	1.5E-06	0.000103
ZMYND19	-6.489968302	8.58E-06	0.000448

Figure 37. The differential expression of synapse genes in 6dpf Panx1a-KO and 6dpf Panx1b-KO. The analysis of the RNA-seq data was performed at SickKids (Toronto, ON). The genes were extracted, sorted, and analyzed using Excel with the adjusted p-value (p-value<0.01). GraphPad Prism was used for the scatter plots using the log2FoldChange with -log10(p-value).

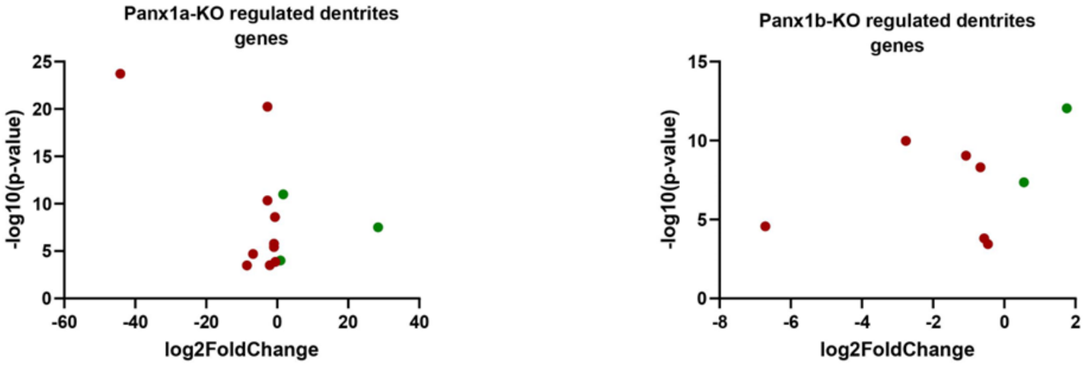

TL VS PANX1A$^{-/-}$

GENE NAME	***log2FoldChange***	***pvalue***	***padj***
ARF6B	-6.828008051	1.96373E-05	0.001058823
BCR	-0.925708581	3.73156E-06	0.000268149
GPHNA	-44.18898743	1.93392E-24	2.97184E-21
KIF1AA	1.674896554	1.01225E-11	2.93068E-09
KIF1B	-0.926950254	1.64038E-06	0.000131342
KIF3B	28.42205401	3.12951E-08	4.12661E-06
MARK2A	-2.765916948	4.51539E-11	1.12755E-08
MYOT	0.891024345	9.85131E-05	0.003855036
NEDD4L	-0.652627085	2.50081E-09	4.25181E-07
PANX1A	-2.725327313	5.68226E-21	7.09466E-18
PSEN2	-0.53705449	0.000134184	0.004941183
SI:DKEY-11O1.6	-2.093672333	0.00031476	0.009570728
STAU1	-8.554053437	0.000324377	0.009810865

TL VS PANX1B$^{-/-}$

GENE NAME	***log2FoldChange***	***pvalue***	***padj***
ACHE	-0.45753	0.000361467	0.00939015
ARF6B	-6.71392	2.69703E-05	0.00116873
FXR1	-1.0745	8.95697E-10	1.4727E-07
FXR2	-0.66743	4.9624E-09	6.95676E-07
KIF1AA	1.759358	8.91484E-13	2.73987E-10
MARK2A	-2.76343	1.03988E-10	2.109E-08
MARK2B	0.551848	4.34134E-08	4.79154E-06
ULK2	-0.56406	0.000156725	0.004818045

Figure 38. The differential expression of dendritic genes in 6dpf Panx1a-KO and 6dpf Panx1b-KO. The analysis of the RNA-seq data was performed at SickKids (Toronto, ON). The genes were extracted, sorted, and analyzed using Excel with the adjusted p-value (p-value<0.01). GraphPad Prism was used for the scatter plots using the log2FoldChange with -log10(p-value).

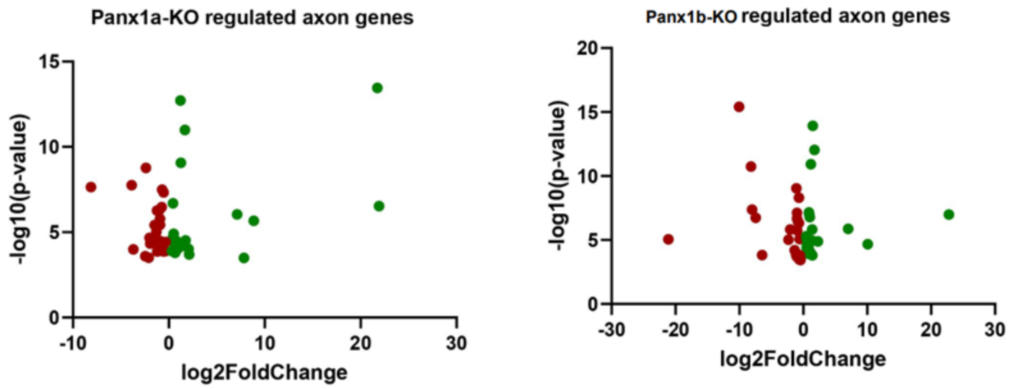

TL VS PANX1A$^{-/-}$

GENE NAME	log2FoldChange	pvalue	padj
ACLYA	-0.55045342	4.62614E-08	5.84914E-06
ALDOAA	-0.955990209	8.06873E-05	0.003296298
ARHGAP35A	1.251806118	8.63719E-10	1.6671E-07
ARNT2	0.646246493	3.21278E-05	0.001580828
BCR	-0.925708581	3.73156E-06	0.000268149
CDH11	-0.702550426	3.21121E-08	4.20658E-06
COL6A4A	-1.409496092	2.30314E-05	0.001207605
CRTAC1A	-8.124781044	2.26472E-08	3.10944E-06
DPYSL5A	-1.301131695	9.66915E-06	0.000598021
EFNA1A	0.437616587	1.99372E-05	0.001070662
EXOSC3	0.65606379	0.000163049	0.005729517
GPM6AB	-2.44448583	0.000257513	0.008177373
HDAC6	7.828173547	0.000324014	0.009807322
HER4.4	-1.471533209	3.78075E-06	0.000270343
IGF1RB	0.396903258	3.69719E-05	0.00176907
INSRA	0.441691919	2.01361E-07	2.17437E-05
KIF1AA	1.674896554	1.01225E-11	2.93068E-09
KIF1B	-0.926950254	1.64038E-06	0.000131342
LGMN	-0.947591841	3.24899E-05	0.001592324
LINGO1A	21.92297656	2.94785E-07	3.01223E-05
LRTM2A	0.770368185	9.6388E-05	0.00379044
MALB	-3.867352313	1.75974E-08	2.46697E-06
MYOT	0.891024345	9.85131E-05	0.003855036
NFASCA	-0.995262728	5.11023E-07	4.69365E-05
PAFAH1B1A	-0.348747023	3.71425E-05	0.001772986
PARD3AB	2.123690447	0.000200298	0.006696835
PINK1	1.219422025	1.91466E-13	8.22563E-11
PITPNAA	-1.097532599	0.000109654	0.004156528
PLLP	-1.231952788	5.41193E-07	4.94802E-05
PLOD3	2.057285941	9.46931E-05	0.003742206
PSEN2	-0.53705449	0.000134184	0.004941183
RBM8A	-0.340736233	0.00012919	0.004774904
RGMA	-1.213451902	0.000136704	0.005010874
SC:D189	-1.939482261	4.62007E-05	0.002116862
SEMA4AB	0.813451711	3.26262E-05	0.001593578
SEMA4AB	-2.385950196	1.68714E-09	2.94358E-07
SI:DKEY-11O1.6	-2.093672333	0.00031476	0.009570728
SI:DKEY-49N23.1	-3.690420844	0.000102119	0.0039574
SLC17A6B	1.263326444	6.55985E-05	0.002818196
SLCO1C1	8.84523358	2.1486E-06	0.00016543
SLITRK6	0.504273355	1.2277E-05	0.000722781
SNRNP70	1.746239975	3.04736E-05	0.001512476

TL VS PANX1B$^{-/-}$

GENE NAME	log2FoldChange	pvalue	padj
ABHD12	-0.579361415	8.3892E-06	0.000439871
ACHE	-0.45753352	0.000361467	0.00939015
APPA	-2.066416608	1.49663E-06	0.000102919
CNP	-8.012185312	4.24711E-08	4.70053E-06
COL4A6	1.375827496	1.10225E-05	0.000543697
COL6A4A	-1.334285065	6.23831E-05	0.002318564
COX5AB	0.876094061	7.04268E-08	7.32769E-06
DNAH3	1.49414936	1.20801E-14	5.24616E-12
EFNA1A	0.469816286	4.87119E-06	0.000279631
EXOSC3	-0.990306431	2.07523E-07	1.84663E-05
EXOSC3	0.923095969	9.34555E-08	9.3348E-06
FXR1	-1.074504814	8.95697E-10	1.4727E-07
FXR2	-0.667433833	4.9624E-09	6.95676E-07
GAN	0.832553378	0.000120802	0.003940021
GNL3	-0.680872323	4.79594E-07	3.79439E-05
HSD17B4	0.527893804	7.63773E-06	0.000403648
HYDIN	1.192066109	1.17874E-11	2.87168E-09
KIF1AA	1.759358356	8.91484E-13	2.73987E-10
LEF1	0.52606377	4.15821E-05	0.001659711
LINGO1A	22.77259525	1.00207E-07	9.91006E-06
MAK16	-0.976398904	7.63305E-08	7.86007E-06
NCALDB	-1.003416649	0.000193247	0.005723497
NFASCA	10.09996667	2.1288E-05	0.000963238
NFASCA	-0.946842635	1.80963E-06	0.000121607
PAK1	-0.902367529	0.000188372	0.005606225
PITPNAA	-1.065925082	0.000174845	0.005268397
PLOD3	-6.462564623	0.000147056	0.004582778
PLOD3	2.293346374	1.28978E-05	0.000624629
RAB33BA	0.55991601	2.64996E-05	0.001152082
RAG1	1.415737482	0.000153669	0.00473743
SCN8AB	-21.12625721	8.73052E-06	0.000453601
SEMA4AB	0.822051371	2.73502E-05	0.001178804
SEMA4AB	-10.06367304	3.85134E-16	2.19824E-13
SI:DKEY-49N23.1	-7.439086376	1.78159E-07	1.61045E-05
SLC17A6B	-8.183042013	1.81439E-11	4.19029E-09
SLC1A2A	-1.137197081	0.000121655	0.003958159
SLC8A1B	1.018916613	1.61776E-07	1.4893E-05
SNCGA	-0.630707075	0.00027398	0.007601794
SNCGA	1.092141276	8.8683E-05	0.003067742
SPI1B	-2.310143088	9.52278E-06	0.000484527
ST8SIA6	-0.805312276	3.82725E-07	3.13758E-05
SYNM	-0.452365434	0.000339646	0.009012032

Figure 39. The differential expression of axon genes in 6dpf Panx1a-KO and 6dpf Panx1b-KO. The RNA-seq data was analyzed at SickKids (Toronto, ON). The genes were extracted, sorted, and analyzed using Excel with the adjusted p-value (p-value<0.01). GraphPad Prism was used for the scatter plots using the log2FoldChange with -log10(p-value).

6. Discussion

Both Panx1a and Panx1b play essential roles in the physiology of the zebrafish vision based on past work done by the lab (Safarian et al., 2020; Safarian et al., 2021; Cenedese et al., 2017). The loss of Panx1a led to changes in visuomotor behavior and was associated with light decrement detection and abnormal responses to visual stimulus through the retinal OFF-pathway via dopaminergic and adenosine signaling pathways (Safarian et al., 2020). In the adult zebrafish, the Panx1a is also involved in a negative feedback pathway from the horizontal cell layers to the cones in the photoreceptor layer which aids in generating centre/ surround organization of the receptive fields of the bipolar cells (Cenedese et al., 2017). The absence of the Panx1b channels in the zebrafish larvae disrupts the retinal response causing the larvae to experience difficulties in navigating the leftward motion in low light conditions (Safarian et al., 2021). The Panx1b was suggested to be involved in modulating the circadian clock system, mediating the sleep-wake cycle of the zebrafish visual system in forming non-visual processes (Safarian et al., 2021).

This project investigated the larvae's optic flow response to their biased direction selectivity in the Panx1a-KO and Panx1b-KO fish lines at molecular, systems, and behavioral levels. It has been proposed that Panx1a and Panx1b modulate the axonal growth in axon guidance pathfinding and together are interconnected to the habenula region, leading to synaptic plasticity of the retinal neural circuitry, and regulating visually guided locomotion in the zebrafish larvae.

6.1. Loss of functional Panx1a and Panx1b affects the eye movement response of the 6dpf larvae

The expression of Panx1a and Panx1b in the retina serves the physiological role(s) of the two proteins in visual processing as mentioned earlier (Safarian et al., 2020; Safarian et al., 2021; Cenedese et al., 2017). The saccadic eye movement of the 6dpf Panx1a-KO and Panx1b-KO larvae compared to TL was investigated using OKR which tests the function of the RGC response to see whether the fish exhibit ocular motor deficiencies and/or if they follow the direction of the motion. The strategy aimed at understanding the kinematic properties of eye movement in the knockout fishlines by exposing the fish to three different contrasts (20%, 50%, 100%), three different spatial frequencies (0.2, 0.15, 0.1), leftward and rightward directions of the moving grating, and a constant speed to evoke an OKR response. It was found that Panx1a$^{-/-}$ and Panx1b$^{-/-}$ display ocular motor deficiencies. The larvae generated the most saccades when exposed to the narrowest spatial frequency band (0.2cycle/degree) and as the contrast was lowered the number of saccades also decreased. In terms of generating saccades, the Panx1b$^{-/-}$ performed similarly to TL but when the individual parameters were analyzed we found that Panx1b$^{-/-}$ displayed shorter amplitudes and slower saccades compared to TL. The majority of the Panx1a$^{-/-}$ couldn't maintain and generate saccades compared to TL, which is evidence for the knockout fishline exhibiting ocular motor deficiencies.

Different pathologies can change the frequency, size, and timing of the saccades (Jensen et al., 2019). Depending on which parameters are displaying an abnormal pattern, the pathologies can represent cerebellar disorders and/or neurodegenerative disorders (Kassavetis et al., 2022). Abnormal saccadic amplitude is observed in pathological conditions such as saccadic dysmetria where the patient displays short saccades due to monocular muscular weakness (Paeve & Laurent, 2011). The slow saccades can also be linked to spinocerebellar ataxia, an autosomal dominant disorder that has been suggested to be due to reduced activity of the brainstem (Szmulewicz et al., 2011). This can be due to inhibition of the excitatory burst neurons that leads to generating slow saccades both horizontally and vertically (Szmulewicz et al., 2011). In addition, slow saccadic eye movement has also been linked to patients with advanced

Parkinson’s disease displaying increased hypometria where they underreach the object of interest during voluntary muscle movement (Garbutt et al., 2004). In this condition, it takes more time to reach the object of interest and as a result, exhibit slow saccades. Slowing of saccades can also be observed in other neurological conditions such as Huntington’s disease, Lewy bodies, and corticobasal degeneration as well (Jensen et al., 2019). The deficiencies in generating saccadic eye movement are indicative of ocular motor deficiencies which are linked to neurological disorders (Grossman & Rucker et al., 2023). Hence both Panx1a$^{-/-}$ and Panx1b$^{-/-}$ display ocular motor deficiencies. Interestingly, in multiple studies Panx1 has been linked to neuroinflammation in Parkinson’s disease where Panx1 is involved in activating neuroinflammation in astrocytes and neurons (Silverman et al., 2009; Frederiksen et al., 2019; Ling et al., 2021) and hence the slow eye movement could be due to neurological conditions. In another study by Shestopalov and colleagues (2016), the researchers found that Panx1 is involved in inflammatory pathways that are associated with the loss of retinal ganglion cell and optic nerve damage which is seen in glaucoma cases. In this condition, glaucoma patients experience longer saccade latencies, which are delayed with increasing glaucoma severity (McDonald et al., 2022). Other saccadic abnormalities in glaucoma patients include lower saccade amplitude (decreased gain), lower saccade velocity, and difficulty inhibiting reflexive saccades (McDonald et al., 2022) and this could be another explanation for the Panx1a$^{-/-}$ fishline demonstrating longer saccade latencies and velocities. In general, understanding the frequency of saccades helps us to assess the efficacy and precision of the larvae’s visual tracking behavior and provides insight to potential impairments and abnormalities.

6.2. Both Panx1a and Panx1b are involved in regulating axon guidance genes and play a pivotal role in cell-to-cell and neuronal communication

Throughout development, all axons are guided to the appropriate targets with the help of guidance molecules. Axons go through complex pathways to reach their destination and based on these guidance cues, the tip of the axons or the growth cone gets repelled or attracted towards precise directions for their specific neural connection (Tesssier-Lavigne & Goodman, 1996). By performing RT-qPCR, the regulation of the axon guidance pathfinding genes on a molecular level was investigated. In addition, RNA-seq analysis was done to see abnormal regulation of genes involved in axon guidance pathfinding, retinal axon guidance, axon, astrocyte, synapse, and dendrites of the 6dpf Panx1a$^{-/-}$ and Panx1b$^{-/-}$ fishlines. The goal was to see if there is abnormal regulation of these genes during the early stages of larval development in the Panx1a-KO and Panx1b-KO fishlines compared to the TL. We found that there was a down-regulation of bdnf3 during the early stages of development (3dpf) in the Panx1a-KO. The Brain-derived neurotrophic factor (BDNF) is involved in neuronal connectivity and synaptic plasticity during brain development by increasing the axonal branches and the forming of presynaptic sites (Cohen-Cory et al., 2011). Interestingly, when the same set of genes was tested at the 6dpf stage of development for Panx1a-KO, there was an upregulation of plxna2 which is involved in mediating axon guidance activity and binds to Semaphorin (Andermatt et al., 2014). Semaphorin is one of the main axon guidance molecules that bind to neuropilins and plexins and are involved in guiding axons to the right target (Andermatt et al., 2014). This demonstrates that there are abnormal regulations during the early stages of development for Panx1a-KO. The 3dpf Panx1b-KO also showed a down-regulation of sema3aa and up-regulation of cdk5 and plxna2. The sema3aa is from the Semaphorin family and it is a guidance cue molecule that guides axons to the right destination by repulsing (Nakamura & Strittmatter, 2000). The cdk5 mediates axonogenesis which is a process involved in axonal extension through growth cone activity (Connell-Crowley & Giniger 2000). When the same set of genes were tested for the 6dpf Panx1b-KO no significant regulations were observed. This demonstrates that many axon guidance pathfinding genes are regulated during the early stages of development where we suggest that it alters these guidance cues molecules and causes a rearrangement of the neuronal circuitry as the larvae develop. The RNA-seq data confirmed the regulation of genes affecting cell-to-cell communication, and signal propagation in both Panx1a$^{-/-}$ and Panx1b$^{-/-}$ fishlines, and this, in turn, could explain the abnormal behavioral patterns that the fish exhibits during OMR and OKR.

6.3. Loss of Panx1a and Panx1b affects visually guided locomotor behavior and is interconnected with the habenula to process directional information

Optic flow is the animal's innate self-motion by creating a drifting movement through the visual scene that covers the entire visual field of the organism (Matsuda & Kubo, 2021). The animal can make appropriate decisions regarding adjusting body position, gaze stabilization, and posture with respect to the environment. In the zebrafish, the neural circuits of processing optic flow are measured in the form of optokinetic response (OKR) and optomotor response (OMR). The OMR is associated with how the fish adjusts its body position and direction of swimming to optic flow. (Orger et al., 2000). The OMR response was conducted to see whether Panx1a and Panx1b fish lines exhibit directional bias when exposed to leftward and rightward moving gratings. Through this behavioral assay, it was suggested that both the 6dpf Panx1a$^{-/-}$ and Panx1b$^{-/-}$ larvae display difficulties in making a decision to go to the left direction or right direction when exposed to leftward and rightward moving grating at low light conditions. Due to having a bias towards the left and right direction at low light conditions, we speculated that it might be interconnected with the habenula region to process directional information. Studies by

Zhang and colleagues (2017) have shown that lesions to the left dorsal Hb are associated with regulating light-preference behavior in the zebrafish by receiving the visual information from the specific subtypes of the RGCs via the eminentia thalami (EmT). This innate behavior is crucial for animal survival and inactivation of the left dorsal Hb causes impairment in the retinal input dependent on light luminescence. Another study by Cherng and colleagues (2020) demonstrated that silencing the habenula-interpeduncular nucleus pathway in zebrafish impairs the left-right-dependent decision-making. In addition, changes in light signals can lead to changes to the neural activity of the lateral habenula, disrupting the circadian rhythm activities (Young et al., 2021). Interestingly, the loss of Panx1a led to changes in visuomotor behavior and was associated with light decrement detection and abnormal responses to visual stimulus through the retinal OFF-pathway via dopaminergic and adenosine signaling pathways (Safarian et al., 2020). In addition, The Panx1b was suggested to be involved in modulating the circadian clock system, mediating the sleep-wake cycle of the zebrafish visual system in forming non-visual processes (Safarian et al., 2021). Hence, we performed immunohistochemistry and found that both Panx1a and Panx1b co-localize with the acetylated tubulin antibody that has been used as a habenula marker to stain the habenula region. In addition, we found that Panx1b and GFAP display co-localization in the brain and interestingly stain the habenula region. The lateral habenula was associated with an increased expression of astrocytes which implicates the neuron burst firings and changes to circadian oscillations leading to experiencing depression (Cui et al., 2018).

6.4 Summary of findings and conclusions

In conclusion, through performing OMR, it was evident that both Panx1a$^{-/-}$ and Panx1b$^{-/-}$ display a directional bias or the inability to make a leftward and rightward direction at low light contrast when exposed to left and right moving grating respectively. The speculation of this was that both Panx1a$^{-/-}$ and Panx1b$^{-/-}$ are interconnected with the habenula to process directional information since the habenula plays a role in biased left and right decision-making (Cherng et al., 2020), as well as light preference behavior (Zhang et al., 2017). Through immunohistochemistry, there was mutual co-localization with the Panx1a and Panx1b antibodies and the Habenula region (acetylated tubulin was used as the habenula marker to stain the habenula region). Moreover, by conducting OKR it was found that both Panx1a$^{-/-}$ and Panx1b$^{-/-}$ exhibit ocular motor deficiencies. The RNA-seq analysis validated a broad regulation of axon guidance, retinal axon guidance, astrocytes, axons, dendrites, and synapse genes. Through RT-qPCR the regulation of 16 genes involved in axon guidance pathfinding in the 3dpf and 6dpf Panx1a$^{-/-}$ and Panx1b$^{-/-}$ were tested and it was confirmed that there is abnormal regulation of the axon guidance pathfinding genes during the early stages of larval development, and this could modify the neuronal circuitry as the larvae develop. In addition, it was suggested that the axon guidance pathfinding connecting the retinal ganglion cell layer to the habenula region through axons has been altered affecting the direction information processing of the two fishlines. Therefore, the findings presented in this thesis support the initial hypothesis.

6.5. Limitations and Future Directions

6.5.1. Behavior and lifetime

There were limitations in this study that need to be taken into consideration in the future. At the level of 5-6 dpf larvae the muscle and neuronal system is still developing, and this could lead to variation in the saccadic peak velocity when testing out the larvae. Future work should investigate the pattern of the saccadic eye movement in adult Panx1a$^{-/-}$ and Panx1b$^{-/-}$ fishlines and see how the different genotypes affect ocular motor behavior across the lifetime. Overall, abnormalities in the frequency of the saccadic response in the zebrafish larvae does indicate an underlying issue in neuronal development, motor control, and visual processing. This provides us with valuable insight into the involvement of Panx1a and Panx1b in both normal development and potential neurological disorders.

6.5.2. Anatomical work axon tracing

Due to time limitations, tracer studies, in which lipophilic substances are injected into individual neurons could not be performed to investigate the axon projections, anterograde and retrograde tracing, of the Panx1a$^{-/-}$ and Panx1b$^{-/-}$ fishlines compared to TL. This type of experiment could visualize whether there are anatomical abnormalities in the axonal circuitry. In addition, performing this experiment is much more difficult in the 6dpf. Future work could try this method on adult fish or rodents Panx1a$^{-/-}$ and Panx1b$^{-/-}$ to visualize the axon tracings. Another limitation was that antibodies were not available for some aspects of the study such as antibodies that stain the retinal ganglion cells to visualize the connection of these cells to the arborization field and optic tectum and how the connection and morphology differ in Panx1a$^{-/-}$ and Panx1b$^{-/-}$ fishlines. Future work should also focus on a more detailed analysis of the OMR data for abnormal posture and body movement patterns as well as the frequency of the bout responses and see how it differs in the knockout fishlines.

6.5.3. Molecular aspect

This study focused on testing a few axon guidance genes of the 3dpf and 6dpf larvae. More axon guidance genes should be tested during the different developmental stages of the knockout lines and TL to see how these genes are regulated at different development stages. Moreover, in this study, RT-qPCR was performed on the DKO fishline (larvae lacking functional Panx1a and Panx1b), and many axon guidance genes were regulated (**Fig. 40**). In addition, the RNA-seq analysis of the DKO fishline demonstrates that many retinal axon guidance genes, axon guidance genes, astrocytes, dendrites, axon, and synapse genes are regulated (**Fig. 41-46**). Future work should focus on the DKO model to investigate how this fishline processes directional information. In addition, this will provide insight into how the absence of both Panx1a and Panx1b affects normal development and alters the neuronal circuitry, as well as contributing to pathological conditions.

References

Agetsuma, M., Aizawa, H., Aoki, T., Nakayama, R., Takahoko, M., Goto, M., Sassa, T., Amo, R., Shiraki, T., Kawakami, K., Hosoya, T., Higashijima, S., & Okamoto, H. (2010). The habenula is crucial for experience-dependent modification of fear responses in zebrafish. *Nature Neuroscience*, *13*(11), 1354–1356. https://doi.org/10.1038/nn.2654

Andermatt, I., Wilson, N. H., Bergmann, T., Mauti, O., Gesemann, M., Sockanathan, S., & Stoeckli, E. T. (2014). Semaphorin 6B acts as a receptor in post-crossing commissural axon guidance. *Development, 141(*19), 3709–3720. https://doi.org/10.1242/dev.112185

Bianco, I. H., Carl, M., Russell, C., Clarke, J. D., & Wilson, S. W. (2008). Brain asymmetry is encoded at the level of axon terminal morphology. *Neural Development, 3*(1), 9. https://doi.org/10.1186/1749-8104-3-9

Boassa, D., Qiu, F., Dahl, G., & Sosinsky, G. (2008). Trafficking dynamics of glycosylated pannexin1 proteins. *Cell Communication & Adhesion*, *15*(1–2), 119–132. https://doi.org/10.1080/15419060802013885

Bruzzone, R., Hormuzdi, S. G., Barbe, M. T., Herb, A., & Monyer, H. (2003). Pannexins, a family of gap junction proteins expressed in brain. *Proceedings of the National Academy of Sciences*, *100*(23), 13644. https://doi.org/10.1073/pnas.2233464100

Cenedese, V., de Graaff, W., Csikós, T., Poovayya, M., Zoidl, G., & Kamermans, M. (2017). Pannexin 1 Is Critically Involved in Feedback from Horizontal Cells to Cones. *Frontiers in Molecular Neuroscience, 10*, 403. https://doi.org/10.3389/fnmol.2017.00403

Chen, C.-C., Bockisch, C. J., Straumann, D., & Huang, M. Y.-Y. (2016). Saccadic and postsaccadic disconjugacy in zebrafish larvae suggests independent eye movement control. *Frontiers in Systems Neuroscience*, *10*. https://doi.org/10.3389/fnsys.2016.00080

Cherng, B.-W., Islam, T., Torigoe, M., Tsuboi, T., & Okamoto, H. (2020). The Dorsal Lateral Habenula-Interpeduncular Nucleus Pathway Is Essential for Left-Right-Dependent Decision Making in Zebrafish. *Cell Reports*, *32*(11), 108143. https://doi.org/10.1016/j.celrep.2020.108143

Cohen-Cory, S., Kidane, A. H., Shirkey, N. J., & Marshak, S. (2010). Brain-Derived Neurotrophic Factor and the Development of Structural Neuronal Connectivity. *Developmental Neurobiology*, *70*(5), 271–288. https://doi.org/10.1002/dneu.20774

Connell-Crowley, L., Le Gall, M., Vo, D. J., & Giniger, E. (2000). The cyclin-dependent kinase Cdk5 controls multiple aspects of axon patterning in vivo. *Current Biology: CB*, *10*(10), 599–602. https://doi.org/10.1016/s0960-9822(00)00487-5

Cui, Y., Yang, Y., Ni, Z., Dong, Y., Cai, G., Foncelle, A., Ma, S., Sang, K., Tang, S., Li, Y., Shen, Y., Berry, H., Wu, S., & Hu, H. (2018). Astroglial Kir4.1 in the lateral habenula drives neuronal bursts in depression. *Nature*, *554*(7692), 323–327. https://doi.org/10.1038/nature25752

Dahl, G., & Keane, R. W. (2012). Pannexin: From discovery to bedside in 11±4 years? *Brain Research*, *1487*, 150–159. https://doi.org/10.1016/j.brainres.2012.04.058

Deng, Z., He, Z., Maksaev, G., Bitter, R. M., Rau, M., Fitzpatrick, J. A., & Yuan, P. (2020). Cryo-EM structures of the ATP release channel Pannexin 1. *Nature Structural & Molecular Biology*, *27*(4), 373–381. https://doi.org/10.1038/s41594-020-0401-0

Gajardo, I., Salazar, C. S., Lopez-Espíndola, D., Estay, C., Flores-Muñoz, C., Elgueta, C., Gonzalez-Jamett, A. M., Martínez, A. D., Muñoz, P., & Ardiles, Á. O. (2018). Lack of Pannexin 1 Alters Synaptic GluN2 Subunit Composition and Spatial Reversal Learning in Mice. *Frontiers in Molecular Neuroscience*, *11*, 114. https://doi.org/10.3389/fnmol.2018.00114

Garbutt, S., Riley, D. E., Kumar, A. N., Han, Y., Harwood, M. R., & Leigh, R. J. (2004). Abnormalities of optokinetic nystagmus in progressive supranuclear palsy. *Journal of Neurology, Neurosurgery, and Psychiatry, 75*(10), 1386–1394. https://doi.org/10.1136/jnnp.2003.027367

Gramage, E., Li, J., & Hitchcock, P. (2014). The expression and function of midkine in the vertebrate retina. *British Journal of Pharmacology*, *171*(4), 913–923. https://doi.org/10.1111/bph.12495

Grossman, S. N., & Rucker, J. C. (2023). Opsoclonus and ocular flutter: Evaluation and management. *Current Opinion in Ophthalmology, 34*(6), 465–469. https://doi.org/10.1097/ICU.0000000000000998

Guilding, C., Hughes, A. T. L., Brown, T. M., Namvar, S., & Piggins, H. D. (2009). A riot of rhythms: Neuronal and glial circadian oscillators in the mediobasal hypothalamus. *Molecular Brain, 2*, 28. https://doi.org/10.1186/1756-6606-2-28

Hastings, M. H., Maywood, E. S., & Brancaccio, M. (2018). Generation of circadian rhythms in the suprachiasmatic nucleus. Nature Reviews. *Neuroscience, 19*(8), 453–469. https://doi.org/10.1038/s41583-018-0026-z

Hikosaka, O. (2010). The habenula: from stress evasion to value-based decision-making. *Nature Reviews. Neuroscience*, *11*(7), 503–513. https://doi.org/10.1038/nrn2866

Jensen, K., Beylergil, S. B., & Shaikh, A. G. (2019). Slow saccades in cerebellar disease. *Cerebellum & Ataxias, 6*, 1. https://doi.org/10.1186/s40673-018-0095-9

Kassavetis, P., Kaski, D., Anderson, T., & Hallett, M. (2022). Eye Movement Disorders in Movement Disorders. *Movement Disorders Clinical Practice, 9*(3), 284–295. https://doi.org/10.1002/mdc3.13413

Kölsch, Y., Hahn, J., Sappington, A., Stemmer, M., Fernandes, A. M., Helmbrecht, T. O., . . . Baier, H. (2021). Molecular classification of zebrafish retinal ganglion cells links genes to cell types to behavior. *Neuron, 109*(4), 645–662.e9. https://doi.org/10.1016/j.neuron.2020.12.003.

Kranz, K., Dorgau, B., Pottek, M., Herrling, R., Schultz, K., Bolte, P., Monyer, H., Penuela, S., Laird, D. W., Dedek, K., Weiler, R., & Janssen-Bienhold, U. (2013). Expression of Pannexin1 in the outer plexiform layer of the mouse retina and physiological impact of its knockout. *The Journal of Comparative Neurology, 521*(5), 1119–1135. https://doi.org/10.1002/cne.23223

Li, B., Piriz, J., Mirrione, M., Chung, C., Proulx, C. D., Schulz, D., Henn, F., & Malinow, R. (2011). Synaptic potentiation onto habenula neurons in the learned helplessness model of depression. *Nature, 470*(7335), 535–539. https://doi.org/10.1038/nature09742

Li, S., Bjelobaba, I., & Stojilkovic, S. S. (2018). Interactions of Pannexin1 channels with purinergic and NMDA receptor channels. Biochimica Et Biophysica Acta. *Biomembranes, 1860*(1), 166–173. https://doi.org/10.1016/j.bbamem.2017.03.025

Li, Y. N., Tsujimura, T., Kawamura, S., & Dowling, J. E. (2012). Bipolar Cell-Photoreceptor Connectivity in the Zebrafish (Danio rerio) Retina. *The Journal of Comparative Neurology, 520*(16), 3786–3802. https://doi.org/10.1002/cne.23168

Ling, Z.-M., Wang, Q., Ma, Y., Xue, P., Gu, Y., Cao, M.-H., & Wei, Z.-Y. (2021). Astrocyte Pannexin 1 Suppresses LPS-Induced Inflammatory Responses to Protect Neuronal SHSY5Y Cells. *Frontiers in Cellular Neuroscience, 15,* 710820. https://doi.org/10.3389/fncel.2021.710820

Locovei, S., Scemes, E., Qiu, F., Spray, D. C., & Dahl, G. (2007). Pannexin1 is part of the pore forming unit of the P2X(7) receptor death complex. *FEBS Letters, 581*(3), 483–488. https://doi.org/10.1016/j.febslet.2006.12.056

Manders, E. M., Verbeek, F. J., & Aten, J. A. (1993). Measurement of co-localization of objects in dual-colour confocal images. *Journal of Microscopy, 169*(3), 375–382. https://doi.org/10.1111/j.1365-2818.1993.tb03313.x

Matsuda, K., & Kubo, F. (2021). Circuit Organization Underlying Optic Flow Processing in Zebrafish. *Frontiers in Neural Circuits, 15*, 709048. https://doi.org/10.3389/fncir.2021.709048

Matsumoto, M., & Hikosaka, O. (2007). Lateral habenula as a source of negative reward signals in dopamine neurons. *Nature, 447*(7148), 1111–1115. https://doi.org/10.1038/nature05860

McDonald, M. A., Stevenson, C. H., Kersten, H. M., & Danesh-Meyer, H. V. (2022). Eye movement abnormalities in glaucoma patients: A Review. *Eye and Brain, 14* (83). https://doi.org/10.2147/eb.s361946

Michalski, K., Syrjanen, J. L., Henze, E., Kumpf, J., Furukawa, H., & Kawate, T. (2020). The Cryo-EM structure of pannexin 1 reveals unique motifs for ion selection and inhibition. *eLife, 9*, e54670. https://doi.org/10.7554/eLife.54670

Mim, C., Perkins, G., & Dahl, G. (2021). Structure versus function: Are new conformations of pannexin 1 yet to be resolved? *The Journal of General Physiology, 153*(5), e202012754. https://doi.org/10.1085/jgp.202012754

Muto, A., Orger, M. B., Wehman, A. M., Smear, M. C., Kay, J. N., Page-McCaw, P. S., Gahtan, E., Xiao, T., Nevin, L. M., Gosse, N. J., Staub, W., Finger-Baier, K., & Baier, H. (2005). Forward genetic analysis of visual behavior in zebrafish. *PLoS Genetics, 1*(5), e66. https://doi.org/10.1371/journal.pgen.0010066

Nakamura, F., Kalb, R. G., & Strittmatter, S. M. (2000). Molecular basis of semaphorin-mediated axon guidance. *Journal of Neurobiology, 44*(2), 219–229. https://doi.org/10.1002/1097-4695(200008)44:2<219::aid-neu11>3.0.co;2-w

Orger, M. (2016). The Cellular Organization of Zebrafish Visuomotor Circuits. *Current Biology, 26*(9), R377–R385. https://doi.org/10.1016/j.cub.2016.03.054.

Orger, M. B., Smear, M. C., Anstis, S. M., & Baier, H. (2000). Perception of Fourier and non-Fourier motion by larval zebrafish. *Nature Neuroscience, 3*(11), 1128–1133. https://doi.org/10.1038/80649

Orger, M. B., Kampff, A. R., Severi, K. E., Bollmann, J. H., & Engert, F. (2008). Control of visually guided behavior by distinct populations of spinal projection neurons. *Nature Neuroscience, 11*(3), 327–333. https://doi.org/10.1038/nn2048

Paeye, C., & Madelain, L. (2011). Reinforcing Saccadic Amplitude Variability. *Journal of the Experimental Analysis of Behavior, 95*(2), 149–162. https://doi.org/10.1901/jeab.2011.95-149

Park, J. S., Ryu, J. H., Choi, T. I., Bae, Y. K., Lee, S., Kang, H. J., & Kim, C. H. (2016). Innate Color Preference of Zebrafish and Its Use in Behavioral Analyses. *Molecules and Cells, 39*(10), 750–755. https://doi.org/10.14348/molcells.2016.0173.

Pelegrin, P., Barroso-Gutierrez, C., & Surprenant, A. (2008). P2X7 receptor differentially couples to distinct release pathways for IL-1beta in mouse macrophage. *Journal of Immunology (Baltimore, Md.: 1950), 180*(11), 7147–7157. https://doi.org/10.4049/jimmunol.180.11.7147

Poller, W. C., Madai, V. I., Bernard, R., Laube, G., & Veh, R. W. (2013). A glutamatergic projection from the lateral hypothalamus targets VTA-projecting neurons in the lateral habenula of the rat. *Brain Research, 1507*, 45–60. https://doi.org/10.1016/j.brainres.2013.01.029

Prochnow, N., Abdulazim, A., Kurtenbach, S., Wildförster, V., Dvoriantchikova, G., Hanske, J., Petrasch-Parwez, E., Shestopalov, V. I., Dermietzel, R., Manahan-Vaughan, D., & Zoidl, G. (2012). Pannexin1 Stabilizes Synaptic Plasticity and Is Needed for Learning. *PLoS ONE*, *7*(12), e51767. https://doi.org/10.1371/journal.pone.0051767

Ray, A., Zoidl, G., Weickert, S., Wahle, P., & Dermietzel, R. (2005). Site-specific and developmental expression of pannexin1 in the mouse nervous system. *The European Journal of Neuroscience*, *21*(12), 3277–3290. https://doi.org/10.1111/j.1460-9568.2005.04139.x

Safarian, N., Houshangi-Tabrizi, S., Zoidl, C., & Zoidl, G. R. (2021). Panx1b Modulates the Luminance Response and Direction of Locomotion in the Zebrafish. *International Journal of Molecular Sciences*, *22*(21), 11750. https://doi.org/10.3390/ijms222111750

Safarian, N., Whyte-Fagundes, P., Zoidl, C., Grigull, J., & Zoidl, G. (2020). Visuomotor deficiency in panx1a knockout zebrafish is linked to dopaminergic signaling. *Scientific Reports*, *10*(1), 9538. https://doi.org/10.1038/s41598-020-66378-y

Shao, Q., Lindstrom, K., Shi, R., Kelly, J., Schroeder, A., Juusola, J., Levine, K. L., Esseltine, J. L., Penuela, S., Jackson, M. F., & Laird, D. W. (2016). A Germline Variant in the PANX1 Gene Has Reduced Channel Function and Is Associated with Multisystem Dysfunction. *Journal of Biological Chemistry*, *291*(24), 12432–12443. https://doi.org/10.1074/jbc.M116.717934

Shestopalov, V. I., Dvoriantchikova, G., Kurtenbach, S., Reiser, A., Kokzhekbaeva, Z., & Tuzhikov, A. (2016). Ganglion cell loss in ocular and glaucoma is facilitated by the Panx1-regulated inflammasome. *Investigative Ophthalmology & Visual Science*, *57*(12), 2247. https://iovs.arvojournals.org/article.aspx?articleid=2560732

Silverman, de Rivero Vaccari, J. P., Locovei, S., Qiu, F., Carlsson, S. K., Scemes, E., Keane, R. W., & Dahl, G. (2009). The pannexin 1 channel activates the inflammasome in neurons and astrocytes. *The Journal of Biological Chemistry*, *284*(27), 18143–18151. https://doi.org/10.1074/jbc.M109.004804

Sosinsky, G. E., Boassa, D., Dermietzel, R., Duffy, H. S., Laird, D. W., MacVicar, B., Naus, C. C., Penuela, S., Scemes, E., Spray, D. C., Thompson, R. J., Zhao, H.-B., & Dahl, G. (2011). Pannexin channels are not gap junction hemichannels. *Channels (Austin, Tex.), 5*(3), 193–197. https://doi.org/10.4161/chan.5.3.15765

Szmulewicz, D. J., Waterston, J. A., MacDougall, H. G., Mossman, S., Chancellor, A. M., McLean, C. A., Merchant, S., Patrikios, P., Halmagyi, G. M., & Storey, E. (2011). Cerebellar ataxia, neuropathy, vestibular areflexia syndrome (CANVAS): A review of the clinical features and video-oculographic diagnosis. *Annals of the New York Academy of Sciences, 1233*, 139–147. https://doi.org/10.1111/j.1749-6632.2011.06158.x

Tessier-Lavigne, M., & Goodman, C. S. (1996). The molecular biology of axon guidance. *Science (New York, N.Y.), 274*(5290), 1123–1133. https://doi.org/10.1126/science.274.5290.1123

Whyte-Fagundes, P., & Zoidl, G. (2018). Mechanisms of pannexin1 channel gating and regulation. *Biochimica et Biophysica Acta - Biomembranes, 1860*(1), 65–71. https://doi.org/10.1016/j.bbamem.2017.07.009

Thiele, T. R., Donovan, J. C., & Baier, H. (2014). Descending control of swim posture by a midbrain nucleus in zebrafish. *Neuron, 83*(3), 679–691. https://doi.org/10.1016/j.neuron.2014.04.018

Yamaguchi, T., Danjo, T., Pastan, I., Hikida, T., & Nakanishi, S. (2013). Distinct roles of segregated transmission of the septo-habenular pathway in anxiety and fear. *Neuron*, *78*(3), 537–544. https://doi.org/10.1016/j.neuron.2013.02.035

Young, C. J., Lyons, D., & Piggins, H. D. (2021). Circadian Influences on the Habenula and Their Potential Contribution to Neuropsychiatric Disorders. *Frontiers in Behavioral Neuroscience, 15,* 815700. https://doi.org/10.3389/fnbeh.2021.815700

Young, C. J., Lyons, D., & Piggins, H. D. (2022). Circadian Influences on the Habenula and Their Potential Contribution to Neuropsychiatric Disorders. *Frontiers in Behavioral Neuroscience, 15*, 815700. https://doi.org/10.3389/fnbeh.2021.815700

Zhao, H., & Rusak, B. (2005). Circadian firing-rate rhythms and light responses of rat habenular nucleus neurons in vivo and in vitro. *Neuroscience, 132*(2), 519–528. https://doi.org/10.1016/j.neuroscience.2005.01.012

Zhao, H.-B., Zhu, Y., Liang, C., & Chen, J. (2015). Pannexin 1 deficiency can induce hearing loss. *Biochemical and Biophysical Research Communications, 463*(1–2), 143–147. https://doi.org/10.1016/j.bbrc.2015.05.049

Zhang, S., Yuan, B., Lam, J. H., Zhou, J., Zhou, X., Ramos-Mandujano, G., Tian, X., Liu, Y., Han, R., Li, Y., Gao, X., Li, M., & Yang, M. (2021). Structure of the full-length human Pannexin1 channel and insights into its role in pyroptosis. *Cell Discovery, 7*(1), 1–15. https://doi.org/10.1038/s41421-021-00259-0

Zoidl, G., Kremer, M., Zoidl, C., Bunse, S., & Dermietzel, R. (2008). Molecular diversity of connexin and pannexin genes in the retina of the zebrafish *Danio rerio*. *Cell Communication & Adhesion, 15*(1–2), 169–183. https://doi.org/10.1080/15419060802014081.

8. Supplementary Materials

The RT-qPCR and RNA-seq analysis of the DKO fishline was also tested as an exploration and future direction (**Fig 40-46**).

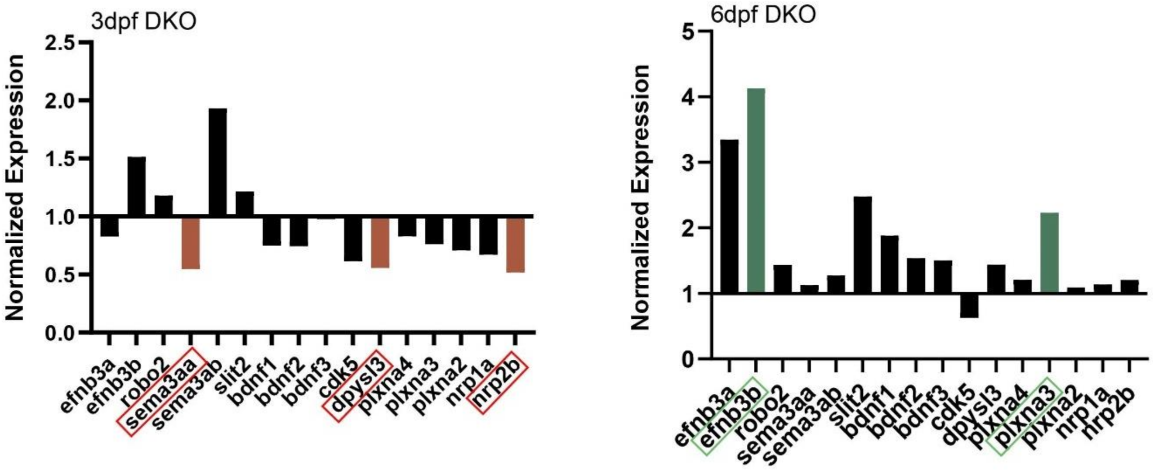

Figure 40. The differential expression of axon guidance pathfinding genes in 3dpf and 6dpf DKO was determined through RT-qPCR and compared with 3dpf and 6dpf TL. Sixteen genes were selected from the axon guidance pathfinding pathway. The regulation of genes in the 3dpf DKO and 6dpf DKO. The gene expression was normalized to 1. The red bars represent downregulation and the green bars represent upregulation of the selected genes.

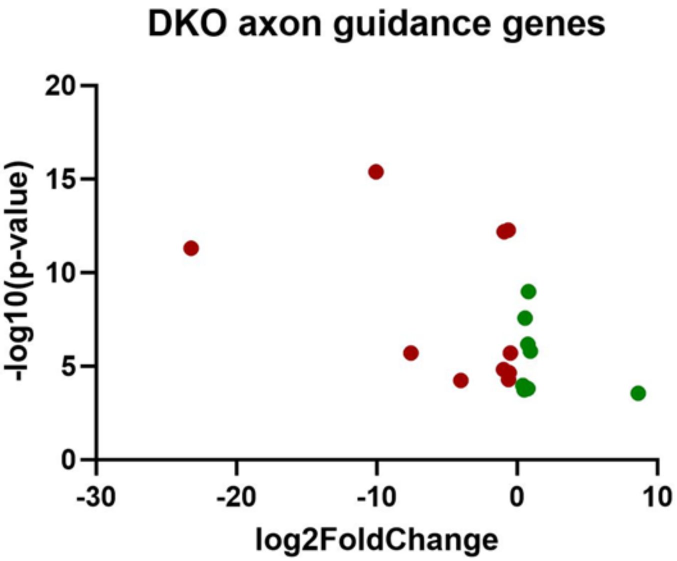

AXON GUIDANCE GENES

	TL VS DKO		
GENE NAME	***log2FoldChange***	***p-value***	***padj***
ACLYA	-0.47987	1.97E-06	0.000139
ALCAMB	-0.60482	5.15E-05	0.002108
ARNT2	0.772704	6.64E-07	5.61E-05
ATXN7	0.763863	0.000155	0.004971
CDH11	-0.92085	6.4E-13	2.46E-10
EFNA1A	0.570692	2.62E-08	3.36E-06
EXTL3	0.491759	0.00018	0.005546
GNL3	-0.57248	2.2E-05	0.001055
KCNC3A	-7.56472	1.92E-06	0.000137
LAMA3	0.415891	0.000107	0.003731
NEO1B	-0.95838	1.52E-05	0.000782
NFASCA	8.641378	0.000278	0.007726
PES	-0.63358	5.34E-13	2.07E-10
PTPRFA	-23.2331	4.87E-12	1.56E-09
RAB33BA	0.806367	1.02E-09	1.83E-07
SEMA4AB	-10.0578	4.01E-16	2.91E-13
SEMA4AB	0.941083	1.53E-06	0.000113
SI:DKEY-49N23.1	-4.01521	5.72E-05	0.002295

Figure 41. The differential expression of axon guidance genes in 6dpf DKO. The analysis of the RNA-seq data was performed at SickKids (Toronto, ON). The genes were extracted, sorted, and analyzed using Excel with the adjusted p-value (p-value<0.01). GraphPad Prism was used for the scatter plots using the log2FoldChange with -log10(p-value).

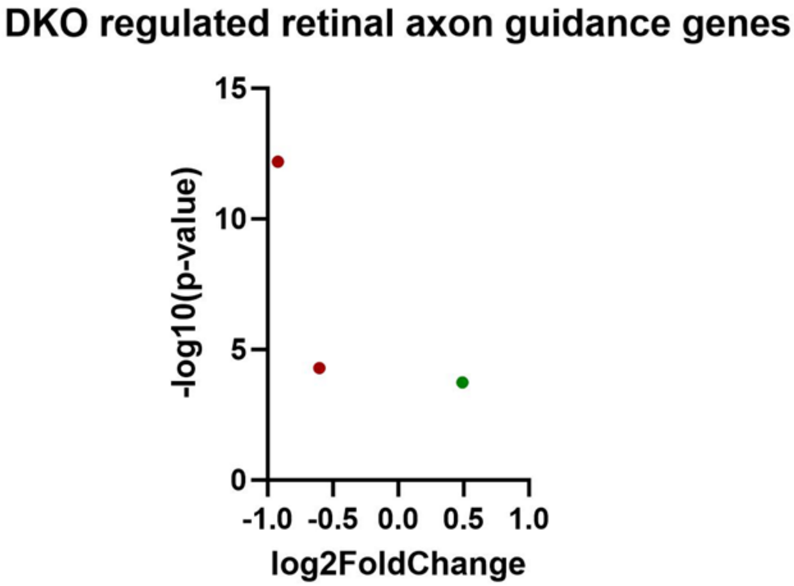

RETINAL AXON GUIDANCE

	TL VS DKO		
GENE NAME	***log2FoldChange***	***pvalue***	***padj***
ALCAMB	-0.604824158	5.15088E-05	0.002108012
CDH11	-0.920845571	6.4043E-13	2.46036E-10
EXTL3	0.491758962	0.000179612	0.005545755

Figure 42. The differential expression of retinal axon guidance genes in 6dpf DKO. The analysis of the RNA-seq data was performed at SickKids (Toronto, ON). The genes were extracted, sorted, and analyzed using Excel with the adjusted p-value (p-value<0.01). GraphPad Prism was used for the scatter plots using the log2FoldChange with -log10(p-value).

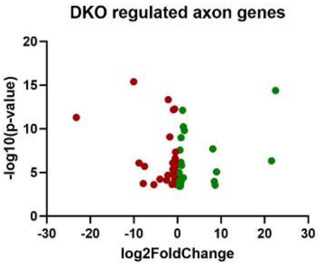

AXON GENES

TL VS DKO			
GENE NAME	***log2FoldChange***	***pvalue***	***padj***
ACLYA	-0.47987	1.97098E-06	0.000139378
ALCAMB	-0.60482	5.15088E-05	0.002108012
APLP2	0.276841	2.18175E-05	0.001051501
ARHGAP35A	1.337783	5.62749E-11	1.36267E-08
ARNT2	0.772704	6.63639E-07	5.60572E-05
ATXN7	0.763863	0.000154788	0.004971396
CDH11	-0.92085	6.4043E-13	2.46036E-10
COL12A1A	-2.17896	2.04439E-05	0.000996116
DNAH11	-1.24019	0.000229091	0.006656801
DOCK7	1.347608	3.91292E-05	0.001695628
EFNA1A	0.570692	2.62001E-08	3.35512E-06
EXTL3	0.491759	0.000179612	0.005545755
FGFR1A	0.612286	0.000280502	0.007766579
GNL3	-0.57248	2.19508E-05	0.001055384
HARS	-0.43625	5.40486E-07	4.74606E-05
HDAC6	8.439078	0.000105381	0.003683617
HSD17B4	0.451285	0.000133477	0.004400119
HYDIN	0.646162	0.00026568	0.007475349
IGF2BP1	-0.23647	0.000239227	0.006912449
INSRA	0.376134	1.01405E-05	0.000563494
KCNC1A	8.971451	8.32055E-06	0.000475593
KCNC3A	-7.56472	1.92396E-06	0.000136779
KIF1AA	1.577954	1.57889E-10	3.42841E-08
LAMA3	0.415891	0.000107121	0.003731393
LGMN	-1.04863	4.29392E-06	0.000268481
LINGO1A	21.57546	4.54296E-07	4.06972E-05
MAPK14A	-5.42154	0.000249629	0.007103675
MYO5B	-0.60241	2.84387E-06	0.000191609
NEO1B	-0.95838	1.52144E-05	0.000782339
NFASCA	8.641378	0.000278052	0.007725508
PAFAH1B1A	-0.46514	4.60932E-08	5.5138E-06
PES	-0.63358	5.34284E-13	2.0725E-10

Figure 43. The differential expression of axon genes in 6dpf DKO. The analysis of the RNA-seq data was performed at SickKids (Toronto, ON). The genes were extracted, sorted, and analyzed using Excel with the adjusted p-value (p-value<0.01). GraphPad Prism was used for the scatter plots using the log2FoldChange with -log10(p-value).

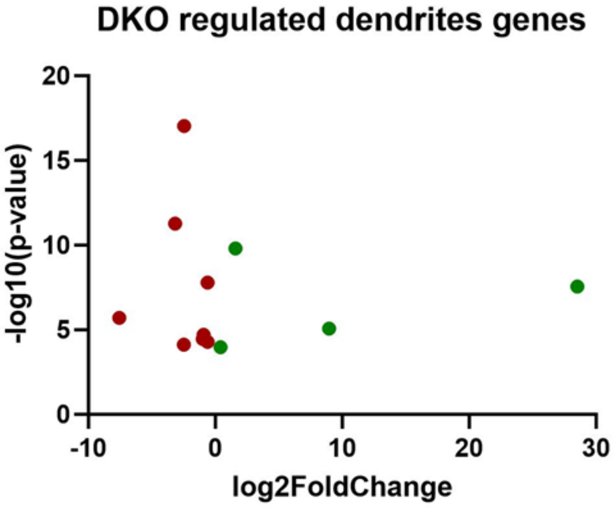

DENDRITES

TL VS DKO			
GENE NAME	***log2FoldChange***	***pvalue***	***padj***
ALCAMB	-0.604824158	5.15088E-05	0.002108012
KCNC1A	8.971450607	8.32055E-06	0.000475593
KCNC3A	-7.564720514	1.92396E-06	0.000136779
KIF1AA	1.577954403	1.57889E-10	3.42841E-08
KIF3B	28.53271952	2.76697E-08	3.52075E-06
LAMA3	0.415890514	0.000107121	0.003731393
MARK2A	-3.177021391	5.31786E-12	1.65992E-09
NEDD4L	-0.621994233	1.59102E-08	2.14033E-06
PANX1A	-2.462077586	9.20952E-18	7.99907E-15
RHOAB	-0.912797327	1.96281E-05	0.000971667
SI:DKEY-11O1.6	-2.466784182	7.46102E-05	0.002812242
STAU1	-0.982821227	3.41745E-05	0.0015205

Figure 44. The differential expression of dendrite genes in 6dpf DKO. The analysis of the RNA-seq data was performed at SickKids (Toronto, ON). The genes were extracted, sorted, and analyzed using Excel with the adjusted p-value (p-value<0.01). GraphPad Prism was used for the scatter plots using the log2FoldChange with -log10(p-value).

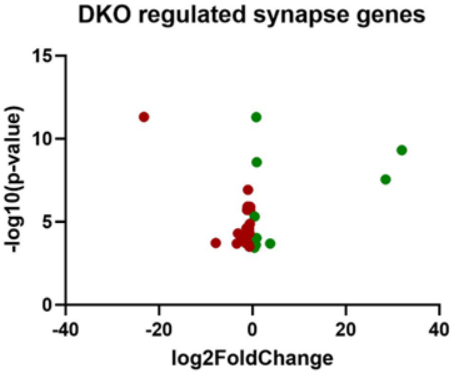

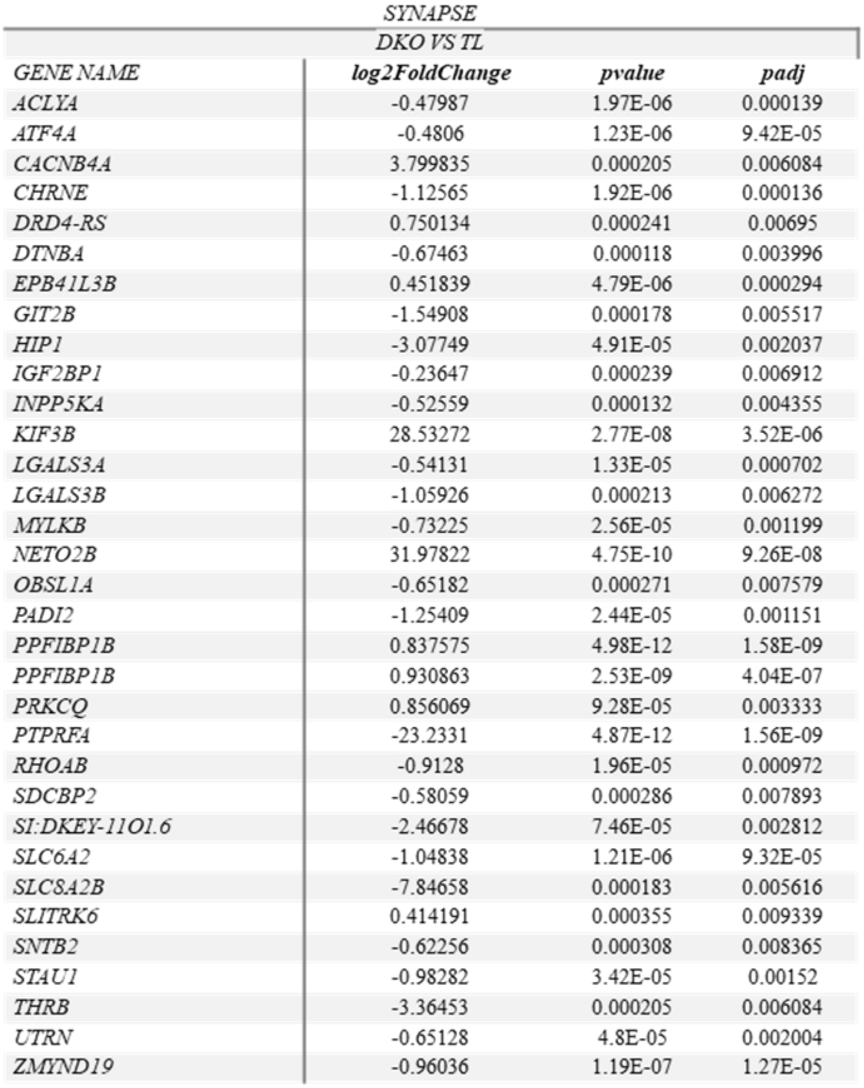

SYNAPSE			
	DKO VS TL		
GENE NAME	log2FoldChange	pvalue	padj
ACLYA	-0.47987	1.97E-06	0.000139
ATF4A	-0.4806	1.23E-06	9.42E-05
CACNB4A	3.799835	0.000205	0.006084
CHRNE	-1.12565	1.92E-06	0.000136
DRD4-RS	0.750134	0.000241	0.00695
DTNBA	-0.67463	0.000118	0.003996
EPB41L3B	0.451839	4.79E-06	0.000294
GIT2B	-1.54908	0.000178	0.005517
HIP1	-3.07749	4.91E-05	0.002037
IGF2BP1	-0.23647	0.000239	0.006912
INPP5KA	-0.52559	0.000132	0.004355
KIF3B	28.53272	2.77E-08	3.52E-06
LGALS3A	-0.54131	1.33E-05	0.000702
LGALS3B	-1.05926	0.000213	0.006272
MYLKB	-0.73225	2.56E-05	0.001199
NETO2B	31.97822	4.75E-10	9.26E-08
OBSL1A	-0.65182	0.000271	0.007579
PADI2	-1.25409	2.44E-05	0.001151
PPFIBP1B	0.837575	4.98E-12	1.58E-09
PPFIBP1B	0.930863	2.53E-09	4.04E-07
PRKCQ	0.856069	9.28E-05	0.003333
PTPRFA	-23.2331	4.87E-12	1.56E-09
RHOAB	-0.9128	1.96E-05	0.000972
SDCBP2	-0.58059	0.000286	0.007893
SI:DKEY-11O1.6	-2.46678	7.46E-05	0.002812
SLC6A2	-1.04838	1.21E-06	9.32E-05
SLC8A2B	-7.84658	0.000183	0.005616
SLITRK6	0.414191	0.000355	0.009339
SNTB2	-0.62256	0.000308	0.008365
STAU1	-0.98282	3.42E-05	0.00152
THRB	-3.36453	0.000205	0.006084
UTRN	-0.65128	4.8E-05	0.002004
ZMYND19	-0.96036	1.19E-07	1.27E-05

Figure 45. The differential expression of synapse genes in 6dpf DKO. The analysis of the RNA-seq data was performed at SickKids (Toronto, ON). The genes were extracted, sorted, and analyzed using Excel with the adjusted p-value (p-value<0.01). GraphPad Prism was used for the scatter plots using the log2FoldChange with -log10(p-value).

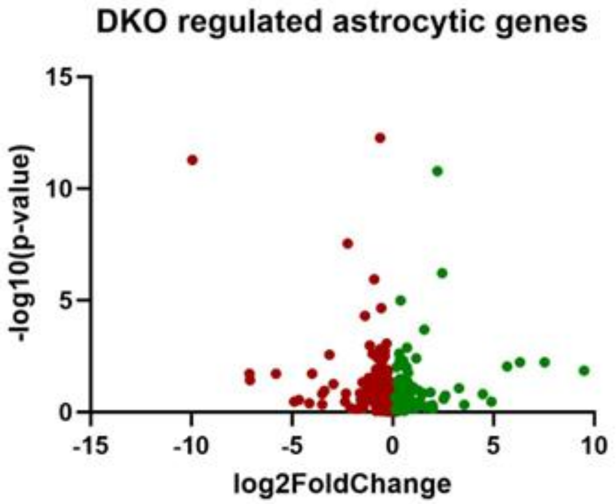

ASTROCYTES

	DKO VS TL		
GENE NAME	***log2FoldChange***	***pvalue***	***padj***
APCDD1L	-1.59256	0.279374	0.635746
APOBEC2A	-0.06508	0.792843	0.946937
APOBEC2B	-0.48672	0.442688	0.771507
APOEA	0.108629	0.654222	0.891196
ASCL1A	-0.12079	0.672351	0.899385
ATP1A2A	-0.91726	1.14E-06	8.86E-05
BANP	0.069066	0.615319	0.871061
C3A.1	-0.26365	0.510827	0.815699
C7B	-0.71288	0.557298	0.843338
CA2	-0.27666	0.2152	0.567121
CADM1A	0.026077	0.89324	0.980345
CADM1B	0.67016	0.312126	0.669292
CADM2B	-2.95776	0.055333	0.282968
CADM4	0.358852	0.032281	0.209717
CAHZ	0.421866	0.744996	0.929316
CDH2	0.041787	0.66062	0.894271
CDHR1A	0.386295	0.217554	0.569844
CDK1	-0.89959	0.047842	0.261455
CEP290	-0.23554	0.473031	0.791216
CHAF1B	-1.20143	0.029539	0.198121
CLCF1	-0.46691	0.09507	0.380633
CLN3	0.252796	0.12789	0.443392
CLRN1	-0.88086	0.069185	0.319748
CRB2A	-0.06075	0.751273	0.931896

CRLF1A	-0.06042	0.793629	0.946971
CSNK1A1	0.713865	0.046551	0.257497
CUX2B	4.90111	0.34106	0.694286
DCAF8	0.18319	0.211593	0.562826
DCTN1A	0.046791	0.59025	0.858593
DCTN2	0.104509	0.486326	0.800021
DKK1A	-0.04797	0.860147	0.9703
DKK1B	-0.44835	0.293895	0.651408
DKK1B	0.305647	0.637691	0.882985
DKK2	-0.00469	0.988737	1
DKK3A	-0.2922	0.188737	0.533172
DKK3B	-0.2647	0.339749	0.69317
DNAJC2	-0.12577	0.315614	0.672511
EGR1	0.123443	0.788042	0.945509
ELOVL2	-0.02707	0.908218	0.984159
EPB41L5	-0.6293	0.034876	0.219928
ESCO2	-0.90484	0.074697	0.333531
F8	-0.75491	0.003862	0.052736
FABP7A	0.107706	0.566764	0.848203
FAT1B	9.486483	0.013819	0.124434
FMNL2A	-0.30816	0.000845	0.018101
FOXN4	1.312353	0.472508	0.790941
FUT8A	0.114295	0.289656	0.646786
FZD2	-0.41903	0.060009	0.296182
FZD3A	0.000736	0.99702	1
FZD8A	-0.06634	0.600073	0.86354
FZD8B	0.370555	0.093534	0.376999
FZD9A	0.357601	0.48125	0.797075
GAPDH	-0.70403	0.013465	0.122325
GDF10A	-0.36936	0.197075	0.543835
GDF10B	0.045549	0.907169	0.983957
GDF6A	-0.34397	0.133723	0.452996
GFAP	0.02248	0.913492	0.985371
GJD2B	0.101006	0.697519	0.90957
GLI2B	0.241699	0.097413	0.385425
GLI3	0.009997	0.927208	0.989039
GLULA	0.289867	0.280733	0.637478
GLULB	-1.30732	0.059677	0.295475
GNL2	-0.28307	0.016595	0.139027
GNL3	-0.57248	2.2E-05	0.001055
GPR183A	-0.97179	0.040413	0.238181
GRIK2	0.427156	0.099893	0.390942
HBEGFA	-0.39492	0.226296	0.579611
HEPACAMA	0.194027	0.370239	0.717979
HER2	0.74412	0.046785	0.258113
HER4.1	-0.04502	0.884428	0.977927

HER6	-1.5887	0.145972	0.473659
HER9	0.656059	0.393027	0.735504
HSPD1	-0.67304	0.066201	0.312533
ICN2	-0.48307	0.113262	0.417969
ID2A	0.374622	0.265232	0.621859
IGF1	0.069466	0.801896	0.950297
IGF1RA	1.870472	0.13213	0.450053
IGF1RB	0.040193	0.678295	0.90179
IGFBP3	-0.11727	0.844345	0.964683
IL11A	-1.62868	0.141773	0.466936
IL6ST	0.938995	0.501665	0.808606
INS	-0.12336	0.712998	0.915514
INSM1A	0.306988	0.214827	0.56671
INSRA	0.376134	1.01E-05	0.000563
INSRB	0.144084	0.045008	0.252826
IRX1A	0.128431	0.458587	0.781571
IRX7	0.033901	0.907036	0.983866
ITGA5	-0.56055	0.009947	0.10074
ITGA6A	-0.61054	0.051307	0.271767
ITGA6B	-0.42053	0.072531	0.327928
ITGA6B	-0.22498	0.25149	0.607714
ITGB1A	-0.28977	0.306194	0.663732
ITGB1A	-0.25511	0.190996	0.535704
JUN	-0.38241	0.037146	0.227036
KCNJ10A	-0.19859	0.595131	0.860876
KCNJ13	1.467287	0.157249	0.490492
KIF11	-0.82921	0.019632	0.153831
KIRREL1A	-0.15351	0.468785	0.788266
KMT2A	0.31082	0.002422	0.038134
LAMB1A	-0.33941	0.121196	0.430686
LAMB2	-0.38913	0.088001	0.364715
LAMB4	0.197848	0.689912	0.905771
LEPB	-4.0114	0.019309	0.152284
LEPR	-1.23578	0.191574	0.53637
LGALS2A	0.652964	0.48373	0.798502
MAK16	1.162203	0.003936	0.053399
MANF	-0.7737	0.068801	0.319229
MAP1AB	-5.6E-05	0.999979	1
MAP1AB	0.309208	0.592049	0.859385
MAX	-0.15673	0.884727	0.978064
MDKA	-7.11628	0.018845	0.150229
MDKB	0.120937	0.492482	0.804113
MECP2	5.670375	0.00897	0.094229
MIB1	-0.84479	0.134803	0.455314
MMP14A	-0.44457	0.047513	0.260637
MMP2	-0.37517	0.210645	0.56173

MMP28	0.754399	0.017518	0.143628
MMP9	-3.14422	0.002722	0.041555
MYCA	-0.23105	0.211543	0.562826
MYO6B	7.528139	0.00579	0.069685
NAV1B	0.110506	0.641174	0.8848
NEUROG1	-0.16229	0.67644	0.900952
NOTCH1A	-0.31712	0.032849	0.211636
NOTCH1B	0.094875	0.55958	0.844571
NOTCH3	-0.28755	0.188189	0.532727
NPHP1	-0.57691	0.454457	0.778766
OCRL	-0.25476	0.363291	0.71232
OPN9	0.072812	0.90314	0.98243
OPN9	0.379468	0.508899	0.814311
PANX1B	-0.8327	0.013492	0.122482
PAX2A	-7.09416	0.036566	0.225211
PAX6A	-0.65411	0.78595	0.944977
PAX6B	-1.73451	0.726526	0.921512
PCNA	-1.14998	0.001033	0.020797
PDE6C	-0.11996	0.689358	0.905696
PDX1	-0.27652	0.228737	0.5823
PES	-0.63358	5.34E-13	2.07E-10
POU5F3	0.024479	0.988637	1
POU6F2	0.156876	0.654612	0.891334
PPP1R12A	0.047433	0.536866	0.832038
PRDM13	0.342183	0.384115	0.728068
PRMT6	-1.0094	0.002444	0.038375
PTF1A	0.109946	0.805756	0.951682
PTGES	-0.18217	0.518946	0.820826
RANBP9	0.188625	0.056035	0.284877
RBPJA	-0.0435	0.665331	0.896439
RHO	-0.06049	0.825157	0.958325
RLBP1A	0.044736	0.904575	0.983021
RLBP1B	-0.62598	0.001499	0.027364
RNASET2	0.700551	0.001304	0.024725
RNF41	0.337825	0.004916	0.062204
RPE65C	-5.79581	0.018986	0.150927
RX1	0.658138	0.068309	0.317901
S100A10A	0.477373	0.130784	0.448056
SART1	-0.26493	0.012778	0.118724
SCN1LAB	0.159299	0.727517	0.921861
SEC13	-0.36937	0.049516	0.266157
SERPINE3	-0.63726	0.136014	0.457527
SFPQ	0.617776	0.044961	0.252826
SHHA	-0.14534	0.200897	0.549591
SHHB	-0.25237	0.223906	0.576986
SIX3B	0.319027	0.331943	0.686327

SLC1A2B	-2.375	0.33736	0.690755
SLC1A3B	0.347682	0.779411	0.942641
SLCO1C1	0.054087	0.912195	0.985371
SLITRK2	0.293922	0.283558	0.640652
SMO	-0.22876	0.077851	0.341077
SNX19A	0.065697	0.872057	0.973622
SNX5	-0.3564	0.051389	0.271805
SOX10	-0.03226	0.844031	0.964668
SOX2	-0.18918	0.177474	0.519167
SOX9A	0.052804	0.710217	0.914067
SPTBN5	1.764426	0.557149	0.843259
STAT3	-1.00284	0.053561	0.278135
STIL	4.459336	0.157835	0.491517
SYPB	-0.60919	0.215884	0.567911
TGFB1A	-0.39969	0.0132	0.121021
TGFB1B	-0.51496	0.200161	0.548733
TGFB2	-0.25242	0.249216	0.605556
TGFB3	0.069885	0.542473	0.835124
TGIF1	0.140235	0.34307	0.695573
TIMP2B	-9.95234	5.17E-12	1.63E-09
TOPORSB	0.089538	0.495074	0.805334
TUBA1B	-0.92436	0.040217	0.237521
UBE2IB	-0.22713	0.113683	0.418621
USH1C	1.472378	0.141174	0.466318
UTP11	-0.58081	0.005381	0.065925
VIM	0.409272	0.004747	0.060799
VPS11	0.001118	0.991125	1
VPS16	0.112201	0.215403	0.56734
VSX2	0.509069	0.12743	0.44261
VWC2	0.677563	0.011373	0.110112
WNT2	0.155251	0.591722	0.859322
WNT2BA	-0.90578	0.073378	0.329865
WNT3	0.596476	0.032638	0.211015
WNT4	-0.00281	0.991361	1
WNT5B	-4.15046	0.399147	0.739663
WNT8B	0.281998	0.424152	0.759006
WT1B	-0.05346	0.895832	0.980819
XIRP1	6.315872	0.005951	0.070998
YAP1	-0.27184	0.017237	0.142156
ZIC2B	0.295346	0.229828	0.583124

Figure 46. The differential expression of astrocyte genes in 6dpf DKO. The analysis of the RNA-seq data was performed at SickKids (Toronto, ON). The genes were extracted, sorted, and analyzed using Excel with the adjusted p-value (p-value<0.01). GraphPad Prism was used for the scatter plots using the log2FoldChange with -log10(p-value).

We established the whole-mount immunohistochemistry protocol to visualize the protein expression of different antibodies using the intact larval structure. **Figure 47** illustrates the expression of astrocytes in the spinal cord and the monoclonal mouse GFAP antibody was used as a marker using whole-mount immunohistochemistry that was established throughout the duration of this thesis project.

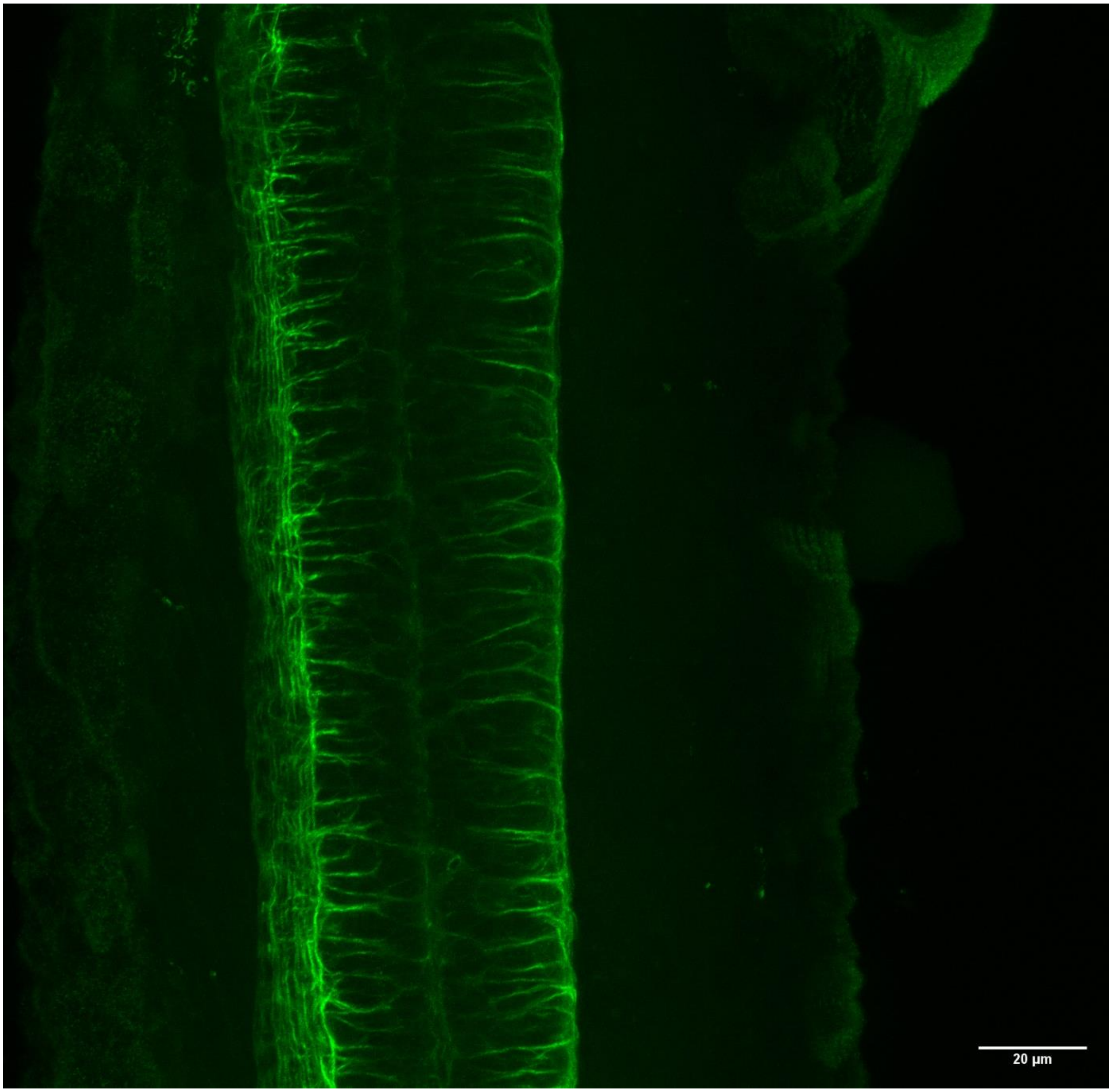

Figure 47. Expression and localization of monoclonal mouse GFAP antibody in the spinal cord using whole-mount immunohistochemistry. The figure illustrates the expression of astrocytes in the spinal cord and the monoclonal mouse GFAP antibody was used as a marker (Scale bar= 20µm).